Open access • Journal Article • DOI:10.1063/5.0029963

# Experimental investigation of internal two-phase flow structures and dynamics of quasi-stable sheet cavitation by fast synchrotron x-ray imaging — Source link

Ilyass Khlifa, Kamel Fezzaa, Olivier Coutier-Delgosha, Olivier Coutier-Delgosha

**Institutions:** Arts et Métiers ParisTech, Argonne National Laboratory, Virginia Tech

**Published on:** 13 Nov 2020 - Physics of Fluids (AIP Publishing LLCAIP Publishing)

**Topics:** Two-phase flow, Velocity gradient, Cavitation, Turbulence and Shear stress

# Experimental investigation of internal two-phase flow structures and dynamics of quasi-stable sheet cavitation by fast synchrotron x-ray imaging

Guangjian Zhang, Ilyass Khlifa, Kamel Fezzaa, Mingming Ge, Olivier Coutier-Delgosha

Physics of Fluids

# Experimental investigation of internal two-phase flow structures and dynamics of quasi-stable sheet cavitation by fast synchrotron X-ray imaging

Guangjian Zhang(张光建)[1, 2], Ilyass Khlifa[1], Kamel Fezzaa[4], Mingming Ge(葛明明)[3], Olivier Coutier-Delgosha[3, 1*]

[1]Univ. Lille, CNRS, ONERA, Arts et Métiers ParisTech, Centrale Lille, FRE 2017 - LMFL - Laboratoire de Mécanique des fluides de Lille - Kampé de Feriet, F-59000 Lille, France

[2]Research Center of Fluid Machinery Engineering and Technology, Jiangsu University, Zhenjiang 212013, China

[3]Kevin T. Crofton Department of Aerospace and Ocean Engineering, Virginia Tech, Blacksburg, VA 24060, USA

[4]Advanced Photon Source, Argonne National Laboratory, 9700 S. Cass Avenue, Lemont, IL 60439, USA

*Email address for correspondence: ocoutier@vt.edu

## Abstract

The quasi-stable sheet cavitation produced in a small Venturi channel is investigated using a fast synchrotron X-ray imaging technique aided with conventional high speed photography. The use of X-rays instead of visible light solves cavitation opacity related issues, and X-ray phase contrast-based edge enhancement enables high-definition visualization of the internal two-phase morphology. The simultaneous acquisition of time-resolved velocity and void fraction fields through post-processing the recorded X-ray images reveals, for the first time, the complex diphasic flow structures inside the sheet cavity, which is essentially divided into 6 characteristic parts. Distinct from the current mainstream view, the globally-steady sheet cavitation is found to be characterized by a weak but constantly-existing re-entrant flow that can penetrate the entire cavity. The turbulent velocity fluctuations inside the sheet cavity are also investigated. The turbulence level in the reverse flow region is observed to be as low as in the outer main flow demonstrating the relatively steady status of the re-entrant flow. Unlike the streamwise and cross-stream fluctuations, the shear stress appears to be weakly correlated with the velocity gradient. The collapse of vapor phase and the vaporization at the upstream cavity interface are found to be the primary causes of shear stress intensification.

## 1. Introduction

Hydrodynamic cavitation is a complex flow phenomenon involving mass and heat transfer between liquid and vapor phase at nearly constant temperature. It typically occurs in some widely-used hydraulic machines, such as pumps and propellers, when the local pressure is reduced below the vapor pressure. The instability of a partial cavity appears as the shedding of vapor structures and the resultant cavity length oscillations. These unsteady behaviors are often responsible for undesired effects like performance degradation, material erosion, noise and vibration. Therefore, understanding the internal structures of partial cavities and the dynamics of cavitation unsteadiness is fundamental to control these detrimental effects.

Partial cavitation has two main forms of appearance: sheet and cloud cavitation (Pelz et al. 2017). The former generally appears as a quasi-stable sheet cavity with only small vapor shedding at its closure region, i.e. with an open closure. While in the latter case, the cavity is highly unstable as a consequence of periodic shedding of large vapor structures. The transition from sheet to cloud cavitation is, in a classic view, related to the motion of a re-entrant jet that breaks off the sheet cavity from the leading edge and consequently causes a large cavitation cloud to shed (Knapp, 1955). The existence of the re-entrant jet in periodic cloud cavitation was confirmed through the method of dye injection (Le et al. 1993). Kawanami et al. (1997) placed a small obstacle on the suction side of a hydrofoil to prevent the re-entrant jet from moving upstream, and the large cloud shedding disappeared, demonstrating the dominant role of the re-entrant jet. The conditions necessary for the development of the re-entrant jet has been explored by Callenaere et al. (2001). They showed the critical role of adverse pressure gradient at the cavity closure in the onset of the re-entrant jet instability.

Regarding the relatively stable sheet cavitation, Gopalan & Katz (2000), Callenaere et al. (2001) and Laberteaux & Ceccio (2001) described that no clear re-entrant jet was observed or only the weak reverse flow existed at the trailing edge of the cavity, since the adverse pressure gradient was not strong enough to drive the re-entrant jet. The similar conclusion was drawn by Leroux et al. (2004) based on the wall pressure measurements under a stable sheet cavity. However, Stutz & Reboud (1997) used a double optical probe device to measure local velocities inside a globally-steady sheet cavity, and they found the presence of a re-entrant flow even under the upstream part of the cavity. Later, Barre et al. (2009) repeated such an experiment but introducing an improved algorithm to perform velocity statistic computations. They also measured a clear re-entrant flow. Conversely, in their simultaneous numerical simulation, the reverse flow was not predicted, and eventually they did not further clarify the role the re-entrant flow plays in stable sheet cavitation. These studies show that there are still questions about stable sheet cavitation to be answered: is there a re-entrant flow underneath the cavity; if so, why does it not pinch off the cavity like in the case of unsteady cloud cavitation?

Besides quantitative velocity information, the visualization of two-phase flow morphology inside the opaque cavity is also a crucial point to improve the physical and numerical models of cavitation. Although the X-ray densitometry measurements show that the cavity is a bubbly mixture with varying void fraction rather than a single cavity full of vapor (Stutz & Legoupil 2003; Coutier-Delgosha et al. 2007; Ganesh et al. 2016), the internal vapor/liquid structure is still unclear. It is usually assumed in the numerical cavitation models that the cavity consists of a large number of individual bubbles with a spherical shape, so that the Rayleigh-Plesset equation can be used (Schnerr & Sauer 200; Singhal et al. 2002). However, Coutier-Delgosha et al. (2006) made the first attempt to visualize the two-phase morphology inside a sheet cavity by means of an endoscopic device. They observed that the vapor/liquid structure varies significantly along the cavity length and most of the bubbles do not have a spherical shape, contradicting the hypothesis in the numerical models.

An accurate description of cavitation physics strongly relies on visualizing and quantifying the cavitating regions. The major challenge in experimental measurements of cavitating flow fields is the fact that multiple scattering and direct reflection of visible light from phase boundaries make the flow optically opaque. Although local measurements using various probes have been proven to be able to provide qualitative and quantitative information inside the two-phase region (Pham et al. 1999; Stutz & Reboud 1997, 2000; Coutier-Delgosha et al. 2006), these probes may perturb the flow field. Different from single-point/intrusive probe measurements, Particle Image Velocimetry (PIV) enables a whole-field acquisition of velocity with little perturbation on the flow. When applied in cavitating flows, the strong scattering and reflection from the cavitation structure will obscure the scattering light from the surrounding tracer particles. This contaminating effect can be avoided by injecting laser-induced fluorescent (LIF) particles, i.e. PIV-LIF technique. However, the issues associated with cavitation opacity still exist. Therefore, most PIV-LIF measurements have focused on the liquid

flow regions outside the cavity (Laberteaux & Ceccio 2001; Foeth et al. 2006; Kravtsova et al. 2014) or turbulent cavitating wake regions with low void fraction (Iyer & Ceccio 2002; Aeschlimann et al. 2011a).

X-rays can penetrate most optically opaque media with weak interactions owing to their much shorter wavelength than visible light. This distinct advantage makes X-ray imaging a powerful method to visualize and characterize multiphase flows (Heindel 2011). X-ray imaging is a line-of-sight (shadowgraphy) technique, recording a 2D projection of a 3D object placed between an X-ray source and a detector (Poelma 2020). X-ray beam can be produced in two types of devices: a tube source and a synchrotron. A detailed comparison between these two kinds of X-rays and the corresponding measurements for multiphase flows is provided by Heindel (2018). For cavitating flows, the tube source X-ray attenuation technique is used to measure local void fraction because of the absorption difference between water and vapor. Stutz & Legoupil (2003) applied firstly the X-ray densitometry to cloud cavitation formed in a Venturi-type test section. They found that the mean void fraction varies regularly from 25% at the upstream end of the mean cavity to 10% in the downstream part. Similar applications of X-ray attenuation to cavitating flows can be found in Coutier-Delgosha et al. (2007) and Aeschlimann et al. (2011b). In recent works (Ganesh et al. 2016; Wu et al. 2019), instantaneous void fraction fields obtained by the time-resolved X-ray densitometry revealed the propagation of condensation shock waves within a cavity, which was regarded as the dominant mechanism of periodic shedding of large vapor clouds in more developed cavitation stages.

The development of the third-generation synchrotron radiation sources promotes the application of X-ray phase-contrast imaging, which enables clear visualization of boundaries between phases with different refractive index (Kastengren & Powell 2014). The short high-flux X-ray pulses emitted from synchrotron sources allow for the capture of fast dynamic events and minimize motion blur (Bothell et al. 2020). Aside from detailed illustration of two-phase morphology (Karathanassis et al. 2018), X-ray phase-contrast images can also be used to perform velocimetry by tracking either seeded particles or phase interfaces inside the opaque regions. Using the X-ray beam at the Advanced Photon Source (APS), Im et al. (2007) greatly improved the particle image quality making single-particle tracking velocimetry possible in an opaque vessel. Wang et al. (2008) revealed for the first time the internal structures of high-speed optically dense sprays near the nozzle exit using the ultra-fast APS X-ray phase-contrast imaging technique. The velocity fields were measured by tracking the movements of the phase enhanced liquid–gas boundaries. The first attempt to measure velocity field inside a sheet cavity using X-ray phase-contrast imaging was described by Coutier-Delgosha et al. (2009). Later Khlifa et al. (2017) improved the experiment procedures enabling a simultaneous acquisition of instantaneous void fraction and velocity fields. The present study is an extension of these two works.

The aim of this paper is to offer a detailed description of the two-phase structures and dynamics in a quasi-stable sheet cavitation. The studied partial cavity is formed in a convergent-divergent (Venturi) channel with a small contraction ratio where the relatively stable cavitation regime can be sustained in a wide range of cavitation numbers. The fast synchrotron X-ray imaging, based on a combined mechanism of absorption and phase contrast, captures the fine two-phase morphological features inside the sheet cavity and visualizes clearly the seeded tracer particles. Through appropriate post-processing to the recorded X-ray images of cavitation, the time-resolved velocity and void fraction fields are obtained simultaneously. Based on the unprecedented experimental data, we challenge the current prevailing explanation to the stable sheet cavitation by confirming the constant existence of a low-speed re-entrant flow underneath the cavity and its role in the complex two-phase flow structures of stable sheet cavitation. Finally, the experimental results have also been used to make a preliminary analysis of cavitation-turbulence interactions.

## 2. Experimental setup and methods

### 2.1. *Hydraulic test rig*

The studied sheet cavitation is generated in the throat region of a small size Venturi-type test section, which is connected into a portable hydraulic loop designed by Coutier-Delgosha et al. (2009). As shown in Fig. 1(a), the flow rate is controlled by a frequency inverter connecting a circulating pump. A secondary recirculation loop is added for attaining small flow rate while avoiding the pump operating in unstable conditions. Cavitation levels can be set properly by regulating the pressure on the free surface of the tank by means of a vacuum pump. A heater combined with a cooling system is employed enabling the flow temperature to stabilize at a given value measured by a thermocouple located upstream of the test section.

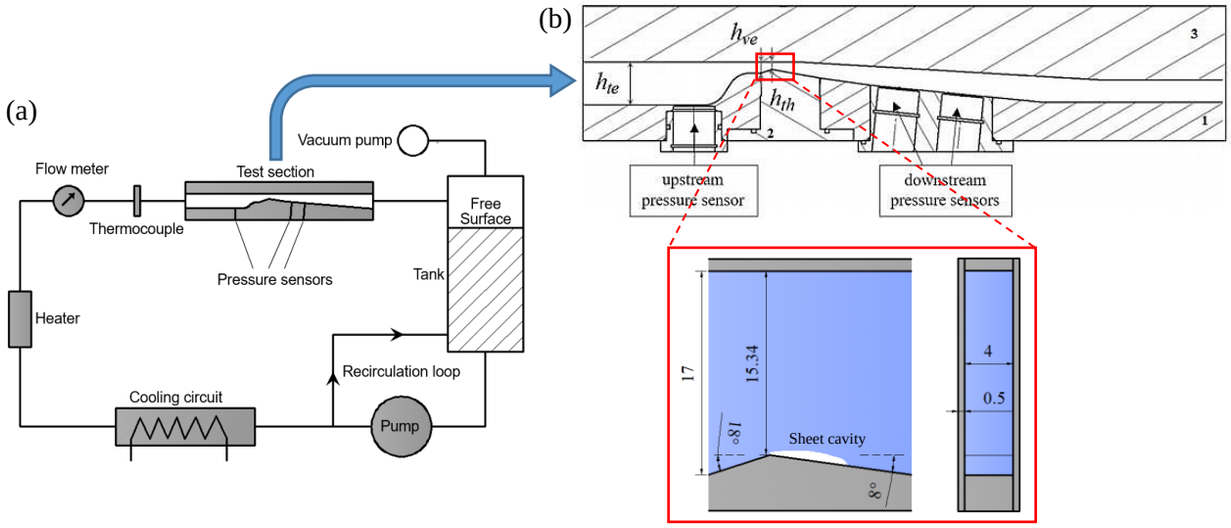


**FIG. 1.** (a) Schematic diagram of the hydraulic loop. (b) Profile of the Venturi-type test section; flow is from left to right; the close-up shows the main dimensions of the convergent-divergent section (in mm).

The overall test section being 30 cm long is presented in Fig. 1(b). The lower part (2) is inserted into the bottom wall (1) forming the Venturi-type flow channel, with the confinement of the top wall (3). The Venturi has a rectangular cross section and is characterized by a convergent angle of 18° and a divergent angle of 8°. The width of the flow passage is 4 mm. The height $h_{\mathrm{ve}}$ at the Venturi entrance is 17 mm with $h_{\mathrm{th}}$ = 15.34 mm at the throat producing a small contraction ratio of 1.1. The height $h_{\mathrm{te}}$ of the test section entrance is 31 mm. The thickness of each Plexiglas side wall is reduced as less as 0.5 mm in order to decrease X-ray energy absorbed by non-fluid parts. Three pressure transducers are flush mounted on the bottom wall of the test section. The upstream one is used to determine the inlet pressure $P_{\mathrm{in}}$ for calculating the free-stream cavitation number $\sigma$:

$$\sigma = \frac{P_{\mathrm{in}} - P_{\mathrm{vap}}}{\frac{1}{2}\rho u_{\mathrm{in}}^2} \tag{1}$$

where $P_{\mathrm{vap}}$ is the vapor pressure at the flow temperature, $u_{\mathrm{in}}$ is the average velocity at the cross section of upstream pressure sensor and $\rho$ is the liquid density. The average velocity is computed according to the volume flow rate measured by a flow meter with a 2% reading uncertainty. The pressure sensors are calibrated in a range of 0–3 bar with a full scale uncertainty of 0.25%. The accuracy of the pressure and velocity measurements leads to an uncertainty of 3.5% in the cavitation number. The two downstream sensors are used to detect possible cavity oscillations.

### 2.2. *Fast X-ray imaging technique*

The X-ray imaging in the present study is based on two different mechanisms: absorption contrast and phase contrast, as illustrated in Appendix A. The experiments were performed using the third-generation synchrotron radiation at the Advanced Photon Source (APS) where a high-energy and spatially coherent X-ray beam is available. As shown in Fig. 2(a), the X-ray source is aligned with the test section on one side and the X-ray detector (a scintillator) on the other side converting X-ray beam into visible light, which is then recorded by a high-speed CCD camera. The X-ray source emits two types of pulses with a cross section of 1.7×1.3 mm$^2$: a primary pulse with a duration of 500 ns and a secondary pulse with a duration of 100 ps. The time interval between two primary or secondary X-ray pulses is 3.68 μs. The source-to-object distance is about 60 m, and the object-to-detector distance is optimized to 50 cm for enhancing phase contrast.

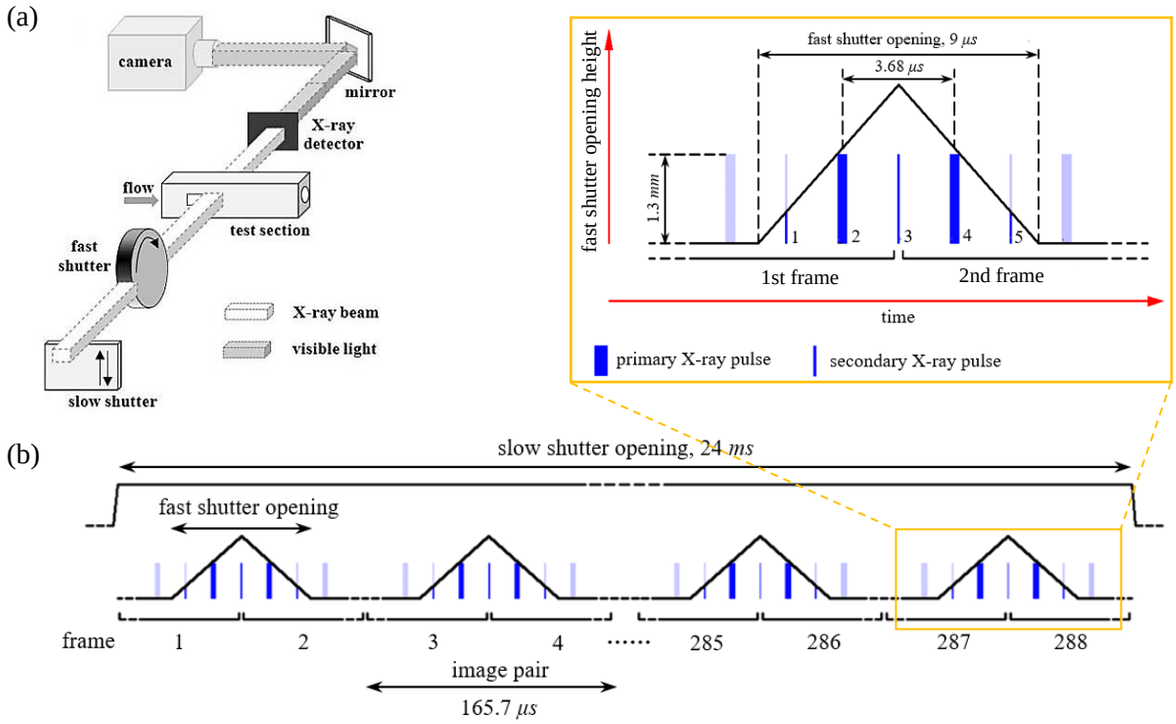


**FIG. 2.** (a) Diagram showing light path of X-ray imaging system at the APS. (b) Synchronization of the shutters, the X-ray pulses, and the camera frames to acquire appropriate image pairs for PIV analysis.

In the beamline, the slow shutter, operating at a frequency of 1 Hz with an opening time of 24 ms, is equipped to protect the test section and the detector reducing heat load on them. The fast shutter used is a mechanical rotating chopper that operates at a frequency of 6035 Hz with an opening time of 9 μs (Gembicky et al. 2005). Fig. 2(b) shows the synchronization scheme of the X-ray flashes, the two shutters, and the camera frames, to obtain appropriate pairs of images for PIV analysis. The camera frame transfer is triggered by the secondary pulse 3, such that each image in the same pair could obtain nearly identical illumination. The acquisition frequency of the camera is set to 12070 fps (twice the fast shutter operating frequency), enabling a spatial resolution of 704×688 pixels with a scale of 2 μm/pixel. It should be noted that only a packet of 144 image pairs is recorded during the opening period of the slow shutter (24 ms per second).

Silver-coated hollow glass spheres with nominal diameters of 17 μm were injected into the flow as tracers of liquid phase. The specific gravity of these tracer particles is 1.4. Because of the small cross section of the X-ray beam, successive but not simultaneous acquisitions at different positions are necessary to obtain the complete image for the flow field of

interest as shown in Fig. 3(a). To that end, the test section was moved parallel to the divergent floor of Venturi (*x*-axis) in front of the X-ray beamline by a motorized platform. At each position, 1872 pairs of images are recorded, which are actually divided equally into 13 packets (corresponding to the slow shutter opening 13 times), and thus the time between packets is not continuous.

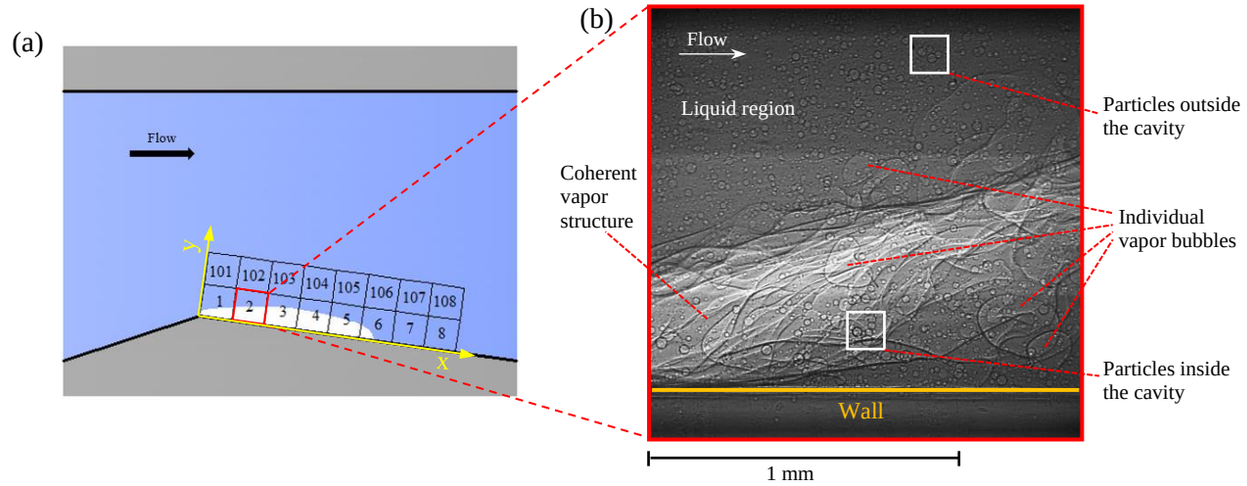


**FIG. 3.** (a) Schematic of X-ray beam scanning positions. The test section was moved to different positions enabling X-ray beam to scan the complete flow field of interest. (b) A representative raw X-ray image of cavitation recorded at the scanning window 2.

Fig. 3(b) presents a typical raw X-ray image of cavitation recorded at the second position. The bright band at the center results from extra partial exposure to a secondary X-ray pulse as indicated in Fig. 2(b). In addition to absorption contrast, the X-ray phase contrast leads to a fringe pattern with sharp intensity variation along the phase interfaces, which allows a better visualization of the two-phase flow morphology and the seeded particles. As can be found in the raw radiograph, the vapor structures in the position close to the cavity leading edge are generally coherent. The seeded particles both inside and outside the cavity are also visualized clearly. They are much smaller and have a relatively regular round shape, compared to individual vapor bubbles.

## 3. Quantitative data extraction based on image post-processing

Although the two-phase information is contained simultaneously in the X-ray images, the transition from visualization to quantitative measurements (e.g. velocity and void fraction fields) is not easy. In the conventional PIV images, a high signal-to-noise ratio (hence a distinct cross correlation peak) is achieved by large contrast in gray levels between particles and liquid background as the liquid can rarely scatter laser light. However, due to the relatively bright background associated with X-ray imaging mechanisms, the signal-to-noise ratio would drop greatly if the background is not removed from the X-ray image. In order to analyze the cavitation dynamics, image post-processing is required to extract the tracer particles from the background such that conventional PIV algorithms can be applied.

### 3.1. *Separation of tracer particles from X-ray image*

The preliminary attempt to separate the seeded particles could be found in Khlifa et al. (2017) where the liquid background was eliminated based on the vapor volume fraction measurements and large areas of vapor structures were removed using a high-pass filter. This image processing method was greatly dependent on the accuracy of void fraction

while the error could be ±15% according to their description if measurements of void fraction were performed using each individual image without pair averaging. In this paper, we employed a new wavelet-decomposition-based image processing method to separate the seeded particles from the non-uniform background of the liquid and the vapor structures. The detailed description of procedures of this new method is provided in Appendix B. The final result is presented in Fig. 4. The particle image [Fig. 4(b)] extracted from the raw X-ray image [Fig. 4(a)] will be used to evaluate the instantaneous velocity field of the cavitating flow. It should be noted that compared to the first attempt the same raw X-ray images were used in the present study, nevertheless this new method is not dependent on the void fraction accuracy and is much less time-consuming (approximately 1/3 processing time with the same computing resources).

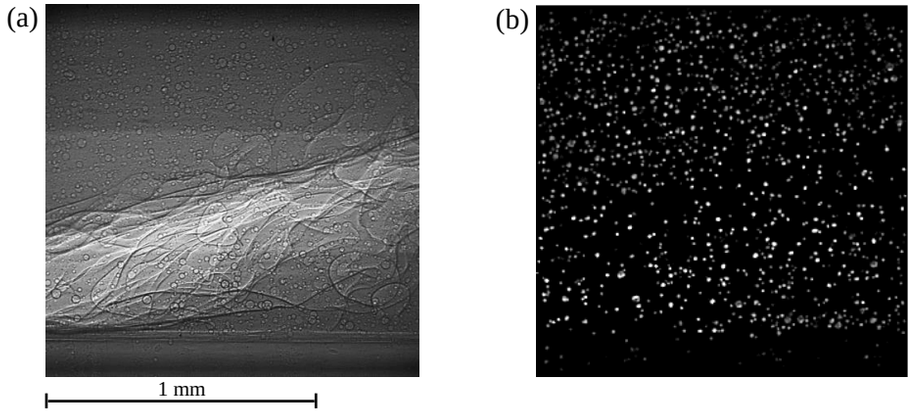


**FIG. 4.** Result of image processing for extracting particles. (a) Raw X-ray image of cavitation; (b) particle image for measurements of instantaneous velocity field.

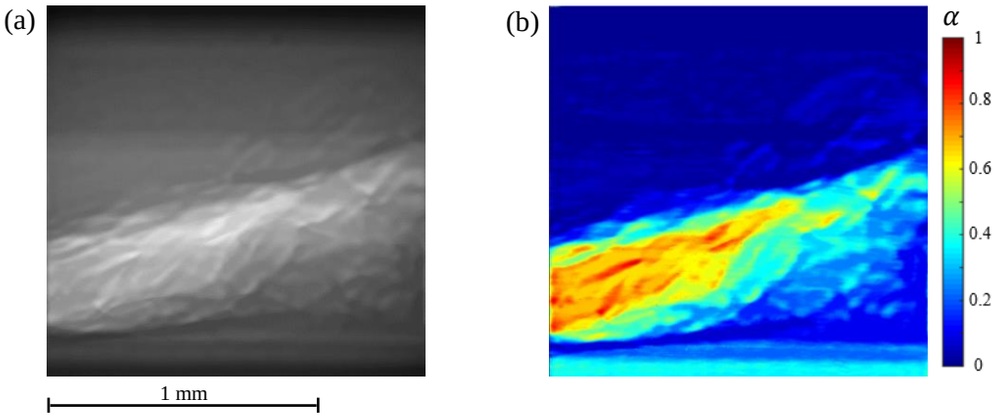


**FIG. 5.** Measurements of vapor volume fractions, (a) processed image for the computation of void fraction; (b) instantaneous vapor volume fraction field.

### 3.2. *Void fraction measurement*

The local void fraction $\alpha$ is defined as the ratio of the vapor volume to the total volume along any given beam path crossing the test section. The value represents the averaged void fraction in the spanwise direction. Since the vapor has a different X-ray attenuation coefficient from the liquid, the local vapor volume fraction $\alpha$ could be estimated quantitatively using Equation 2, derived from Lambert–Beer's law,

$$\alpha = 1 - \frac{\ln(I_0/I_\alpha)}{\ln(I_0/I_1)} \tag{2}$$

where $I_0$ is the local intensity measured when the test section is completely filled with air (for convenience, vapor is replaced by air as they almost have an identical absorption coefficient), $I_1$ is the local intensity measured when the test section is full of water, and $I_\alpha$ is the local intensity measured when cavitation occurs in the test section. For computing $\alpha$, it is necessary to take the calibration images of air and water under the same acquisition conditions as the cavitation tests. Fig. 5(a) presents a processed image used for the computation of void fraction. The aim of processing the raw image is to reduce the effect of imperfect synchronization and phase contrast fringes on void fraction measurements. The detailed processing procedures are provided in Appendix C. The final result of instantaneous void fraction field is illustrated in Fig. 5(b). The measurement uncertainty is about 2%.

### 3.3. *Particle image velocimetry*

Based on the MatPIV.1.6.1 open source toolbox, cross-correlation algorithm was applied on each pair of consecutive particle images obtained by the above image processing procedures to determine the corresponding liquid phase displacements. The time separation between the two pictures was 3.68 μs. Four interrogation passes with window offset were carried out and the interrogation window size was progressively decreased in order to increase the spatial resolution. The interrogation window for the first pass was 80×70 pixels followed by 3 passes with interrogation windows of 70×60, 60×50, and 50×40 pixels. In the final pass the correlation peak was estimated with a sub-pixel accuracy by using the three-point Gaussian fitting scheme in two directions. Fig. 6 shows an instantaneous velocity field of the liquid phase evaluated through the above cross-correlation algorithm, in which the aberrant vectors detected by median test were rejected and then replaced by bilinear interpolation from their valid neighboring vectors. The two ends where illumination is not sufficient were excluded. Each pair of processed particle images produced 26×31 instantaneous local velocity vectors spaced equally by 22pixels (44 μm) in the field of view.

The uncertainty of the velocity measurements was estimated by generating synthetic images of a cavitating flow with imposed particle displacements as discussed in detail in Khlifa et al. (2017). The comparison between imposed and measured values shows that the mean error of the liquid phase velocity measurements is around ± 0.46 m/s (approximately 5% of the reference velocity of the studied flow).

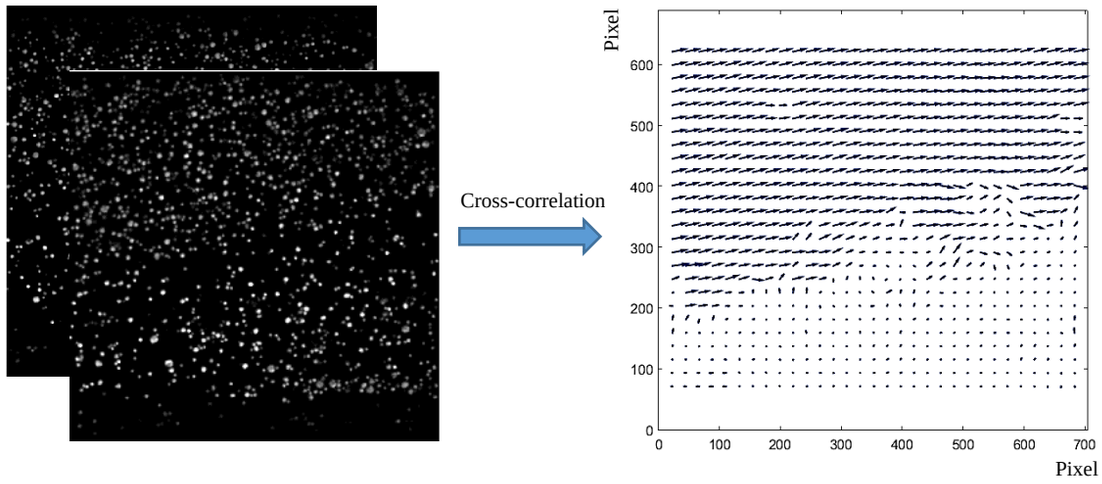


**FIG. 6.** Instantaneous velocity vector field evaluated by cross-correlation from a pair of processed particle images.

### 3.4. *Comparison between conventional laser PIV and X-ray PIV*

Unlike the standard PIV measurements illuminating particles in a plane with a thin laser sheet, all particles and bubbles along the beam path are projected into the X-ray image due to the line-of-sight nature associated with the X-ray imaging method. Therefore, the standard PIV result represents a 2D velocity field in the illuminated plane while the X-ray PIV result is a span-averaged velocity field containing accumulated flow information in the spanwise direction. Lee & Kim (2003) reported the velocity profile in an opaque circular pipe measured by the X-ray PIV method, where the measured velocity at the pipe center is only two-thirds of the theoretical value. This discrepancy is attributed to the three-dimensionality of the laminar flow boundary layer, given a flow with a mean velocity of 0.5 mm/s in a 750μm tube.

Both the laser and X-ray PIV measurements, under the non-cavitating condition with an average velocity of 15 m/s at the throat, were carried out in the present Venturi-type test section in order to examine the two-dimensionality of the flow. The central plane of the Venturi channel was illuminated by a thin laser sheet of 1 mm thickness, thereby allowing 2D velocity measurements less affected by the two side walls. As shown in Fig. 7, the mean streamwise velocity profiles measured by the standard PIV and the X-ray PIV are compared quantitatively with each other at two different distances from the Venturi throat ($x$=8 mm and $x$=14 mm). Note that the $x$-axis is along the Venturi divergent floor and the origin is located at the apex of the Venturi throat (indicated in the inset of Fig. 7). As can be seen, the velocity profile acquired by X-ray agrees well with the standard PIV result away from the bottom wall indicating the flow is almost two dimensional in this region. This is due to the fully turbulent flow producing relatively thin boundary layers on the two side walls. Nevertheless, the velocity difference adjacent to the bottom wall is relatively high indicating a certain extent of three dimensionality of the flow in this region, which might be caused by corner flows and relatively thick boundary layers on the two side walls.

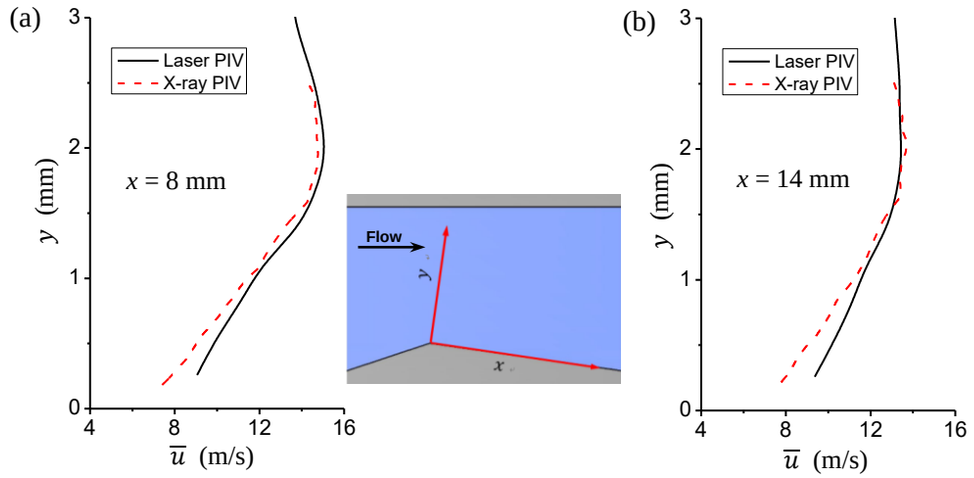


**FIG. 7.** Comparison of mean streamwise velocity ($\overline{u}$) profiles at two locations measured by the standard PIV and the X-ray PIV in the non-cavitating condition, (a) $x$=8 mm; (b) $x$=14 mm.

## 4. Results and discussion

In the present experiments, the flow temperature was kept constant at 17 ± 0.5 °C and the flow rate $Q$ was set to 35.09 l/min leading to a reference velocity $u_{\mathrm{ref}}$ = 9.53 m/s at the Venturi throat. The variation of cavitation number was achieved by adjusting the inlet pressure. The cavitation pattern observed does not exhibit a significant change with the reduction of cavitation number. In other words, the cavitating flow in this specific small-contraction-ratio Venturi geometry is

characterized by a quasi-stable sheet cavitation. Three cases with different cavitation numbers ($\sigma$ = 7.54, 8.0 and 9.13) were tested. They correspond to the developed stage, the intermediate stage and the early stage of sheet cavitation, respectively. As they all exhibit the similar flow characteristics, only the data of the developed stage is discussed in the follwing sections.

### 4.1. *Global behavior of sheet cavitation based on high speed photography*

The cavitating flow in the convergent-divergent channel was captured from side view using a high-speed Photron Fastcam SA 1.1 camera with a Tokina 100mm lens. The flow was illuminated by a high-power LED from top. The frame rate was set to 8000 fps with a short exposure time (1/50000 s) to freeze the fast-moving vapor structures. The spatial resolution was 1024 × 512 pixels with each pixel corresponding to 24 μm.

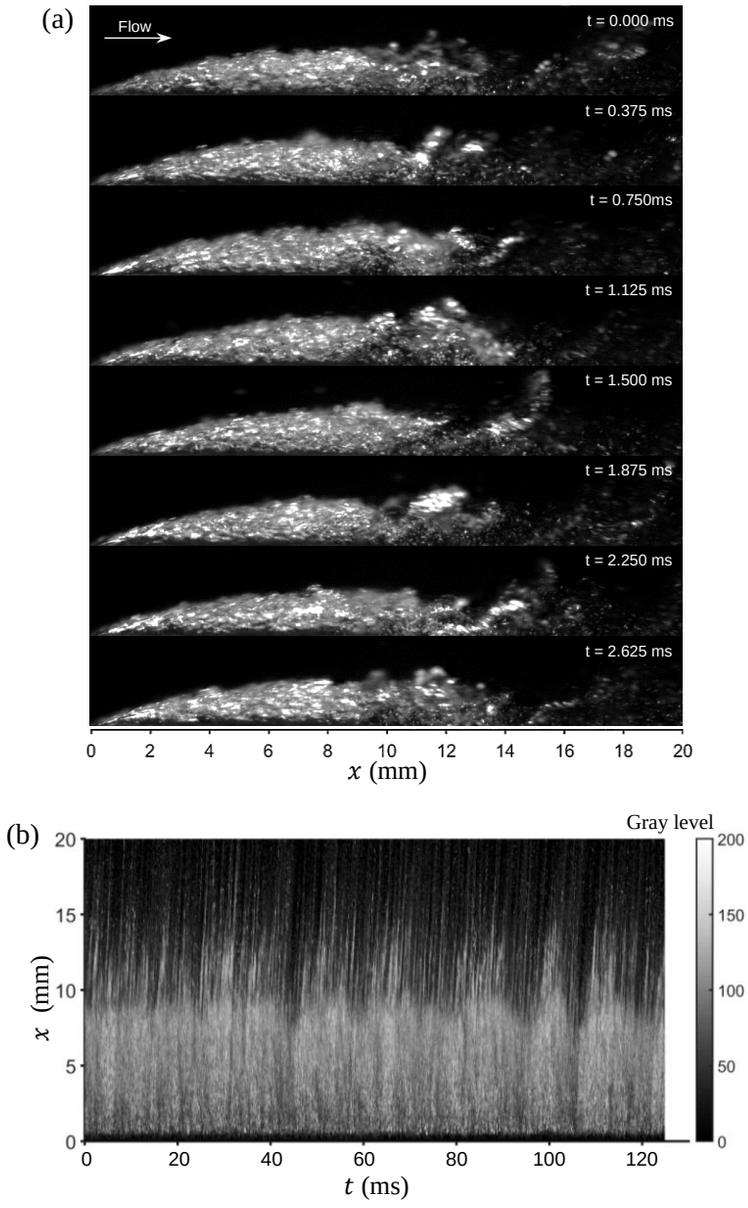


**FIG. 8.** (a) A sequence of high-speed photographs for the cavitating case of $\sigma$ = 7.54. (b) Time-space ($t$-$x$) diagram derived from 1000 consecutive cavitation snapshots for $\sigma$ = 7.54.

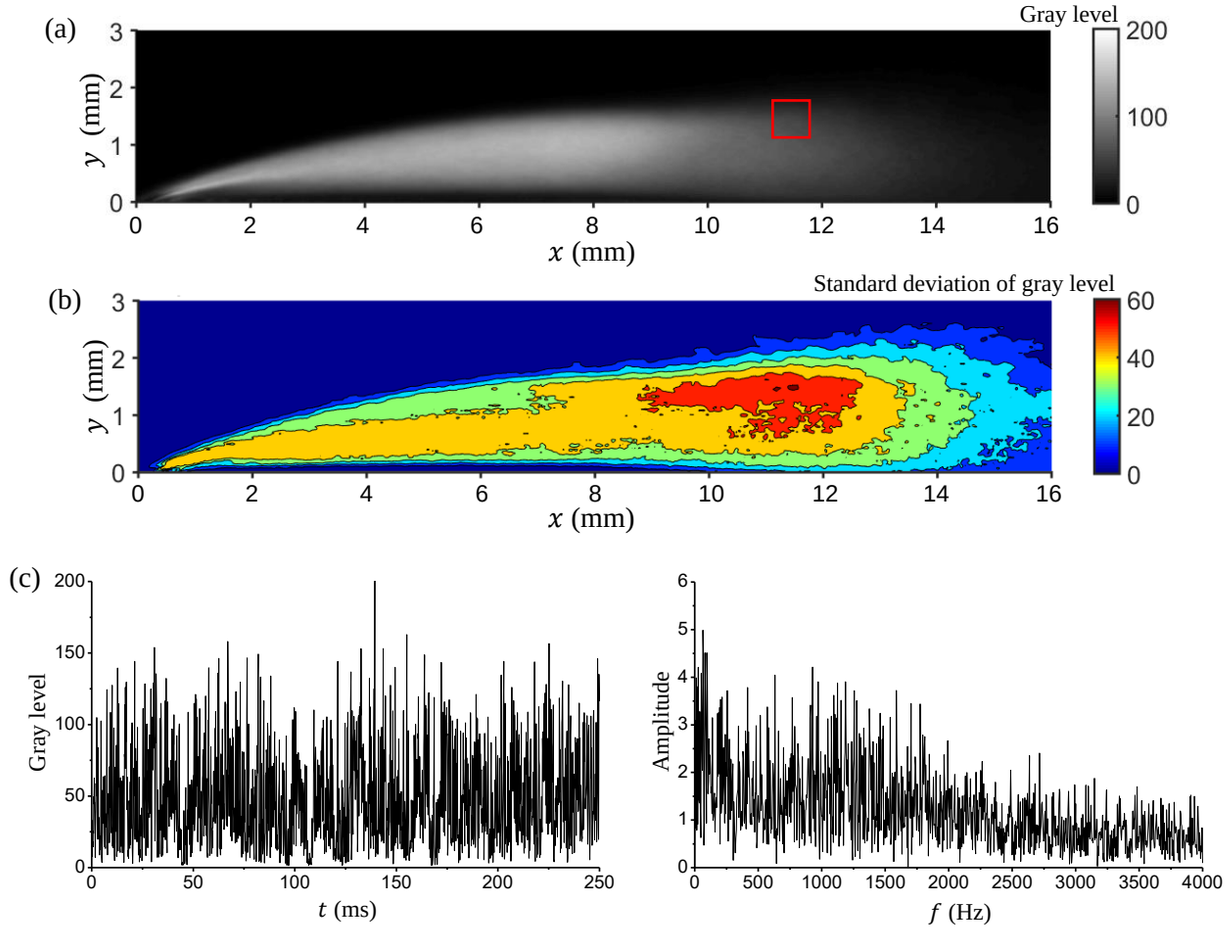


**FIG. 9.** Gray level examination for $\sigma$ = 7.54. (a) Mean gray level values of 2000 high speed images; (b) standard deviations of gray levels; (c) time evolution of gray level in the probing window (indicated by the red frame in (a)) and its FFT result.

As the cavitation number decreases, the cavitating region grows and the liquid-vapor interface becomes increasingly wavy and unstable. However the classical periodic shedding of large vapor clouds is not observed in the present geometry. Fig. 8(a) shows a sequence of high speed images for the case of $\sigma$ = 7.54. From these images, an open partial cavity is observed with a turbulent frothy closure. The beginning of the cavity is located close to the Venturi throat ($x$ = 0). The main part ($x$ = 0-10 mm) appears to attach to the solid surface steadily. Small-scale vapor structures are rolled up and shed continuously from the cavity closure region ($x$ = 10-12 mm). As these vapor structures are convected downstream, they rapidly split and/or collapse into a large number of very small bubbles in the cavity wake region ($x$ >12 mm).

The time-space ($t$–$x$) diagram is a useful data processing method to illustrate unsteady cavitation behaviors. Gray levels in each high speed photograph is averaged along the $y$ axis generating a column of the $t$–$x$ diagram. Fig. 8(b) presents the $t$–$x$ diagram for $\sigma$ = 7.54 which is obtained by stacking 1000 consecutive snapshots of cavitation. It is clear that the main part ($x$ = 0-10 mm) of the cavity is fairly stable while vapor structures are shed after $x$ = 10 mm in an irregular fashion.

As shown in Fig. 9(a) and (b), mean values and standard deviations of gray levels of 2000 images were calculated in order to determine the cavity length and analyze the shedding frequency content. The method of estimating the cavity length from the mean gray level image is not accurate since it is too subjective to choose the threshold value. Dular et al. (2004) found that the position of the maximum standard deviation of gray level is correlated well with the position of maximal cavitation structure oscillation. Therefore, one can consider the location of the maximum standard deviation as

the sheet cavity termination. In recent years, this method has been widely used as could be found in Danlos et al. (2014), Prothin et al. (2016), Long et al. (2017) and Zhang et al. (2019). In our case, the maximum standard deviation is identified at the point of $x$ = 11.5 mm, $y$ = 1.5 mm and thus the mean cavity length is determined to be 11.5 mm. Another reliable method is to use the contour line of $\alpha$ = 0.1 in the time-averaged void-fraction field to designate the mean cavity length. As shown in Fig. 10(a), the cavity length is around 11.5 mm. This good agreement demonstrates that it is reasonable to use the standard deviation method to determine the cavity length. Moreover, the maximum standard deviation is also an objective way to select the probing window for estimating the cavity shedding frequency. The time evolution of gray level in Fig. 9(c) is obtained by averaging all gray level values in a 50×50 pixel probing window with its center at the position of the maximum standard deviation. From its Fast Fourier Transform (FFT) result, no characteristic frequency is detected implying that the small vapor shedding from the cavity closure occurs in an irregular way.

So far the mainstream explanation to the relatively stable sheet cavitation is that no re-entrant jet exists underneath the cavity or the re-entrant jet only exists near the cavity closure region, thereby producing intermittent shedding of small vapor structures. The conjecture of lacking re-entrant flow is considered as the primary mechanism causing the main part of the sheet cavity attaching to the wall steadily. In the next sections, we will challenge this conjecture by the X-ray imaging measurements and illustrate how the seemingly stable sheet cavitation is linked to a clear re-entrant flow penetrating the entire sheet cavity.

### 4.2. *Mean void fraction and velocity fields based on X-ray imaging measurements*

Since the time-resolved acquisitions by X-ray imaging are not simultaneous at different positions, it is impossible to analyze the complete instantaneous flow field. Nevertheless, the time-averaged flow field at each position can be connected well with each other. Fig. 10(a) presents the distribution of the mean void fraction $\overline{\alpha}$ assembled from 22 scanning windows (10 in the upper row and 12 in the lower row). The averaged void fraction profiles at different distances from the throat are overlaid on the mean cavity shape in gray scale as shown in Fig. 10(b). The maximum mean void fraction is found to be at the point close to the cavity origin with a value of 75%, while the maximum instantaneous value can be up to 100%, implying that a pure vapor pocket is likely to exist in the leading edge of the cavity. A drastic decrease of void fraction down to nearly 0 is detected towards the solid surface, which is not revealed well by the gray level variation from high speed photographs.

The maximum mean void fraction in the transverse direction is plotted in Fig. 10(c), and it illustrates clearly the spatial evolution of the mean void fraction along the flow direction. The evolution of the standard deviation of void fraction $\alpha'$ is also plotted in the same way. In the region of $x$ = 0-4 mm, the mean void fraction is rapidly decreased from the maximum value 75% to 20%. Thereafter, it reduces progressively from 20% to 0 in the cavity wake at a much slower rate. The void fraction evolution along the streamwise direction in the present sheet cavity is quite different from the one reported by Coutier-Delgosha et al. (2006): in their unsteady configuration, the void fraction is rather constant in the entire attached cavity. With regard to the evolution of the standard deviation of void fraction, the maximum value is found to be in the range of $x$ = 1-2 mm, where is far away from the location of maximum standard deviation of gray level ($x$ = 11.5 mm). The explanation to this great disparity is the fact that the gray level of high speed images can only indicate the presence of cavitation structures in most cases, whereas it is poorly related to the void fraction. Surprisingly, the standard deviation of void fraction remains nearly constant at the value of 0.1 in a wide range of $x$ = 4-12 mm before it begins to decrease. The standard deviation is observed to be greater than the mean void fraction after $x$ = 11.5 mm, which is attributed to the rapid collapse of shedding vapor structures causing a relatively large void fraction fluctuation.

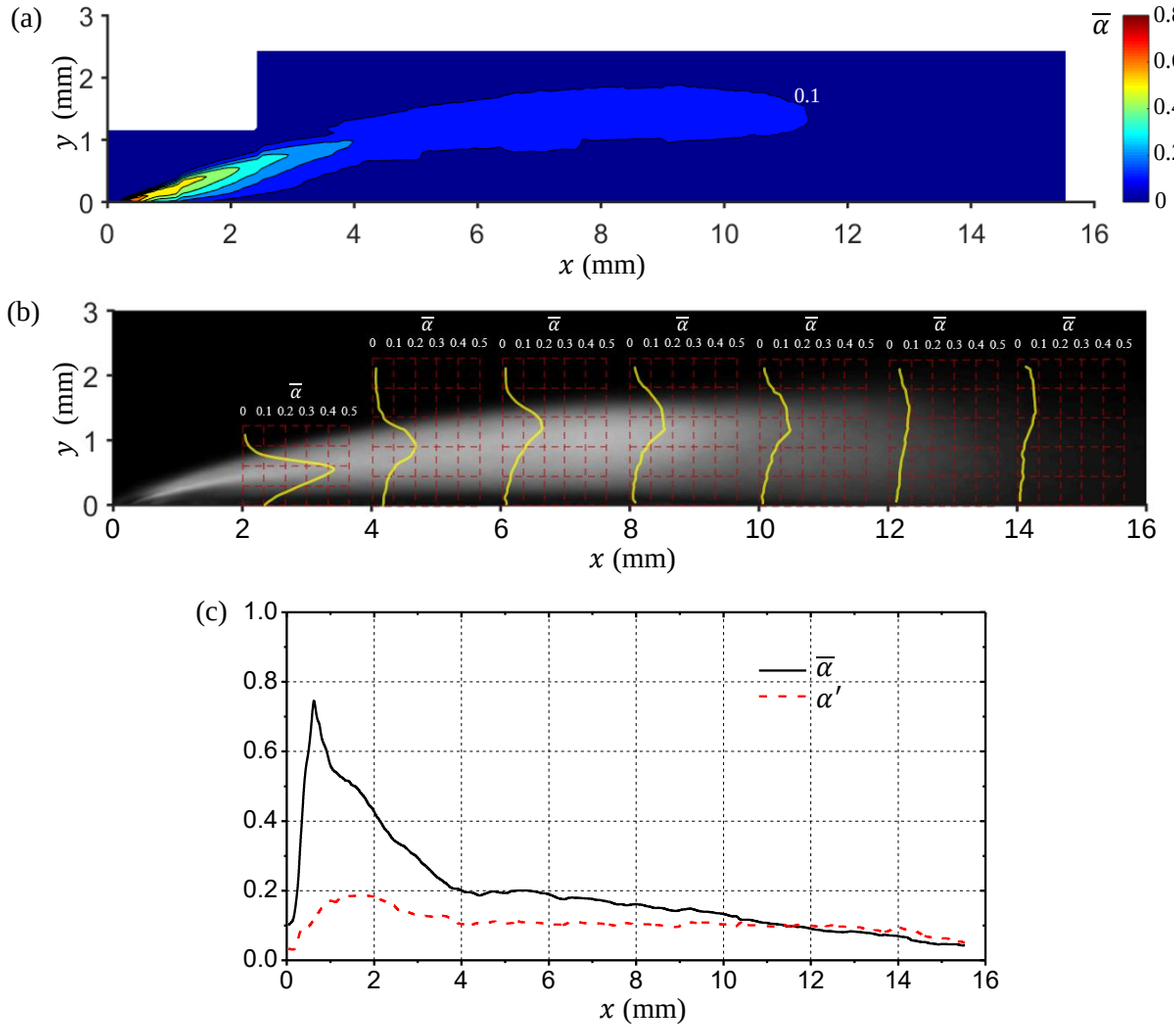


**FIG. 10.** (a) Distribution of the mean void fraction $\overline{\alpha}$ for $\sigma$ = 7.54; (b) mean void fraction profiles overlaid on the mean cavity shape for $\sigma$ = 7.54; (c) evolution of the mean void fraction $\overline{\alpha}$ and the standard deviation of void fraction $\alpha'$ along the streamwise direction for $\sigma$ = 7.54.

Fig. 11(a) shows the spatial distribution of the time-averaged longitudinal velocity $\overline{u}/u_{\mathrm{ref}}$ normalized by the reference velocity . The contour lines of $\overline{u}/u_{\mathrm{ref}}$ = 0 and 1 are superimposed on the mean void fraction field as shown in Fig. 11(b). Based on these two figures, the following results can be obtained in a statistical sense. The region under the contour line of $\overline{u}/u_{\mathrm{ref}}$ = 0 indicates the existence of a reverse flow along the wall. This upstream flow beneath the cavity is traditionally termed as a re-entrant jet. But in the present studied case, it is more accurate to call it a re-entrant or reverse flow (see Sect. 4.3). The thickness of the reverse flow remains quite constant in the range of $x$ = 4-12 mm. It can be seen that a large portion of the cavity has already detached from the wall under the displacement of the re-entrant flow, leaving only the very upstream part attaching to the wall. A strong velocity shear layer is formed between the reverse flow and the outer main flow. The vapor content is mainly concentrated within this shearing area. The local low pressure induced by the coherent vortical motions in this shear layer might prevent the bubbly mixture from collapsing immediately after detaching from the wall, and thus contributes to the formation of a long tail-like cavitation structure. The upstream end of the re-entrant flow is located at $x$ = 1.5 mm where corresponds to the position of the maximum standard deviation of void fraction, suggesting that the re-entrant flow can cause phase change and hence plays a crucial role in the void fraction variations.

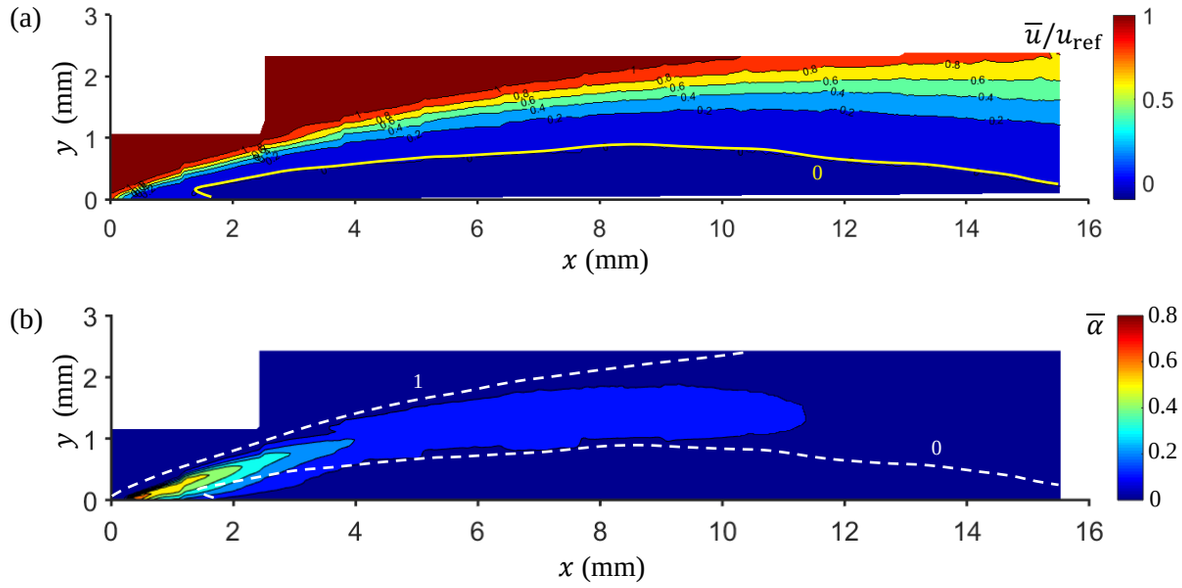


**FIG. 11.** (a) Distribution of the time-averaged longitudinal velocity $\overline{u}/u_{\mathrm{ref}}$ for $\sigma$ = 7.54. The yellow line highlights the contour line of $\overline{u}/u_{\mathrm{ref}}$ = 0; (b) mean void fraction field on which the contour lines of $\overline{u}/u_{\mathrm{ref}}$ = 0 and 1 are overlaid to indicate the mean reverse flow and the external main flow.

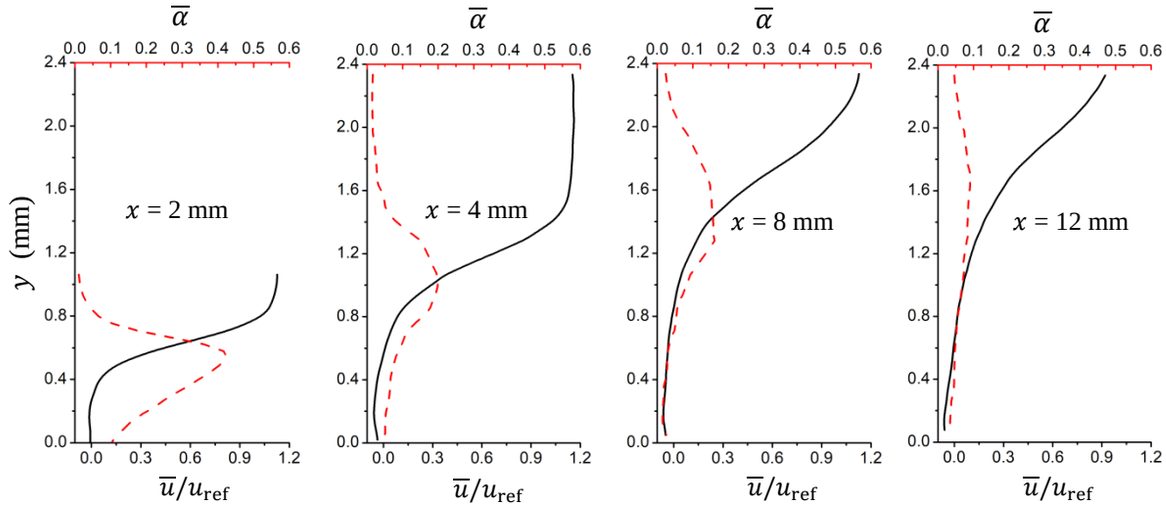


**FIG. 12.** Comparison of the mean void fraction profiles (red dashed line) and the mean longitudinal velocity profiles (black solid line) at different distances from the throat for $\sigma$ = 7.54.

The profiles of the mean void fraction and the mean longitudinal velocity are compared in Fig. 12 at different distances from the throat. The maximum void fraction is found to be located in the shear layer between the re-entrant flow and the main flow. More specifically, it corresponds generally to the location of the maximum velocity gradient. The vapor content in the reverse flow region is almost 0 demonstrating the existing knowledge that the re-entrant flow is a liquid film entraining some cavitation bubbles. The velocity in the re-entrant flow region is fairly uniform spanning the whole thickness. The time-averaged flow fields are not sufficient to characterize this complex phenomenon since cavitation is unsteady in nature. In the next two sections, we will devote to investigating the transient characteristics of the re-entrant flow and void fraction.

4.3. *Probability of the re-entrant flow*

The time-varying streamwise velocities at four positions ($x$ = 1, 2, 8 and 15 mm) along the horizontal line of $y$ = 0.1 mm (adjacent to the Venturi wall) are shown in Fig. 13. It should be clarified that due to the application of the slow shutter, only a packet of 144 pairs of images was recorded successively during each opening period (13 packets in total). Considering the time discontinuity between different packets, sample number is thus used in the time trace of streamwise velocities. Different packets are highlighted with the vertical blue dashed lines. The percentage in each subfigure represents the time fraction of negative velocity, i. e. the occurrence probability of reverse flow, and the red dashed line denotes the averaged velocity. At $x$ = 1 mm where the average velocity is positive, the occurrence probability of reverse flow is less than 50%. As expected, in the mean reverse flow region, the probability is more than 50%. A continuous presence of reverse flow is identified at $x$ = 8 mm as the probability of negative velocity there is nearly 100%.

In order to highlight the near-wall upstream moving flow, Fig. 14 provides the evolution of the probability of reverse flow along the line of $y$ = 0.1 mm. Also shown is the time-averaged longitudinal velocity. The re-entrant flow probability of 50% occurs at around $x$ = 1.5 mm where corresponds to the location of maximum standard deviation of void fraction. It suggests that the most frequent switch between positive and negative velocity leads to the largest void fraction fluctuation. The probability reaches nearly 100% at $x$ = 4 mm. This is the ultimate location the attached vapor pocket can grow to as the liquid re-entrant flow can make it detached and break up. In the range of $x$ = 4-12 mm, the probability almost remains at 100%, implying a continuous presence of the reverse flow, which is quite different from the beat behavior of the classically described re-entrant jet related to periodic cloud shedding (Callenaere et al. 2001). In the same $x$ range, the mean velocity magnitude of the reverse flow almost remains constant as well at its maximum value of approximately 0.6 m/s (7% $u_{\mathrm{ref}}$). Combined with the outer main flow, the persistence of the re-entrant flow with a constant mean velocity in this wide range leads to the formation of a steady shear layer.

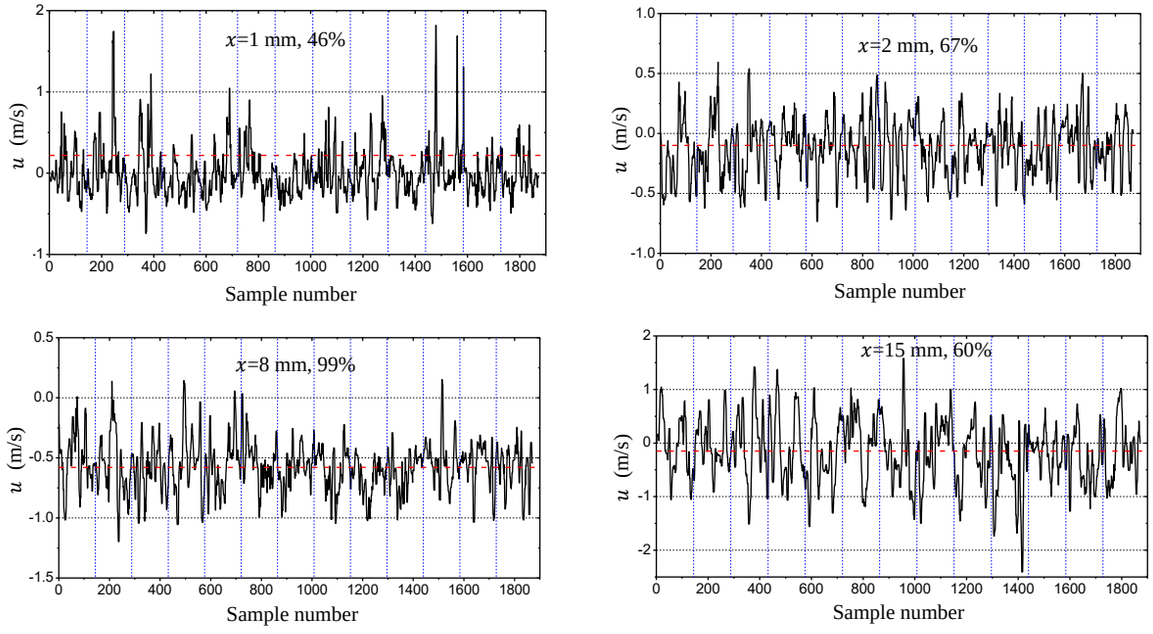


**FIG. 13.** Time-varying streamwise velocities at four locations ($x$ = 1, 2, 8 and 15 mm) along the line of $y$ = 0.1 mm for $\sigma$ = 7.54. The percentage represents the probability of negative velocity. The red dashed line denotes the averaged velocity. The vertical blue dashed lines separate different packets.

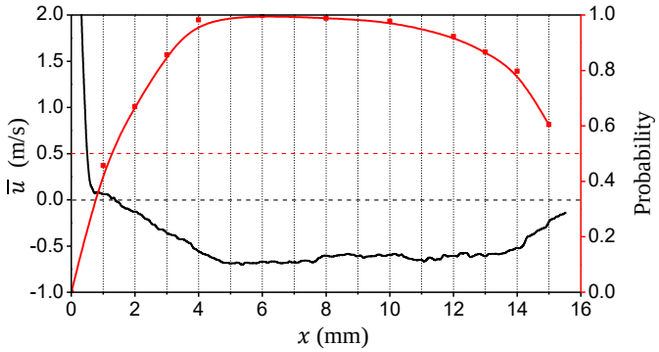


**FIG. 14.** Evolution of the occurrence probability of reverse flow (red line with squares) and the time-averaged longitudinal velocity (black line) along the horizontal line of $y$ = 0.1 mm for $\sigma$ = 7.54.

Based on the above description, a flow scenario can be conceived: the leading edge vapor pocket oscillates in a limited range of $x$ = 0-4 mm, and under the action of the re-entrant flow it detaches from the wall breaking up into a low-void-fraction bubbly mixture, which is afterwards transported downstream in the relatively steady shear layer. This explains why the mean void fraction is rapidly decreased from the maximum value 75% to 20% in the region of $x$ = 0-4 mm and then it reduces progressively from 20% to 0 at a much slower rate. It is worthwhile to note that the re-entrant flow in the present sheet cavitation regime is quite weak (the maximum value of mean velocity is only 7% $u_{\mathrm{ref}}$) in contrast to the measured velocity of re-entrant jet in periodic cloud cavitation, which is generally of the same order of magnitude as the free-stream velocity (Le et al. 1993; Pham et al. 1999). This might be the primary mechanism for sheet cavitation to remain in a quasi-stable state.

### 4.4. *Spectral analysis of void fraction variation*

In this section we will determine whether the upstream vapor pocket is oscillating randomly or regularly. To that end, two probe locations close to the cavity leading edge are selected for examining the time-varying void fraction. The first probe location is indicated in Fig. 15(c) by a yellow frame that is actually included in the X-ray beam scanning position 1 (the numbering system of scanning positions can be found in Fig. 3 and 18). Fig. 15(a) shows the time history of spatially averaged void fraction in the first probe location. Due to the aforementioned reason, only the first packet of 144 samples (corresponding to a duration of 24 ms) is presented here. Taking the packet-to-packet difference into account, all the 13 packets of spectra are averaged and the mean spectrum is shown in Fig. 15(b). As can be seen, there exists a single spectral peak at approximately 167 Hz indicating that the void fraction in the first probe location varies in a quasi-periodic pattern rather than randomly. Then let us examine the second probe location that is indicated in Fig. 16(c) by a yellow frame (in the scanning position 2). Just like for the first probe, only the void fraction variation in the first packet is presented in Fig. 16(a), and the average of the 13 spectra obtained from the 13 packets is shown in Fig. 16(b). A dominant frequency is also identified at 167 Hz, which is consistent with the one obtained in the first location. Since the void fraction in both probe locations varies regularly at the same dominant frequency, it is reasonable to speculate that the upstream vapor pocket oscillates quasi-periodically at around 167Hz. Note that the frequency resolution, defined as sampling frequency/sample length, is 42 Hz.

X-ray images at five typical time instants are shown in Fig. 15(c) for the scanning position 1 and in Fig. 16(c) for the scanning position 2. It is clear that the very upstream part of the cavity is characterized by an attached vapor pocket that is fed by intense vaporization at its upper interface with the liquid flow. Through the deformation of the vapor pocket boundary,

one can identify the front of the re-entrant flow, whose appearance is distinctly different from the condensation shock front described by Ganesh et al. (2016) and Budich et al. (2018). As the re-entrant flow moves upstream along the wall, the vapor pocket shrinks and transitions into a low-void-ratio bubbly mixture. As shown in Fig. 15(c), the re-entrant flow already extends to the vicinity of the Venturi throat at the instant $t_3$ almost leading the vapor pocket to disappear. It is interesting to note that the re-entrant flow in the studied sheet cavitation can almost penetrate the entire cavity, like in cloud cavitation, but we never observe that it pinches off the cavity forming the shedding of large vapor clouds. This might be attributed to the re-entrant flow having insufficient momentum.

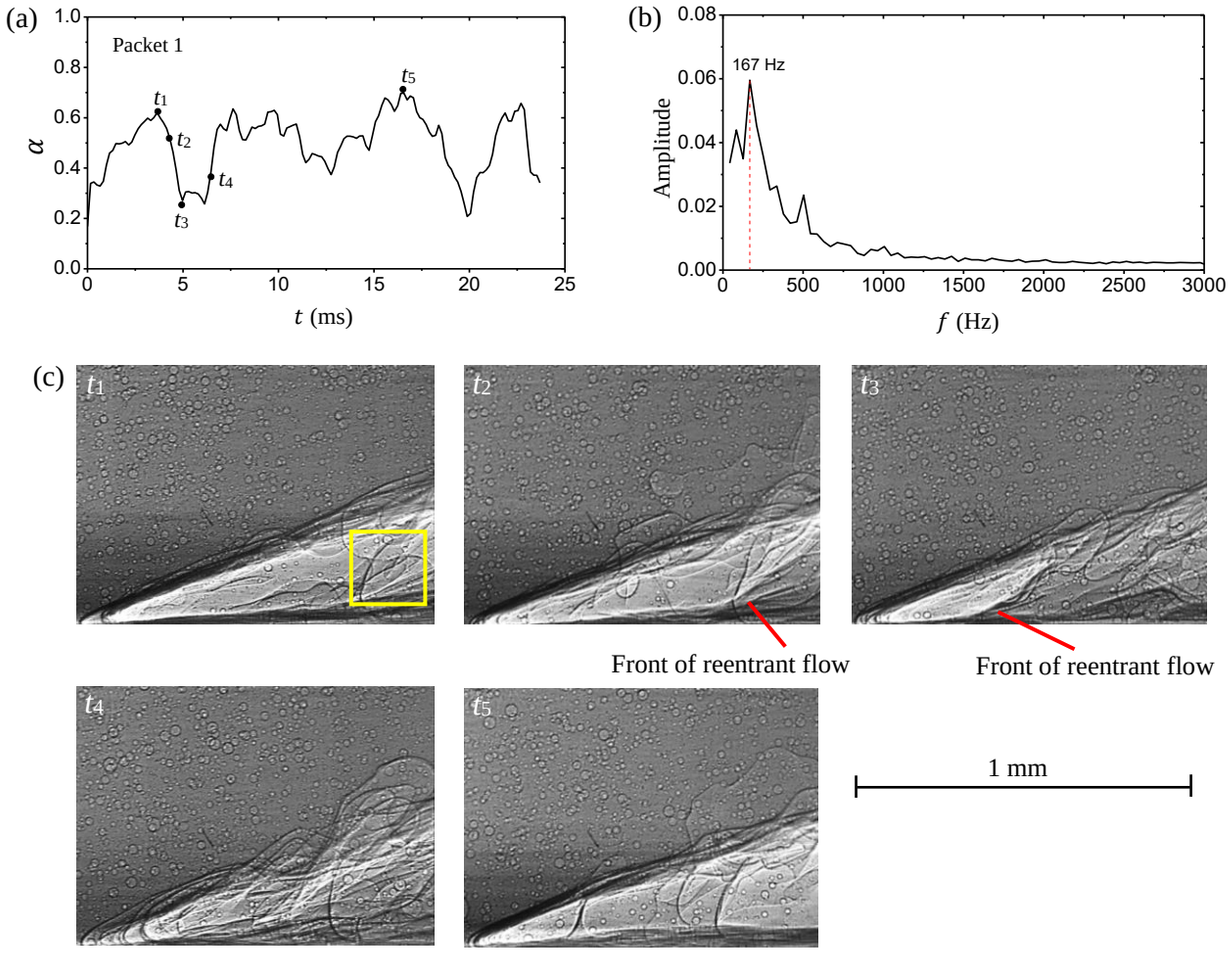


**FIG. 15.** Examination of void fraction in the X-ray scanning position 1 for $\sigma$ = 7.54, (a) time-varying void fraction in the first probe location indicated by the yellow frame in (c); (b) average of all the spectra of 13 packets; (c) X-ray images at five typical time instants.

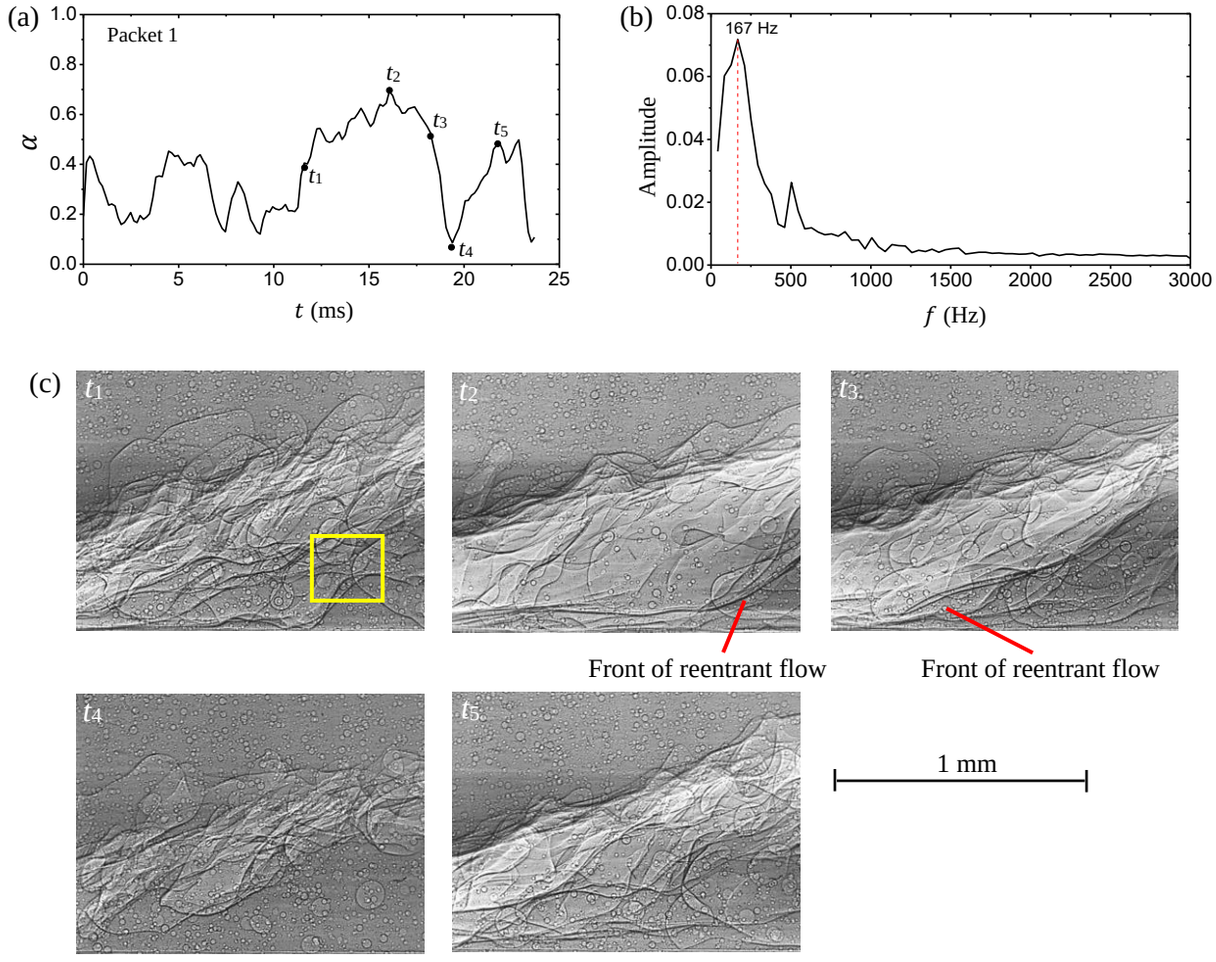


**FIG. 16.** Examination of void fraction in the X-ray scanning position 2 for $\sigma$ = 7.54, (a) time-varying void fraction in the second probe location indicated by the yellow frame in (c); (b) average of all the spectra of 13 packets; (c) X-ray images at five typical time instants.

The void fraction variation with time in the shear layer is also investigated. Fig. 17(a) shows the time trace of void fraction in the third probe location which is included in the scanning position 107. The average of all the spectra of 13 packets is shown in Fig. 17(b). As shown in the mean spectrum, multiple spectral peaks with comparable amplitude can be recognized and high-frequency content of the void fraction fluctuations increases considerably in comparison with the spectra obtained in the upstream region, which implies that the cavitation structure within the shear layer varies fast in a chaotic manner. The X-ray images at five typical instants in Fig. 17(c) reveal the constant presence of the bubbly mixture in the probe position. Due to high velocity gradient in the shear layer, the coherent vapor bubbles are distorted into a large variety of shapes and sizes.

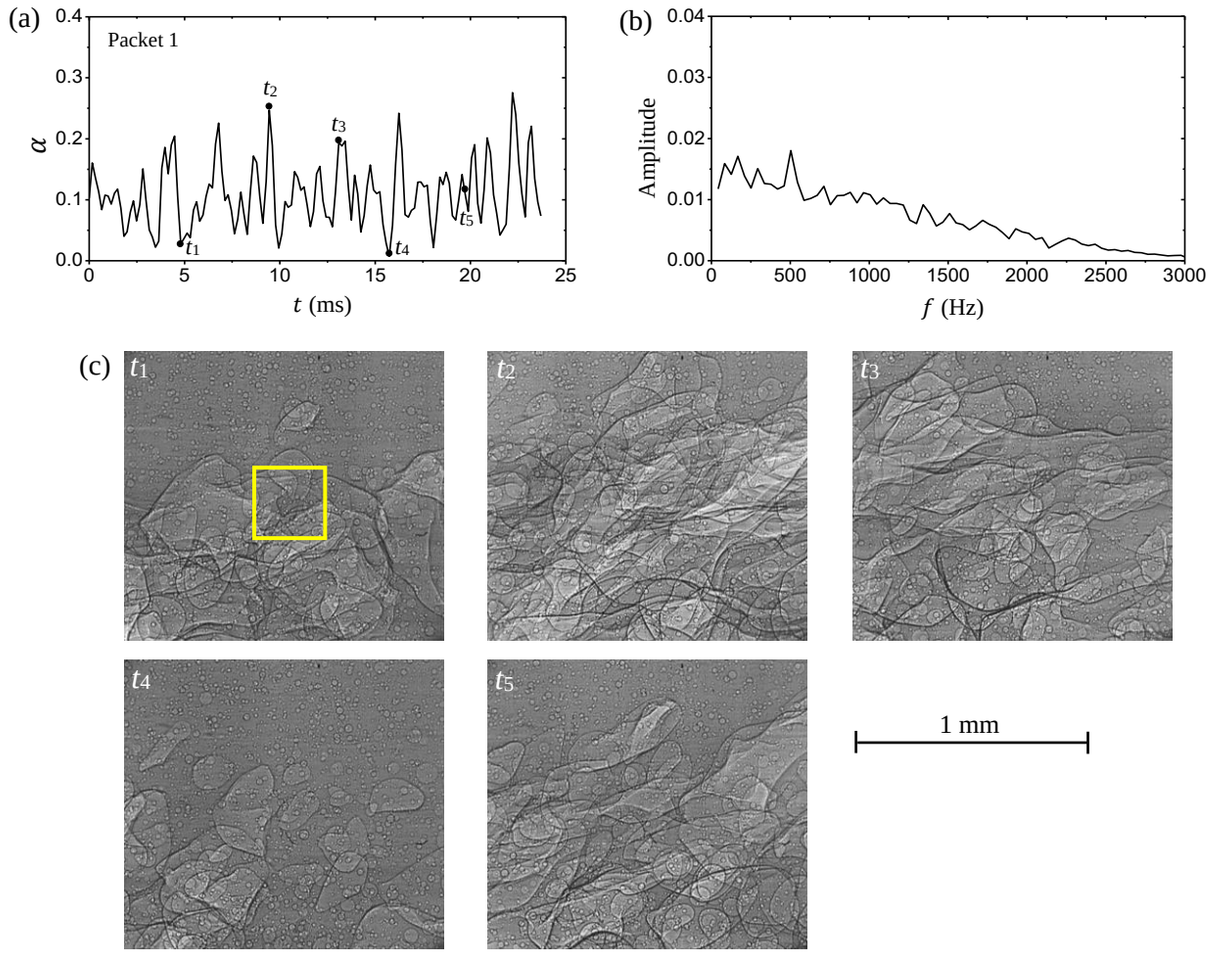


**FIG. 17.** Examination of void fraction in the X-ray scanning position 107 for $\sigma$ = 7.54, (a) time-varying void fraction in the third probe location indicated by the yellow frame in (c); (b) average of all the spectra of 13 packets; (c) X-ray images at five typical time instants.

### 4.5. *Summary of two-phase flow structures observed inside the sheet cavity*

Based on the above analysis, the sheet cavity in the present flow conditions is essentially divided into 6 parts as shown in Fig. 18(a). The complete flow field is reconstructed by assembling 22 instantaneous X-ray images in the corresponding scanning positions. In each position one X-ray image is selected manually to represent local flow characteristics. In order to display the internal structures clearly, this giant reconstructed picture (7887×1326 pixels) is split into 3 sections that are zoomed and presented in Fig. 18(b-d) with the scanning position numbers.

The upstream part (1) of the sheet cavity is characterized by an attached vapor pocket that is sustained due to intense vaporization at its upper interface with the liquid flow. Under the influence of the re-entrant flow, the vapor pocket grows and retracts quasi-periodically in a limited range of $x$ = 0-4 mm at a frequency of 167±21 Hz.

The reverse region (5) can be divided into 3 sub-regions (5a), (5b) and (5c), namely the upstream part, the main part, and the downstream part. The upstream part (5a) of the re-entrant flow ends on average at x = 1.5 mm where corresponds to the location of maximum standard deviation of void fraction. When the attached vapor pocket interacts with the front of the re-entrant flow, it detaches from the wall and transitions into a low-void-ratio bubbly mixture. The upstream part (5a) is likely to reach the vicinity of the throat, but it does not cut the sheet cavity completely into two parts forming large vapor cloud shedding. The main part (5b) of the re-entrant flow is characterized by the continuous presence of reverse flow. In

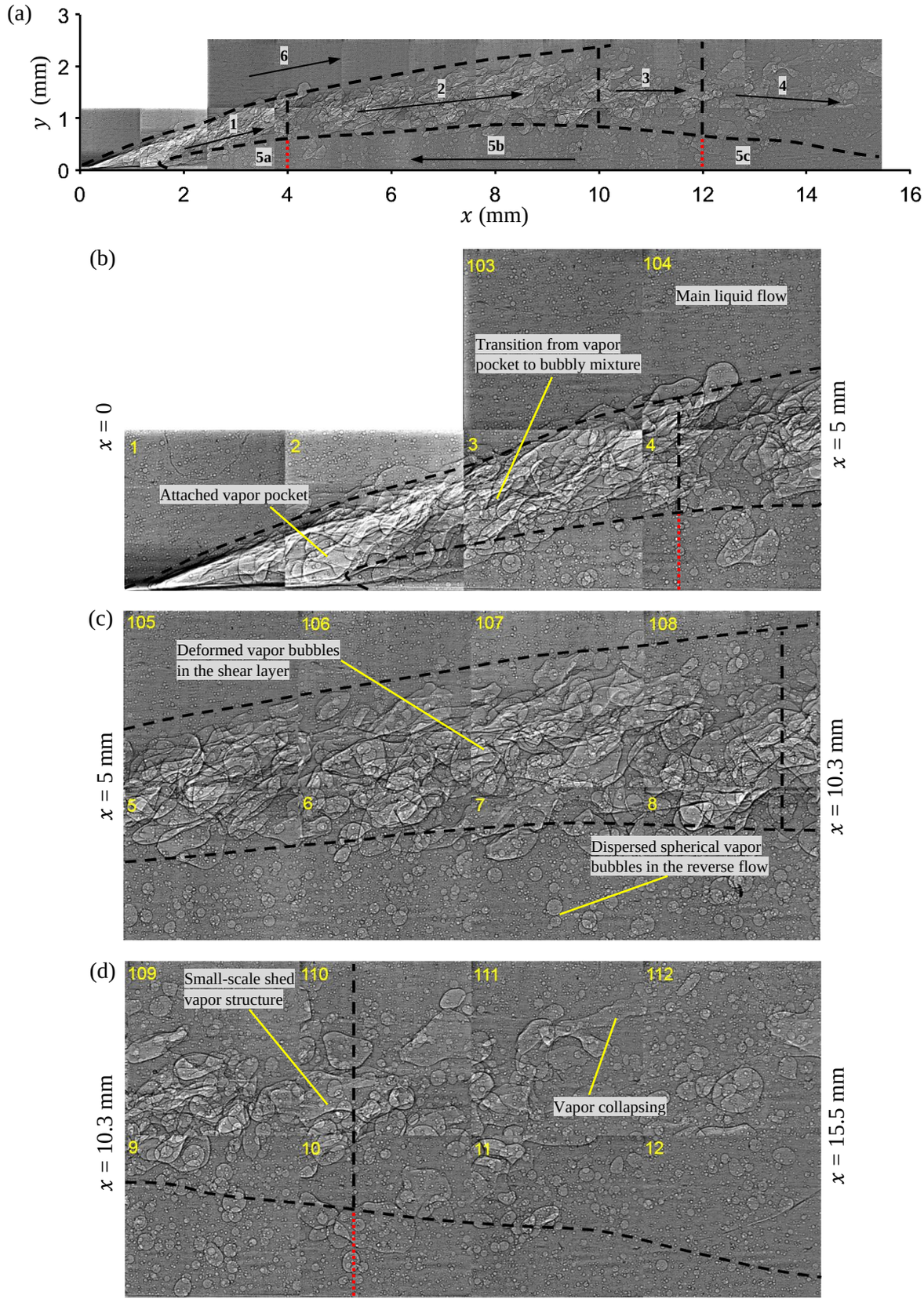


**FIG. 18**. Two-phase flow structures inside the sheet cavity for $\sigma$ = 7.54, (a) a reconstructed image from 22 scanning positions showing the internal structures of sheet cavity. The arrows indicate the mean flow directions in each sub-region; the image is split into 3 sections that are enlarged and shown in (b-d).

this region, the thickness of the re-entrant flow remains quite constant, and the mean velocity is fairly uniform spanning the whole thickness. The magnitude of the mean reverse flow velocity also remains quite constant along the streamwise direction at its maximum value of approximately 0.6 m/s (7% $u_{\mathrm{ref}}$). The downstream part (5c) is a region where the re-entrant flow originates from. The whole re-entrant flow can be considered as a liquid film moving upstream with dispersed cavitation bubbles since the mean void fraction in this region is close to 0. The sparse bubbles carried by the reverse flow travel upstream and tend to be of spherical shape as the velocity gradient is relatively small.

A strong velocity shear layer (2) exists steadily between the re-entrant flow (5) and the main flow (6) outside the cavity. In this region, the mean void fraction decreases along the flow direction at a very slow rate, and the standard deviation of void fraction is almost invariable. No characteristic frequency is detected regarding the time-varying void fraction. The low-void-fraction bubbly mixtures originated from the upstream vapor pocket are convected in the shear layer (2) without significant morphological and phase changes as their collapse might be limited by low pressure in the cores of vortical structures. The coherent bubbles are deformed into a large variety of shapes and sizes as a consequence of high velocity gradient in the shear layer.

In the cavity closure region (3), small-scale vapor structures are shed continuously from the main cavity under the entrainment of the main flow and/or the action of horseshoe vortices. The mean sheet cavity is also terminated in this region (the mean cavity length is 11.5 mm in the present flow conditions). The part (4) is the cavity wake region where the shedding vapor structures collapse into a large number of small bubbles. The mean void fraction in the wake is basically below 5%.

### 4.6. *Turbulent velocity fluctuations inside the sheet cavity*

The acquisition of time-resolved velocity fields inside the sheet cavity allows to compute the distribution of velocity fluctuations. Fig. 19(a-c) show the distributions of streamwise velocity fluctuations $\overline{u'u'}/u_{\mathrm{ref}}^2$, transversal velocity fluctuations $\overline{v'v'}/u_{\mathrm{ref}}^2$ and shear stress $|\overline{u'v'}|/u_{\mathrm{ref}}^2$, respectively, with the evolution of velocity gradient $\partial\overline{u}/\partial y$ along the flow direction shown in (d). The velocity fluctuations in longitudinal and transversal directions have the similar distributions and both of their domains of high-velocity fluctuations correspond pretty well to the shear area (indicated by the two dashed lines). The turbulence level in the reverse flow region is quite low due to the statistically steady state of the re-entrant flow in the studied sheet cavitation. With the growth of shear layer thickness, the velocity gradient decreases along the streamwise direction. The longitudinal and transversal velocity fluctuations are observed to decrease gradually along the flow direction, which is consistent with the trend of velocity gradient. In the cavity wake ($x$ >12 mm) where the shed vapor structures collapse, the longitudinal and transversal fluctuations do not increase compared with the upstream region. One possible explanation for this is that the decrease of fluctuations caused by the velocity gradient reduction is dominant, compared with the effect of vapor collapse, since the collapse is relatively mild in sheet cavitation.

With regard to the distribution of shear stress $|\overline{u'v'}|/u_{\mathrm{ref}}^2$, it appears to be weakly correlated with the velocity gradient. The most intense area of shear stress is located in the range of $x$ = 12-16 mm where is exactly the region vapor collapse occurs. It implies that the collapse of vapor phase has increased the coupling substantially between the streamwise and cross-stream velocity fluctuations. The second intense area of shear stress is located in a narrow strip area ($x$ = 0-4 mm) where is actually the interface of the upstream vapor pocket with the liquid main flow. This interface is also the position the sheet cavity is fed from the liquid through intense vaporization. Therefore, we conjecture that the phase change of vaporization also contributes to the coupling between the streamwise and cross-stream velocity fluctuations. In the range

of $x$ = 4-10 mm, the vapor bubbles are convected without significant phase change and accordingly the correlation between the streamwise and cross-stream velocity fluctuations reaches the lowest level.

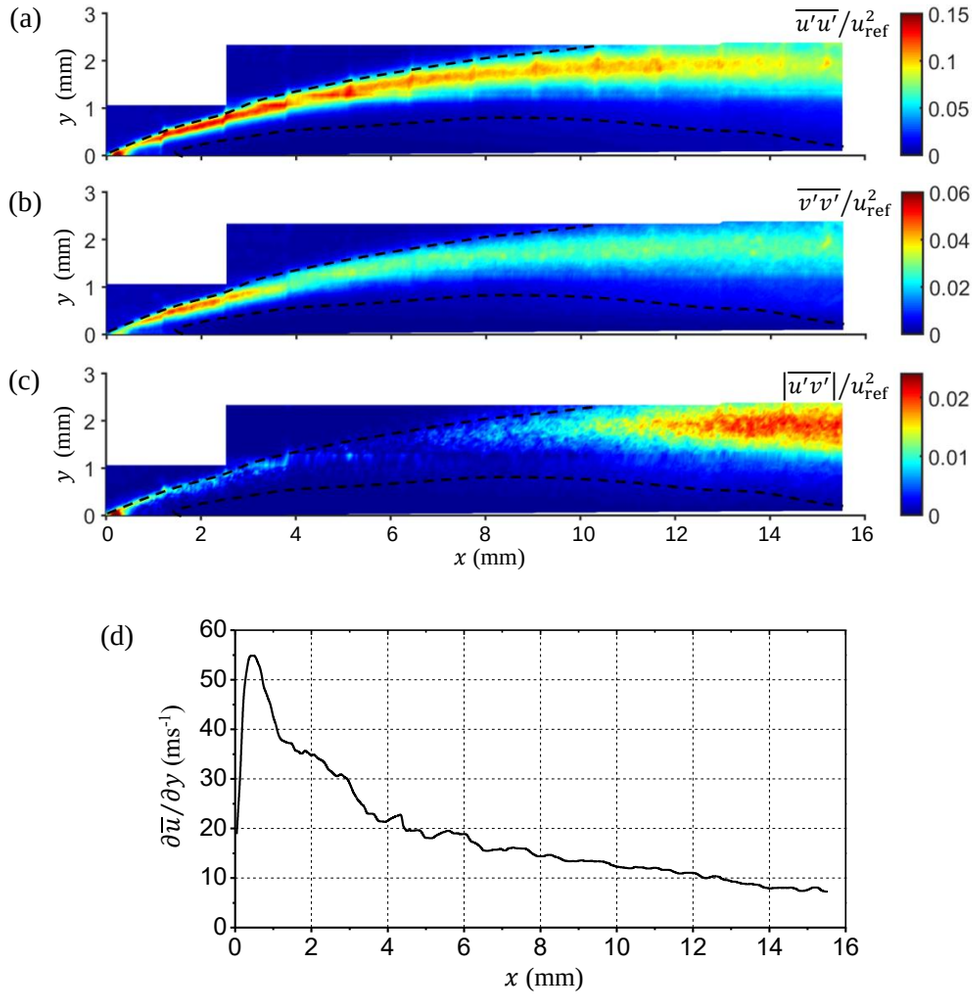


**FIG. 19.** Turbulence statistics for $\sigma$ = 7.54. (a) Distribution of streamwise velocity fluctuations $\overline{u'u'}/u_{ref}^2$; (b) distribution of transversal velocity fluctuations $\overline{v'v'}/u_{ref}^2$; (c) distribution of shear stress $|\overline{u'v'}|/u_{ref}^2$; (d) evolution of velocity gradient $\partial\bar{u}/\partial y$ along the flow direction. The two dashed lines indicate the shear area between the re-entrant flow and the main flow.

## 5. Discussion and conclusions

The cavitating flow in the present Venturi geometry with a small contraction ratio is characterized by a quasi-stable sheet cavitation, which was at first studied through conventional high speed photography. The main part of the sheet cavity was observed to attach to the solid surface steadily while small vapor structures were rolled up and shed continuously from the closure region in an irregular manner. These global behaviors of sheet cavitation observed from high speed images are consistent with the previous research about this cavitation pattern. So far the mainstream explanation to the quasi-stable sheet cavitation is that no re-entrant jet exists underneath the cavity or the re-entrant jet only exists near the cavity closure region, thereby producing a relatively stable fore part with a turbulent frothy closure. However, this conjecture was challenged by the current X-ray imaging measurements.

An accurate description of cavitation physics strongly relies on the visualization of two-phase morphology and the measurements of characteristic quantities (e.g. velocity and void fraction) inside cavitating areas. The use of conventional optical techniques has been unsuccessful to provide these information due to the opacity of the liquid/vapor mixture. Motivated by solving this problem, an ultra-fast synchrotron X-ray imaging technique was developed in consideration of X-rays high penetrability and weak interaction with matter. Small silver-coated hollow particles (~17 μm) were injected into the cavitating flow as the liquid phase tracers for PIV. Thanks to the high-flux coherent X-ray beam provided by the APS synchrotron facility and the purposed-made test section with extremely thin Plexiglas side walls, we obtained unprecedented images of fast-moving cavitation structures and tracer particles under the combined effects of X-ray phase contrast and absorption contrast. The further post-processing to the raw X-ray images enabled the simultaneous acquisition of time-resolved velocity and void fraction fields in the cavitating flow for the first time.

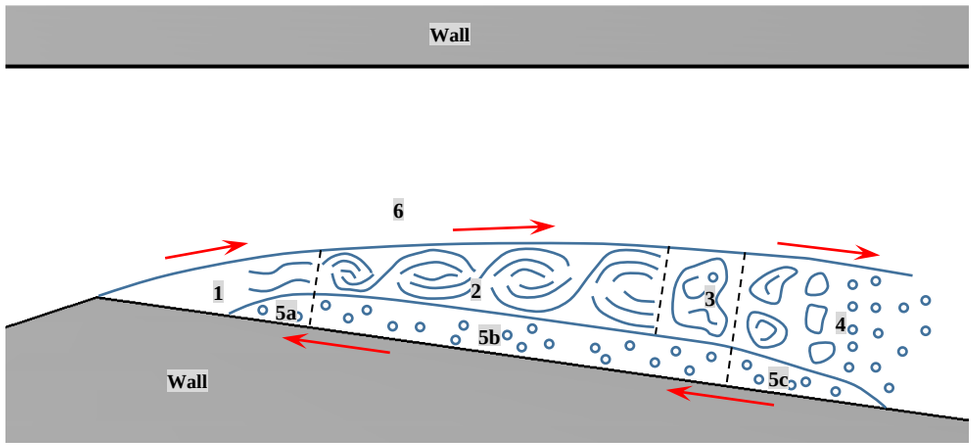


**FIG. 20.** Schematic of two-phase flow structures of sheet cavitation.

Based on the data from X-ray measurements, the complex two-phase flow morphological features and dynamics inside the quasi-stable sheet cavity were revealed in such detail for the first time. As shown in Fig. 20, the open sheet cavity in the present flow conditions is essentially divided into 6 characteristic parts. The attached vapor pocket is sustained in the very upstream part (1) of the sheet cavity due to intense vaporization and it oscillates quasi-periodically under the influence of the re-entrant flow (5a). The main part (5b) of the re-entrant flow exists persistently near the wall with a relatively constant thickness and velocity. When the attached vapor pocket interacts with the front of the re-entrant flow, it detaches from the wall and transforms into a low-void-ratio bubbly mixture. The entire re-entrant flow can be regarded as a liquid film carrying a number of spherical vapor bubbles. A strong velocity shear layer (2) exists steadily between the re-entrant flow (5) and the main flow (6) outside the cavity. In this region, the bubbly mixtures originated from the upstream vapor pocket are convected downstream without significant morphological and phase changes as their collapses might be limited by low pressure in the cores of coherent vortical structures. In the closure part (3), small-scale vapor structures are shed continuously from the main cavity. The part (4) is the cavity wake region where the shed vapor structures collapse into a large number of small bubbles. In general, the studied stable sheet cavitation is characterized by a low-speed re-entrant flow existing continuously underneath the cavity. Although it can almost penetrate the entire cavity, it does not pinch off the cavity forming the shedding of large vapor clouds. This might be attributed to the re-entrant flow having insufficient momentum in contrast to that the measured re-entrant jet velocity in periodic cloud cavitation is generally of the same order of magnitude as the free-stream velocity.

The turbulent velocity fluctuations inside the sheet cavity were also investigated. The domains of high-velocity fluctuations in the streamwise and cross-stream direction were found to correspond to the shear area. Both of them decrease gradually along the flow direction, which is consistent with the trend of velocity gradient. The turbulence level in the reverse flow region is as low as in the main flow demonstrating the relatively steady status of the re-entrant flow. Unlike the streamwise and cross-stream fluctuations, the shear stress appears to be weakly correlated with the velocity gradient. The collapse of vapor phase was found to be the main cause of the largest shear stress in the cavity wake. The phase change of vaporization at the upstream interface was also found to increase the coupling between the streamwise and cross-stream velocity fluctuations. The lowest shear stress was identified in the shear layer where vapor bubbles are convected without significant phase change.

**Acknowledgements**

This work was supported by the scholarship from China Scholarship Council (CSC) under the Grant CSC NO. 201608320260. Use of the Advanced Photon Source at the Argonne National Laboratory was supported by the US Department of Energy, Office of Science, and Office of Basic Energy Sciences.

**Data availability**

The data that support the findings of this study are available from the corresponding author upon reasonable request.

## Appendix A. X-ray imaging mechanisms

The X-ray imaging in this work is based on two different mechanisms: absorption contrast and phase contrast. The arrangement of in-line X-ray imaging system is depicted in Fig. 21(a). The radiograph is projected onto the $x$-$y$ plane perpendicular to the optic axis $z$. $R_1$ and $R_2$ are the source to object distance and object to detector distance, respectively. Considering a sample of a spherical vapor bubble in water, the working principle of absorption-based X-ray imaging is illustrated in Fig. 21(b). In this method, the detector is placed at the object exit surface $z = 0$. The contrast in the resulting image comes from the difference in the attenuation of X-ray energy since vapor has a smaller absorption coefficient than water. In phase-contrast X-ray imaging via free-space propagation as shown in Fig. 21(c), the sharp contrast at the periphery of the recorded image results from Fresnel diffraction at a certain distance from the sample. To make phase effects detectable an appropriate propagation distance $R_2$ between the object and the detector is required and the X-ray beam must be (at least partially) spatially coherent. Note that absorption contrast still contributes to the intensity image acquired by the propagation-based phase contrast technique.

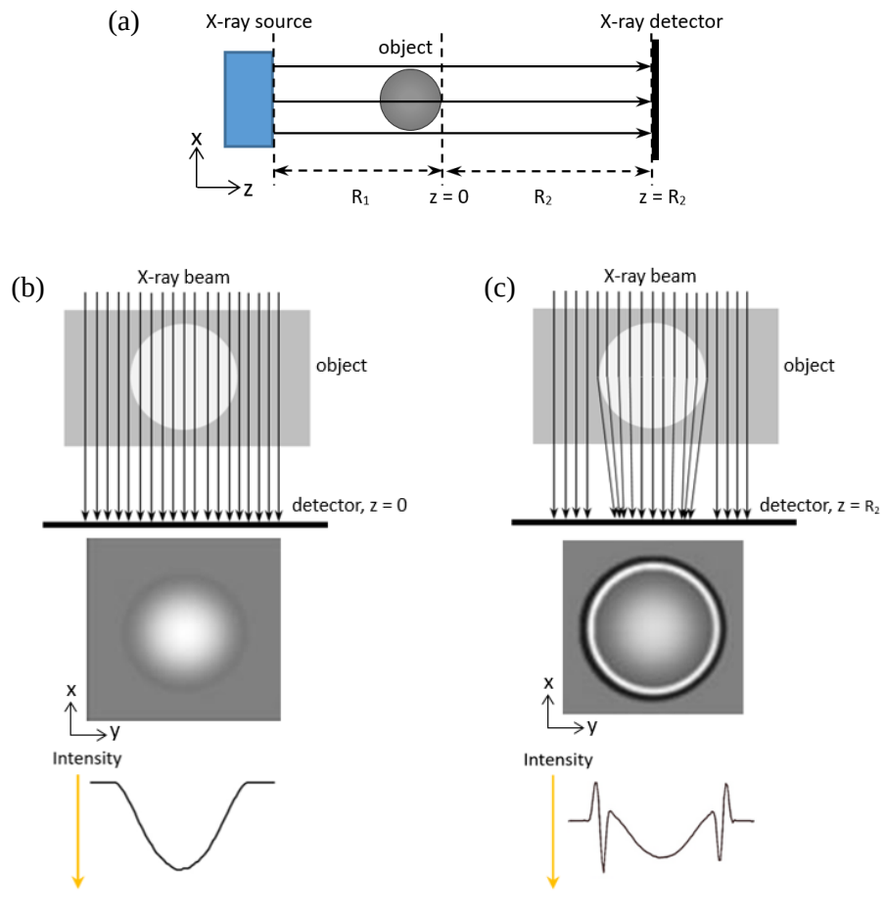


**FIG. 21.** (a) Schematic of in-line X-ray imaging system. $R_1$ and $R_2$ are the source to object distance and object to detector distance, respectively. (b) Simple model for absorption contrast of X-ray imaging. (c) Simple model for free-space propagation-based phase contrast of X-ray imaging.

## Appendix B. Procedures of wavelet-decomposition-based image processing method

A raw X-ray image of cavitation shown in Fig. 4(a) was taken here as an example to illustrate the procedures of extracting the tracer particles from the raw image. As mentioned before, the imaging is based on a combination of absorption contrast and phase contrast. The identification of particles also relies on the traits of these two mechanisms.

A two-dimensional signal (an image for instance) can be decomposed into approximation components and detail components at different levels by the discrete wavelet transform. As shown in Fig. 22(a), it is accomplished by convolving the original signal s with a low-pass filter and a high-pass filter simultaneously resulting in an approximation component $a_1$ and a detail component $d_1$ respectively. Note that the two filters are quadrature mirror filters associated with the selected wavelet function. This decomposition is repeated until the desired level to further increase the scale resolution using the same scheme, replacing the original signal s by $a_1$ and producing $a_2$ and $d_2$, and so on. The level N corresponds to the scale of $2^N$ in the wavelet function.

Fig. 22(c) presents the decomposition results by performing a 4-level discrete wavelet transform with the db5 wavelet function in the MATLAB software. As shown in Fig. 22(b), the part confined by the red frame in the raw image is zoomed up for clarity. The reason of choosing db5 wavelet is that its shape matches quit well with sharp fringe intensity variations due to the phase contrast mechanism. Observing the approximation component $a_4$, we can know that there are no useful signals included in it (all particles are filtered out), so further decomposition is not necessary. The level of wavelet

decomposition is therefore determined as 4. Observing the detail components from $d_1$ to $d_4$, it is found that the different scales of signals are separately stored in detail components at different levels: the background high-frequency noise is primarily contained in $d_1$; most edge information of particles and vapor bubbles is contained in $d_2$; the interiors of particles are mainly contained in $d_3$ while only a small proportion of particles with largest scales are contained in $d_4$.

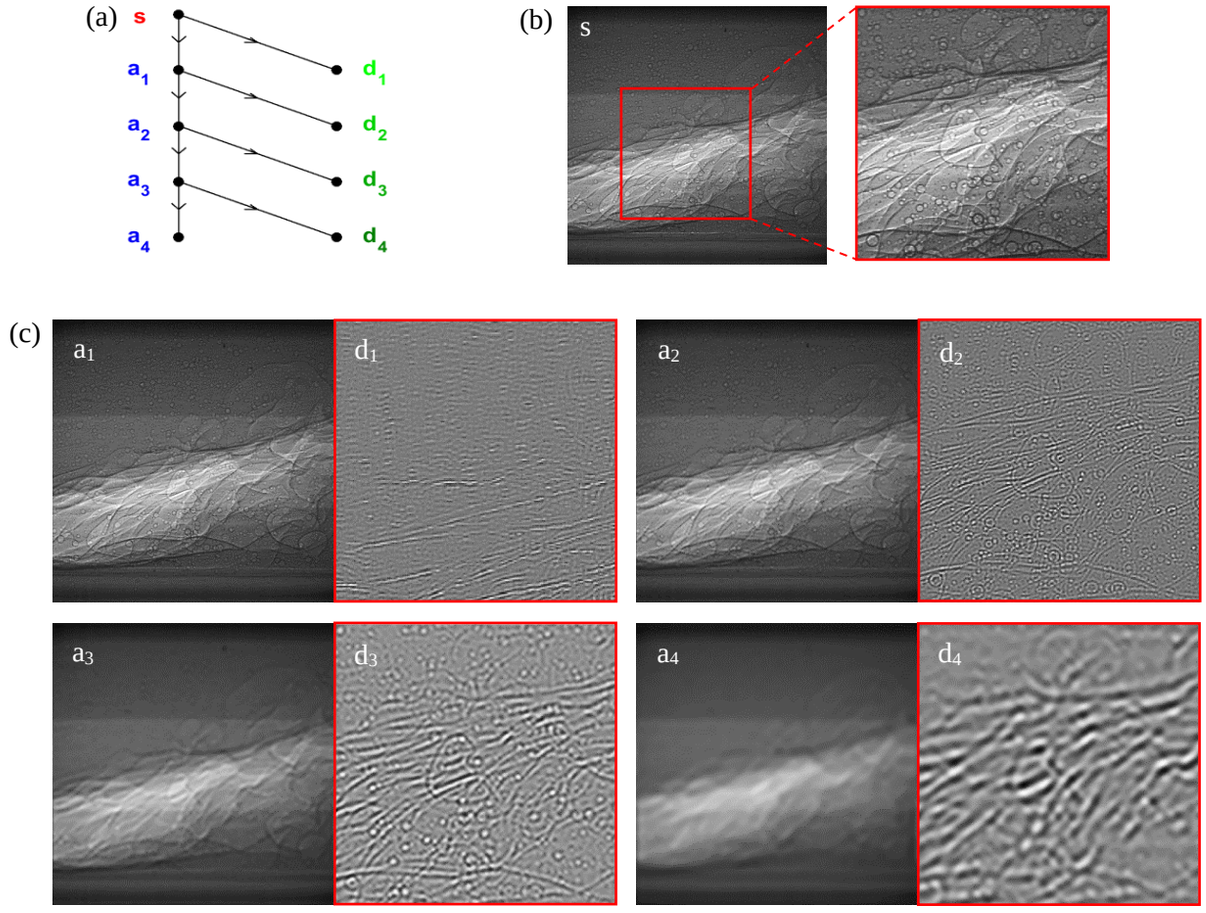


**FIG. 22.** Discrete wavelet transform. (a) A binary tree of 4-level discrete wavelet transform; (b) raw X-ray image and the zoomed-up part; (c) wavelet decomposition results corresponding to the binary tree of 4-level discrete wavelet transform.

The phase contrast enhances the visibility of the edge. Therefore the first identification of particles is based on the detection of the edges with sharp contrast (i.e. large intensity gradient). In this case, we wish to highlight the boundaries of the particles rather than their interiors. This can be realized by choosing appropriate threshold values for each level from 1 to 4. In general, a relatively large threshold value is set for level 2 with small threshold values for the other levels since most edge information is contained in the detail component $d_2$. In practice these threshold values were determined empirically in the Matlab graphical user interface tool –wavemenu where it is convenient to adjust threshold values to obtain a subjectively optimal result. Fig. 23(a) and (b) show the decomposition results using the threshold values determined from wavemenu. It can be seen that the boundaries of the particles and the vapor bubbles are separated out while leaving the particle interiors and the large-area vapor structures in the approximation component. In addition, the non-uniformities of image intensities caused by the beam's secondary pulse are solved, which would make the edge detection more effective.

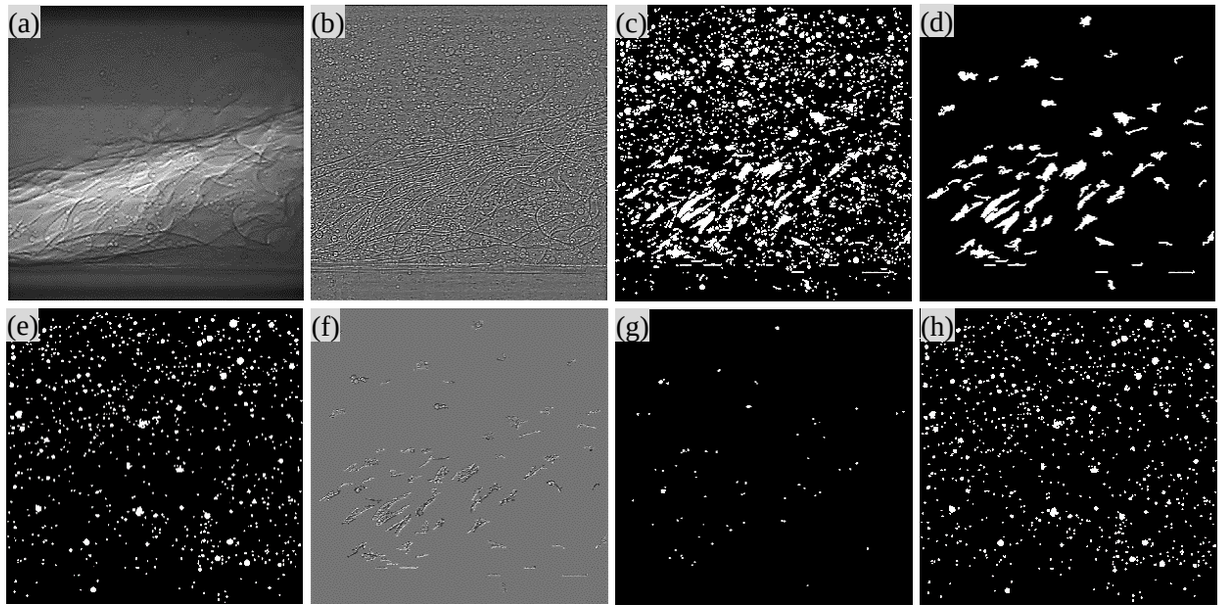


**FIG. 23.** Particle detection based on the phase contrast imaging mechanism, (a) reconstructed approximation component; (b) reconstructed detail component; (c) preliminary particle detection by Canny edge detector; (d) removed objects by prescribed criteria; (e) remaining particles; (f) removed region shown in grey level mode; (g) hidden particles in the removed regions; (h) final result of the first identification of particles.

The Canny edge detector (Canny 1986) based on image intensity gradients was then used given its ability to derive clean, thin edges that are well connected to nearby edges. In order to facilitate the following morphological operations, the enclosed areas by the detected edges are filled and presented as a binary image where the pixels with value 1 represent the locations occupied by particles. The remaining thin edges were removed via the morphological opening operation. Fig. 23(c) shows the result of the preliminary detection, which is not satisfactory due to the presence of vapor bubble edges. Criteria based on the size of the tracer particles and their shapes were applied to remove these spurious objects caused by vapor bubble edges: (1) the largest diameter of an object must not exceed 20 pixels (40 μm); (2) the eccentricity of an object must be less than 0.4 to ensure its roundness. The removed objects and the remaining particles are shown in Fig. 23(d) and (e), respectively. In fact, there are some particles hiding in the removed region [Fig. 23(f)], so the Canny edge detector and the criteria with slightly more strict thresholds were reapplied on the removed region to identify the hidden particles as shown in Fig. 23(g). The final result of the first identification of particles is shown in Fig. 23(h) and the number of objects recognized is 870.

On the other hand, we can take advantage of absorption contrast to identify particles since the hollow glass spheres reduce the X-ray attenuation. In this second identification, we wish to highlight the interiors of the particles rather than their edges. Fig. 24(a) and (b) show the decomposition results using a relatively large threshold value at level 3 as the interiors of particles are mainly contained in the detail component $d_3$. Fig. 24(c) presents the background suppression with a constant threshold value given that the background is almost homogeneous. This processing increases the contrast of particle interiors. Then the same procedures as the first identification were implemented to obtain the binary image of particles identified based on local attenuation difference as shown in Fig. 24(d) and (e). The number of objects in the second identification is 1060.

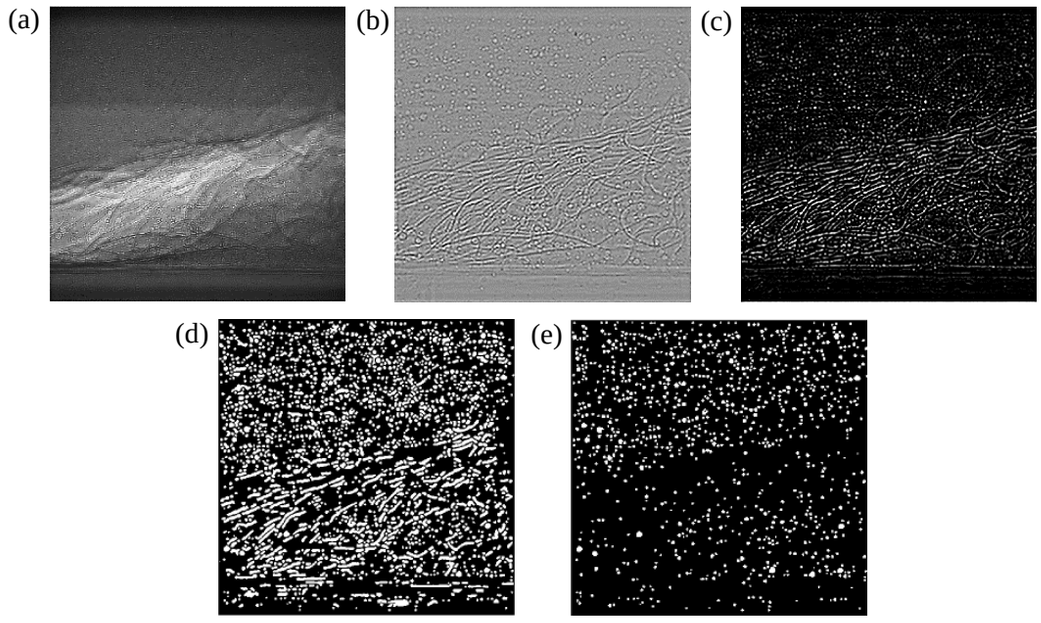


**FIG. 24.** Particle detection based on the absorption contrast imaging mechanism, (a) reconstructed approximation component; (b) reconstructed detail component; (c) background suppression; (d) binary image of identified particles with the presence of vapor structures; (e) final result of the second identification of particles.

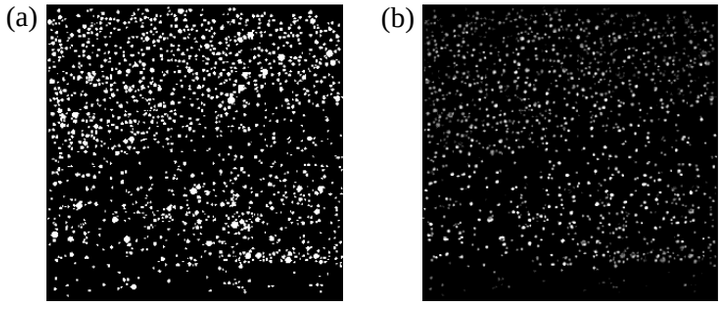


**FIG. 25.** (a) Combination of particles identified by the two methods; (b) particle gray level restoration.

Fig. 25(a) displays a combination of particles identified by the above two methods corresponding to the two imaging mechanisms. The total number of objects recognized is 1230. This number is important for determining the interrogation window size of PIV evaluation. All tracer particles are finally restored according to their detected locations. Fig. 25(b) illustrates the final image of particles which is used for the measurements of liquid phase velocities. It should be noted that the gray levels of particles were restored from the image shown in Fig. 25(c) instead of the raw X-ray image because the non-uniform exposure to X-ray beam would affect the PIV calculation, given that the cross-correlation peak is dominated by brighter particle images and the bright background might remain in the particle image due to the imperfect detection of particle locations.

## Appendix C. Improvement of void fraction measurement accuracy

Theoretically, every reference image of air or water in a sequence has the same intensity at the corresponding pixels if the synchronization scheme [Fig. 2(b)] is achieved perfectly. Then any reference image of air or water can be used to calibrate void fraction. However, when we observe a sequence of air reference images, it is found that the global intensity

and the width of the middle bright band vary with images. This suggests the ideal synchronization scheme is difficult to be achieved. In fact, the fast shutter, the camera and the X-ray pulses are synchronized in three different ways, which are responsible for the image-to-image difference. Fig. 26 illustrates the three synchronization schemes and their corresponding image pairs. The image row-averaged intensity is plotted for a quantitative comparison between the first frame (Image 1) and the second frame (Image 2) in the same pair. The maximum opening of the fast shutter is slightly shifted to the left relative to the middle secondary pulse 3 in all three schemes because it is observed that the first image of each pair has a relatively wide bright band compared to the second one. The camera frame transfer determines the secondary pulse 3 to illuminate Image 1 (scheme c) or Image 2 (scheme a) or neither (scheme b).

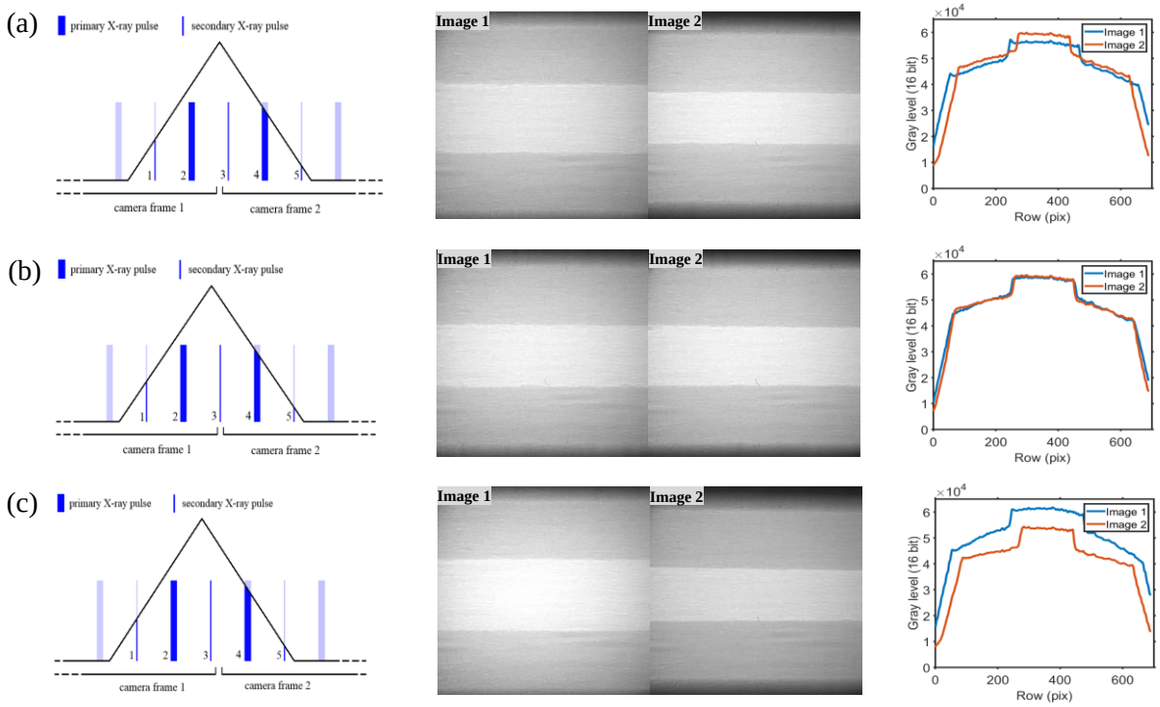


**FIG. 26.** Three synchronization schemes, (a) Image 1 exposed to one primary pulse and one secondary pulse, Image 2 exposed to one primary pulse and two secondary pulses; (b) both Image 1 and Image 2 exposed to one primary pulse and one secondary pulse; (c) Image 1 exposed to one primary pulse and two secondary pulses, Image 2 exposed to one primary pulse and one secondary pulse.

Due to the application of the slow shutter, only a packet of 144 pairs of images was recorded per opening of the slow shutter (13 packets in total). Fig. 27(a) illustrates the global intensity variation of air reference images in a packet of 144 image pairs. The green solid line denotes the mean intensity of the first image of each pair. The blue solid line denotes the mean intensity of the second image of each pair. The red dashed line signifies the average intensity of all images in the packet. It can be seen that the global intensity of the first image is different from the second image in the same pair and both intensity variations diverge with the image pairs in an oscillating way, which seemingly poses a convergence problem if the average image of a packet is used as the calibration image for gaseous phase. However, let us observe the variation of the average intensity of the two images belonging to the same pair shown in Fig. 27(b), it is noted that the quasi-periodic oscillation is steady in a statistical sense, relative to the average intensity of the packet. In addition, the other 12 packets of air reference images have the same tendency (not presented). The reference images of water were also examined and the

results in a packet are illustrated in Fig. 28. Although the image-to-image variation pattern is different, the variation of the pair average intensity is still consistent with the air reference images. Therefore, the calibration image of air (or water) for calculating vapor volume fraction can be obtained through averaging all the images in a packet.

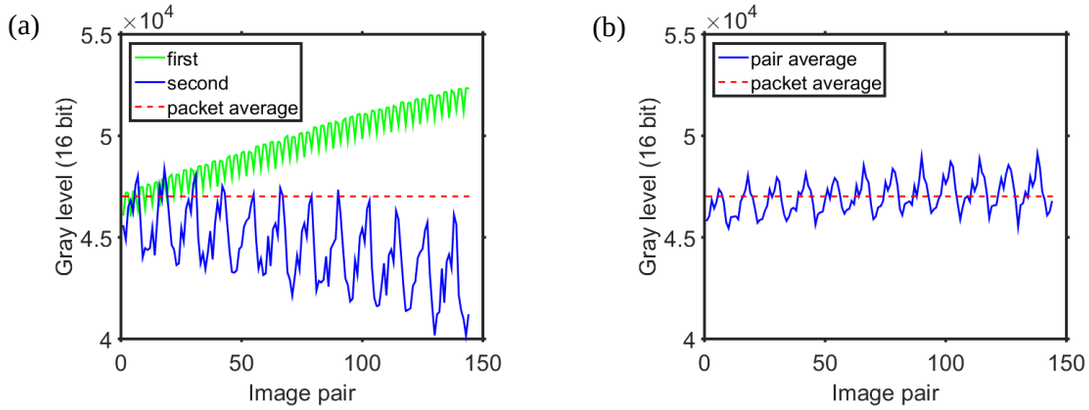


**FIG. 27.** Variation of global intensity of air reference images in a packet of 144 image pairs. (a) Intensity variations of the first image and the second image; (b) variation of the average intensity of the two images belonging to the same pair.

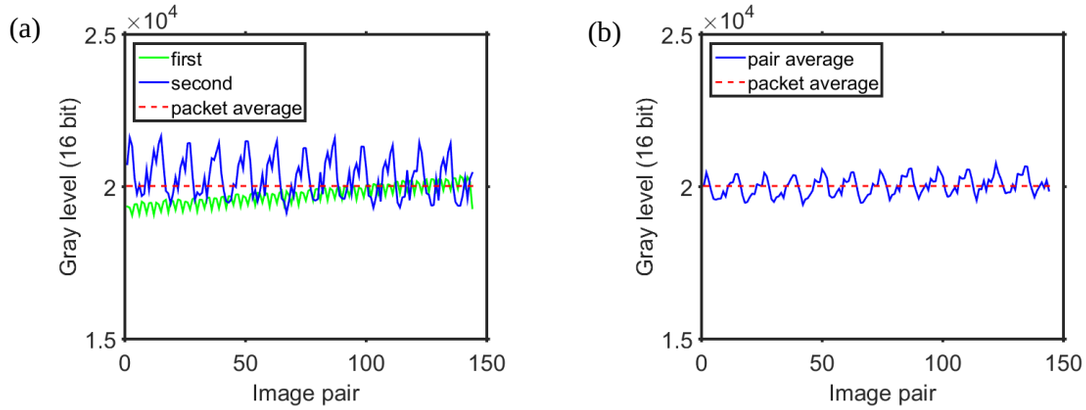


**FIG. 28.** Variation of global intensity of water reference images in a packet of 144 image pairs. (a) Intensity variations of the first image and the second image; (b) variation of the average intensity of the two images belonging to the same pair.

Taking into account the slight packet-to-packet difference, the calibration images for gaseous phase and liquid phase were finally obtained by averaging all the images in the thirteen packets of each phase. Accordingly, the local void ratio measurements in the cavitating flow cases were performed using the average of the two X-ray images belonging to the same pair as well. In this way, the non-uniform illumination caused by the synchronization problems will have a better correspondence with the reference images than the individual images and each velocity field will correspond to only one vapor volume fraction field.

Images of pure air and images of pure water can be used to estimate the accuracy of the aforementioned method for calculating vapor volume fraction since the errors are represented by the discrepancies between the calculated values and the theoretical values (100% for the vapor phase, 0% for the liquid phase). Fig. 29 indicates the mean vapor volume fraction errors estimated from 1872 air image pairs. The big errors (exceeding ±20%) are found at two ends, which is attributed to the insufficient exposure to the X-ray beam. Consequently, for a reliable result only the domain ranging from the 90$^{th}$ row to the 630$^{th}$ row (limited by the red dashed lines) is considered in the present paper. Thanks to averaging image pairs, the

mean error within the middle band is as small as outside the band attaining ±2%. However, the relatively large error (around ±4%) as circled is observed in the vicinity of the middle band edges. The explanation for this larger error is illustrated in Fig. 30 by comparison between the air calibration image and the averaged image of a typical pair of air images. As mentioned previously, the middle band of the first image (band 1) is wider than the second one (band 2). So in the pair averaged image there must be a narrow transition zone between the edges of these two bands with abrupt intensity change. However, due to averaging sufficient number of image pairs, the intensity variation within the transition zone of the air calibration image becomes relatively smooth since the middle band width varies with images. The different intensity transition from the air calibration image results in the relatively large errors.

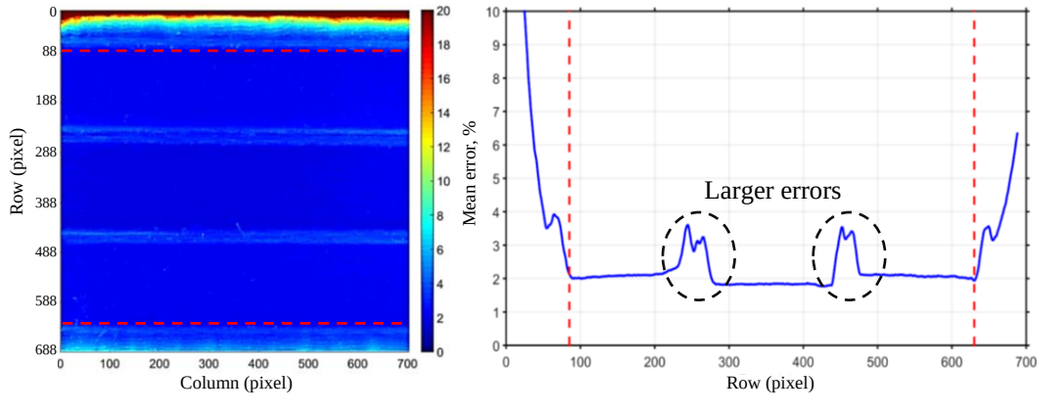


**FIG. 29.** Mean measurement error of vapor volume fraction estimated from pure air images.

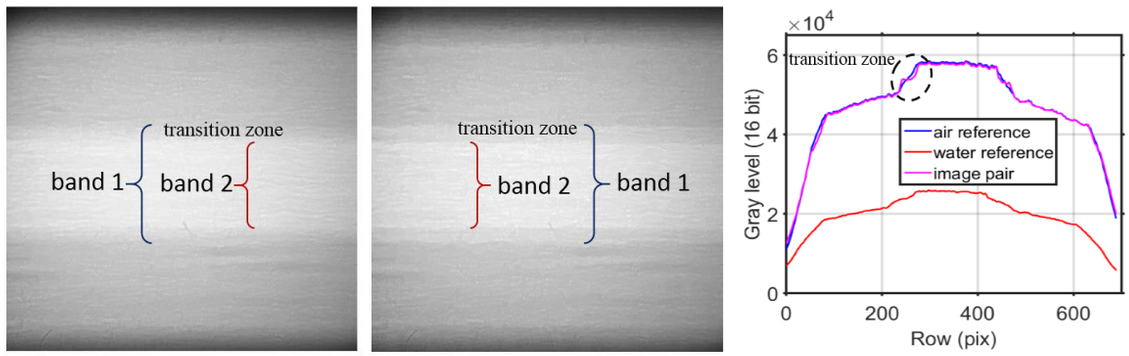


**FIG. 30.** Comparison between the air calibration image (left) and the averaged image of a typical air image pair (middle); their row-averaged intensity is plotted for a quantitative comparison (right).

In order to improve the accuracy within the transition zone, the band edges with sharp intensity change need to be smoothed to make them closer to the air calibration image. In an original X-ray image of air [Fig. 31(a)], wavelet decomposition was used to separate the band edges out [Fig. 31(b)] as the local discontinuities can be described better with wavelets. A 2D averaging filter was then applied on the detected band edges to smooth the intensity change as shown in Fig. 31(c). The processed detail component was combined with the approximation component of the wavelet transform to reconstruct the final result as shown in Fig. 31(d). All the other air images were treated by the above steps as well. Fig. 31(e) depicts the mean vapor volume fraction errors obtained from 1872 pairs of processed air images. It is obvious that thanks to the band edge smoothing the error within the transition zone (as circled) is reduced to the same order of magnitude (around ±2%) as the rest of the area.

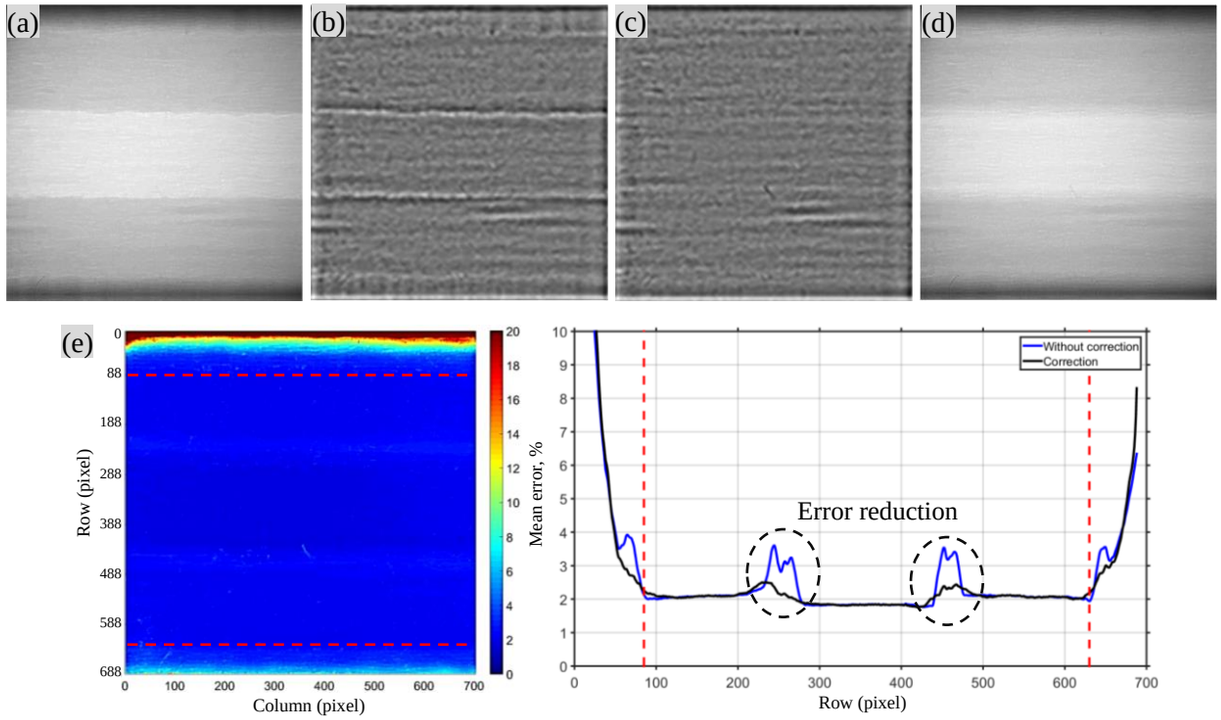


**FIG. 31.** Smooth the band edges to reduce vapor volume fraction errors within the transition zone. (a) An original X-ray image of air with sharp intensity change at the middle band edges; (b) separated detail component of band edges; (c) smoothing the intensity change at the band edges; (d) reconstructed air image with smooth intensity change at the band edges; (e) mean vapor volume fraction error estimated from processed air images, compared to the mean error estimated from air images without band edge intensity correction.

The fringe patterns due to phase contrast in the unprocessed X-ray image of cavitation [Fig. 32(a)], although important for visualizing particles and vapor bubbles, have a negative influence on the computation of void fraction. The diffracted dark edge lines coupled with bright ones at the phase interfaces result in local underestimation or overestimation of vapor volume fraction. In order to reduce the detrimental effect of phase contrast, the same wavelet transform as in the processing of particle identification was employed to decompose the original X-ray image but with different threshold values aiming to make the particle and vapor interfaces contained completely in the detail component. Fig. 32(b) presents the detail component where the two edges of the middle band are also included. A low pass averaging filter was applied on the image of detail component, after which the diffraction traits of black lines and white lines are neutralized, the high frequency particles are filtered out, and the middle band edges are smoothed. The processed detail component [Fig. 32(c)] was subsequently added to the image of approximation component reconstructing the image of vapor structures without particles nor vapor bubble interfaces as shown in Fig. 32(d). The other X-ray image in the same pair was treated using the same steps as well [Fig. 32(e)]. The average image of the pair is indicated in Fig. 32(f): this is the one used for the calculation of the vapor volume fraction, rather than the individual one.

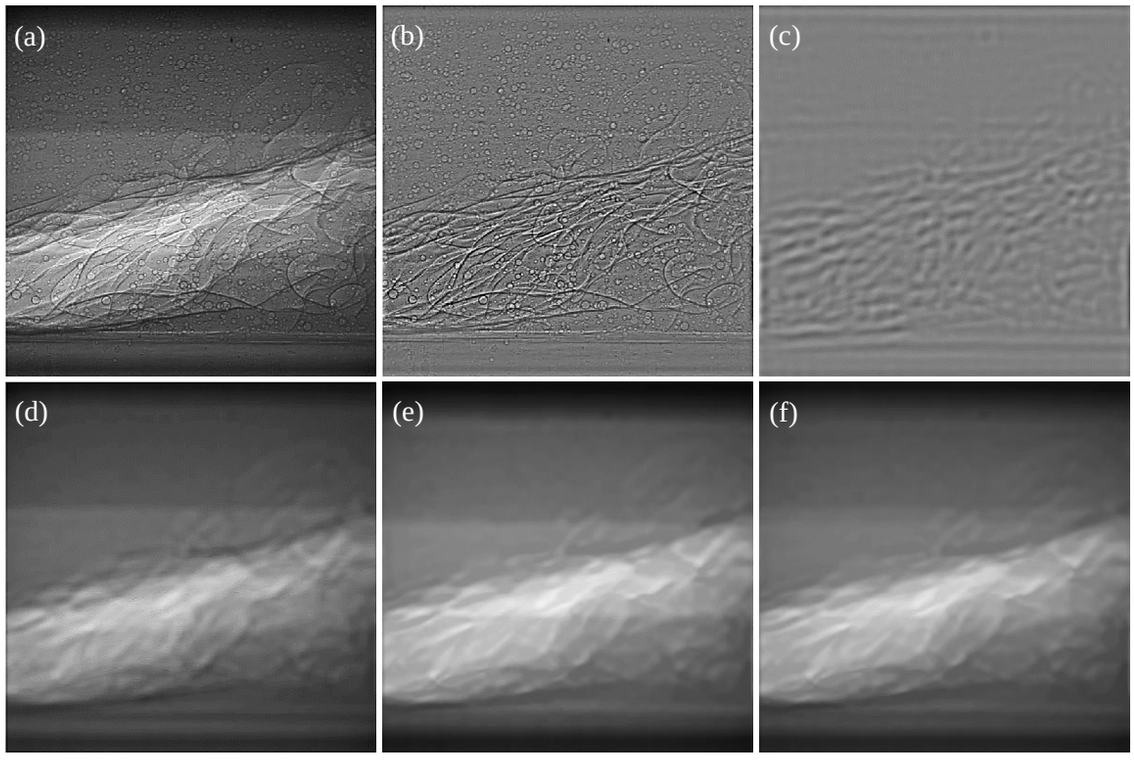


**FIG. 32.** Image processing for vapor volume fraction measurements, (a) unprocessed X-ray image of cavitation; (b) detail component of wavelet decomposition; (c) detail component processed by averaging filter; (d) first processed image of vapor structures without particles nor vapor bubble interfaces in a pair; (e) second processed image of vapor structures without particles nor vapor bubble interfaces in a pair; (f) pair averaged image for estimating vapor volume fraction.

## References

1. Aeschlimann, V., Barre, S., and Djeridi, H., "Velocity field analysis in an experimental cavitating mixing layer," Phys. Fluids 23(5), 055105 (2011a).
2. Aeschlimann, V., Barre, S., and Legoupil, S., "X-ray attenuation measurements in a cavitating mixing layer for instantaneous two-dimensional void ratio determination," Phys. Fluids, 23(5), 055101 (2011b).
3. Barre, S., Rolland, J., Boitel, G., Goncalves, E., and Patella, R. F., "Experiments and modeling of cavitating flows in venturi: attached sheet cavitation," Eur. J. Mech. B-Fluid 28(3), 444–464 (2009).
4. Bothell, J. K., Machicoane, N., Li, D., Morgan, T. B., and Heindel, T. J., "Comparison of X-ray and optical measurements in the near-field of an optically dense coaxial air-assisted atomizer," Int. J. Multiphase Flow, 125, 103219 (2020).
5. Budich, B., Schmidt, S. J., and Adams, N. A., "Numerical simulation and analysis of condensation shocks in cavitating flow," J. Fluid Mech. 838, 759-813 (2018).
6. Callenaere, M., Franc, J. P., Michel, J. M., and Riondet, M., "The cavitation instability induced by the development of a re-entrant jet," J. Fluid Mech. 444, 223-256 (2001).
7. Canny, J., "A computational approach to edge detection," IEEE Trans. (6), 679-698 (1986).

8. Coutier-Delgosha, O., Devillers, J. F., Pichon, T., Vabre, A., Woo, R., and Legoupil, S., "Internal structure and dynamics of sheet cavitation," Phys. Fluids 18(1), 017103 (2006).
9. Coutier-Delgosha, O., Stutz, B., Vabre, A., and Legoupil, S., "Analysis of cavitating flow structure by experimental and numerical investigations," J. Fluid Mech. 578, 171-222 (2007).
10. Coutier-Delgosha, O., Vabre, A., Hocevar, M., Delion, R., Dazin, A., Lazaro, D., and Lee, W. K., "Local measurements in cavitating flow by ultra-fast x-ray imaging," in *ASME 2009 Fluids Engineering Division Summer Meeting*, pp. 371-379, (2009).
11. Danlos, A., Ravelet, F., Coutier-Delgosha, O., and Bakir, F., "Cavitation regime detection through Proper Orthogonal Decomposition: Dynamics analysis of the sheet cavity on a grooved convergent–divergent nozzle," Int. J. Heat Fluid Fl. 47, 9–20 (2014).
12. Dular, M., Bachert, B., Stoffel, B., and Sirok, B., "Relationship between cavitation structures and cavitation damage," Wear 257, 1176–1184 (2004).
13. Foeth, E. J., Van Doorne, C. W. H., Van Terwisga, T., and Wieneke, B., "Time resolved PIV and flow visualization of 3D sheet cavitation," Exp. Fluids 40(4), 503-513 (2006).
14. Ganesh, H., Mäkiharju, S. A., and Ceccio, S. L., "Bubbly shock propagation as a mechanism for sheet-to-cloud transition of partial cavities," J. Fluid Mech. 802, 37-78 (2016).
15. Gembicky, M., Oss, D., Fuchs, R., and Coppens, P., "A fast mechanical shutter for submicrosecond time-resolved synchrotron experiments," J. Synchrotron Radiat. 12(5), 665-669 (2005).
16. Gopalan, S., and Katz, J., "Flow structure and modeling issues in the closure region of attached cavitation," Phys. Fluids 12(4), 895-911 (2000).
17. Heindel, T. J., "A review of X-ray flow visualization with applications to multiphase flows," J. Fluids Eng., 133(7), 074001 (2011).
18. Heindel, T. J., "X-ray imaging techniques to quantify spray characteristics in the near-field," Atomization and Sprays 28(11), 1029–1059 (2018).
19. Im, K. S., Fezzaa, K., Wang, Y. J., Liu, X., Wang, J., and Lai, M. C., "Particle tracking velocimetry using fast x-ray phase-contrast imaging," Appl. Phys. Lett. 90(9), 091919 (2007).
20. Iyer, C. O., and Ceccio, S. L., "The influence of developed cavitation on the flow of a turbulent shear layer," Phys. Fluids, 14(10), 3414-3431 (2002).
21. Karathanassis, I. K., Koukouvinis, P., Kontolatis, E., Lee, Z., Wang, J., Mitroglou, N., and Gavaises, M., "High-speed visualization of vortical cavitation using synchrotron radiation," J. Fluid Mech. 838, 148–164 (2018).
22. Kastengren, A., and Powell, C. F., "Synchrotron X-ray techniques for fluid dynamics," Exp. Fluids, 55, 1686 (2014).
23. Kawanami, Y., Kato, H., Yamaguchi, H., Tanimura, M., and Tagaya, Y., "Mechanism and control of cloud cavitation," J. Fluids Eng. 119(4), 788-794 (1997).
24. Khlifa, I., Vabre, A., Marko Hočevar, Fezzaa, K., Fuzier, S., Roussette, O., and Coutier-Delgosha, O., "Fast x-ray imaging of cavitating flows," Exp. Fluids 58(11), 157 (2017).
25. Knapp, R.T., "Recent investigations of the mechanics of cavitation and cavitation damage," Trans. ASME 77, 1045–1054 (1955).
26. Kravtsova, A. Y., Markovich, D. M., Pervunin, K. S., Timoshevskiy, M. V., and Hanjalić, K., "High-speed visualization and PIV measurements of cavitating flows around a semi-circular leading-edge flat plate and NACA0015 hydrofoil," Int. J. Multiphase Flow 60, 119-134 (2014).

27. Laberteaux, K. R., and Ceccio, S. L., "Partial cavity flows. Part 1. Cavities forming on models without spanwise variation," J. Fluid Mech. 431, 1-41 (2001).
28. Le, Q., Franc, J., and Michel, J., "Partial cavities: global behavior and mean pressure distribution," J. Fluids Eng. 115, 243–248 (1993).
29. Lee, S. J., and Kim, G. B., "X-ray particle image velocimetry for measuring quantitative flow information inside opaque objects," J. Appl. Phys. 94(5), 3620-3623 (2003).Leroux, J. B., Jacques André Astolfi, and Billard, J. Y., "An experimental study of unsteady partial cavitation," J. Fluids Eng. 126(1), 94-101 (2004).
30. Long, X., Zhang, J., Wang, J., Xu, M., and Ji, B., "Experimental investigation of the global cavitation dynamic behavior in a venturi tube with special emphasis on the cavity length variation," Int. J. Multiphase Flow 89, 290-298 (2016).
31. Pelz, P. F., Keil, T., and Groß, T. F., "The transition from sheet to cloud cavitation," J. Fluid Mech. 817, 439-454 (2017).
32. Pham, T. M., Larrarte, F., and Fruman, D. H., "Investigation of unsteady sheet cavitation and cloud cavitation mechanisms," J. Fluids Eng. 121(2), 289-296 (1999).
33. Poelma, C., "Measurement in opaque flows: a review of measurement techniques for dispersed multiphase flows," Acta. Mech. 231(6), 2089-2111 (2020).
34. Prothin, S., Billard, J.Y., and Djeridi, H., "Image processing using proper orthogonal and dynamic mode decompositions for the study of cavitation developing on a NACA0015 foil," Exp. Fluids 57(10), 157 (2016).
35. Schnerr, G. H., and Sauer, J., "Physical and numerical modeling of unsteady cavitation dynamics," in: *Fourth International Conference on Multiphase Flow*, New Orleans, USA, (2001).
36. Singhal, A. K., Athavale, M. M., and Li, H., "Mathematical basis and validation of the full cavitation model," J Fluid Eng. 124, 617−624 (2002).
37. Stutz, B., and Reboud, J. L., "Two-phase flow structure of sheet cavitation," Phys. Fluids 9(12), 3678-3686 (1997).
38. Stutz, B., and Reboud, J. L., "Measurements within unsteady cavitation," Exp. Fluids 29(6), 545-552 (2000).
39. Stutz, B., and Legoupil, S., "X-ray measurements within unsteady cavitation," Exp. Fluids 35(2), 130-138 (2003).
40. Wang, Y., Liu, X., Im, K. S., Lee, W. K., Wang, J., Fezzaa, K., and Winkelman, J. R., "Ultrafast X-ray study of dense-liquid-jet flow dynamics using structure-tracking velocimetry," Nat. Phys. 4(4), 305 (2008).
41. Wu, J., Ganesh, H., and Ceccio, S., "Multimodal partial cavity shedding on a two-dimensional hydrofoil and its relation to the presence of bubbly shocks," Exp. Fluids 60(4), 66 (2019).
42. Zhang, H., Zuo, Z., Mørch, K. A., and Liu, S., "Thermodynamic effects on Venturi cavitation characteristics," Phys. Fluids 31, 097107 (2019).

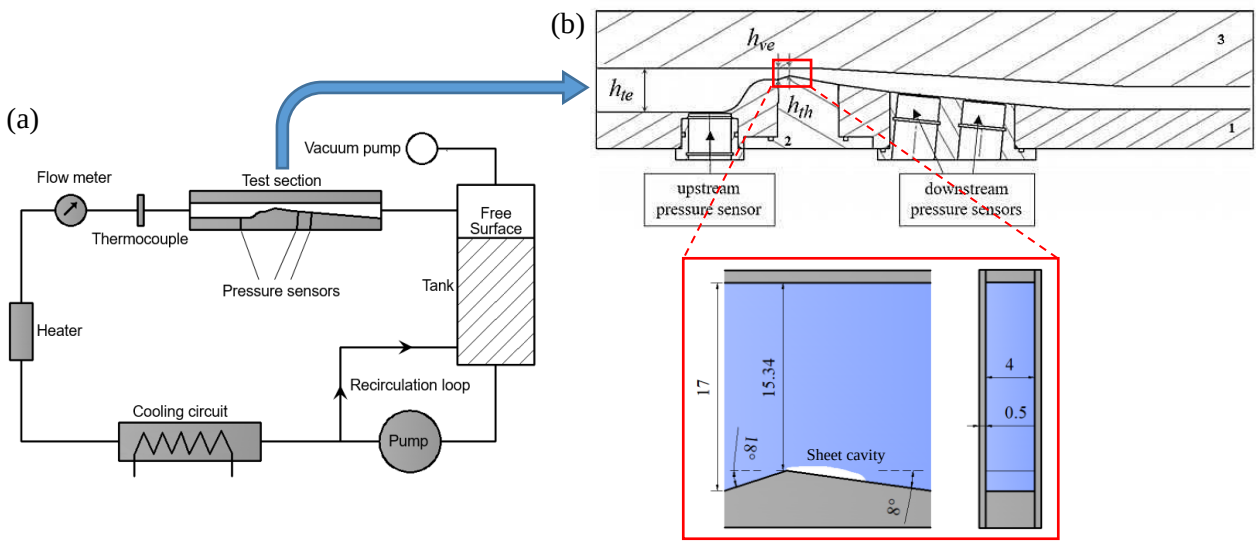
(a)
Vacuum pump
Flow meter
Test section
Thermocouple
Free Surface
Pressure sensors
Tank
Heater
Recirculation loop
Cooling circuit
Pump
(b)
$h_{ve}$
$h_{te}$
$h_{th}$
3
2
1
upstream pressure sensor
downstream pressure sensors
17
15.34
8°
Sheet cavity
8°
4
0.5

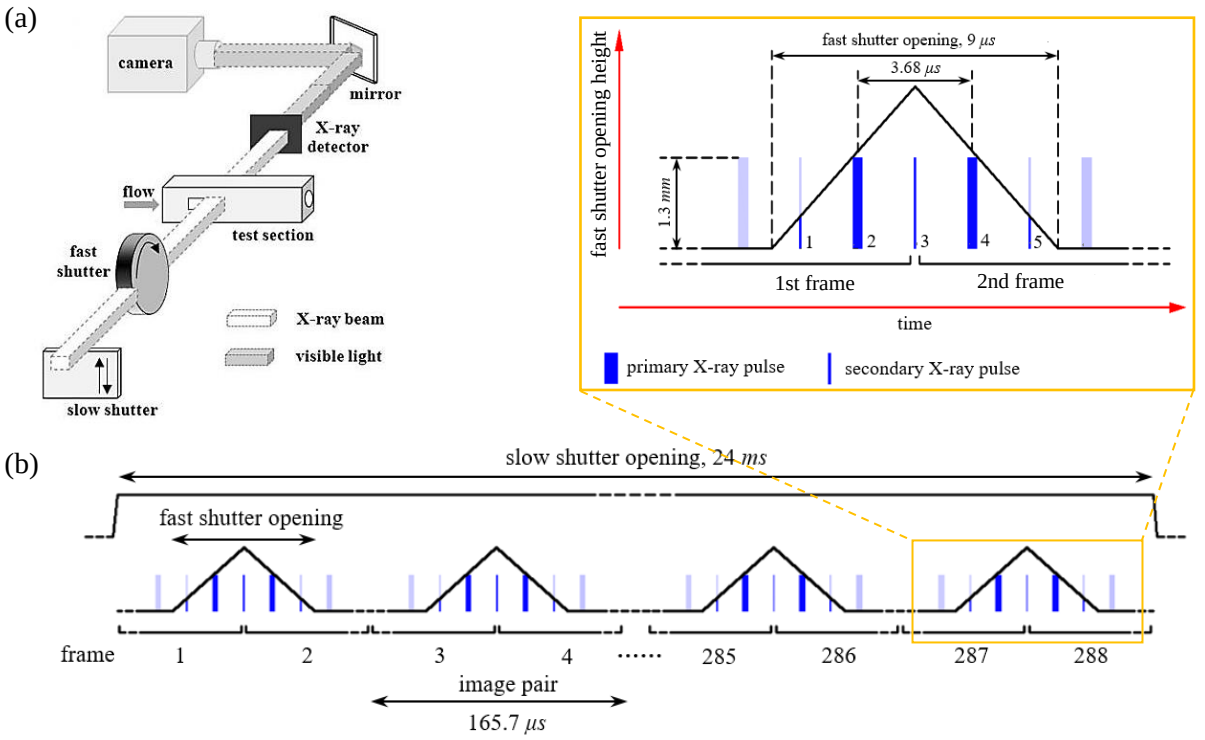
(a)
camera
mirror
X-ray detector
flow
test section
fast shutter
X-ray beam
visible light
slow shutter
fast shutter opening, 9 μs
3.68 μs
fast shutter opening height
1.3 mm
1
2
3
4
5
1st frame
2nd frame
time
primary X-ray pulse
secondary X-ray pulse
(b)
slow shutter opening, 24 ms
fast shutter opening
frame
1
2
3
4
285
286
287
288
image pair
165.7 μs

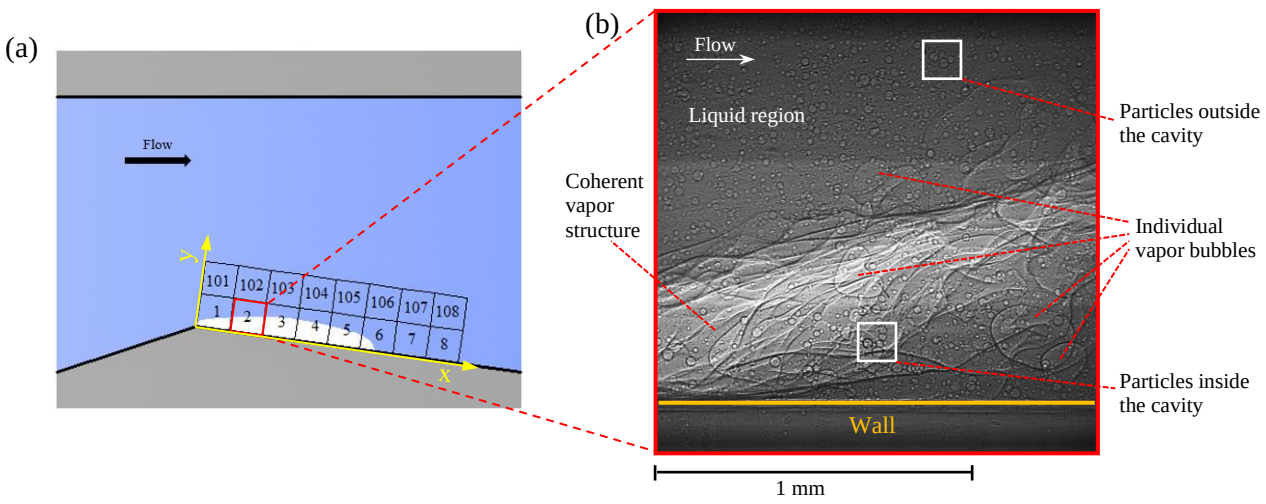
(a)
Flow
y
x
101
102
103
104
105
106
107
108
1
2
3
4
5
6
7
8
(b)
Flow
Liquid region
Coherent vapor structure
Particles outside the cavity
Individual vapor bubbles
Particles inside the cavity
Wall
1 mm

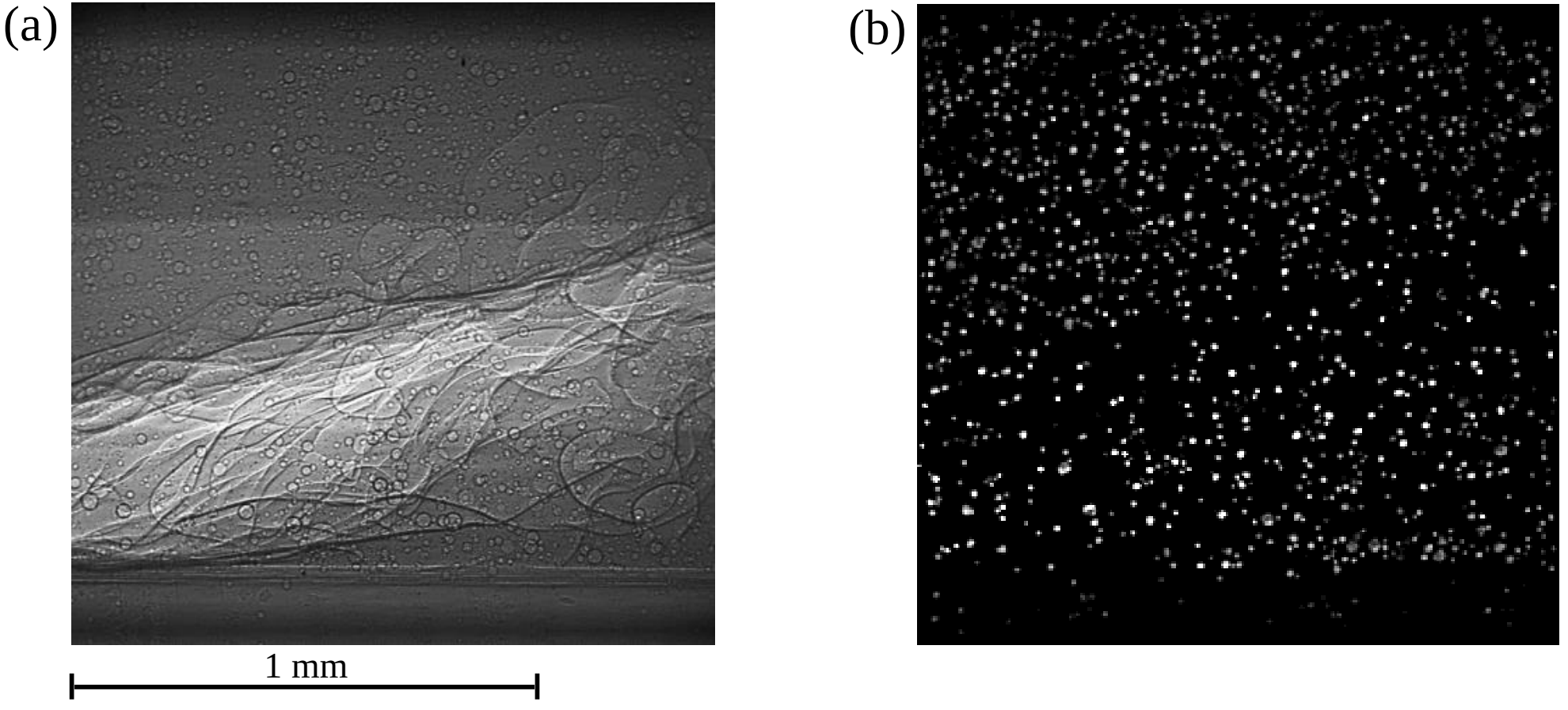
(a)
1 mm
(b)

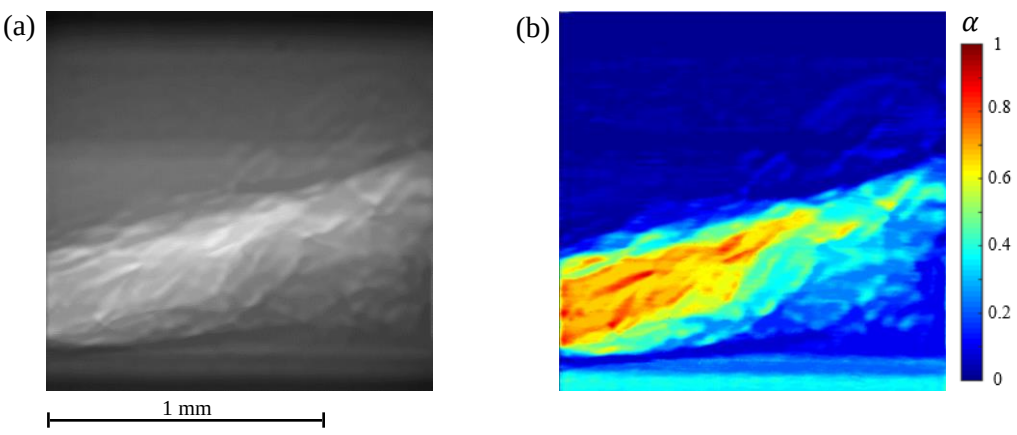
(a)
1 mm
(b)
α
1
0.8
0.6
0.4
0.2
0

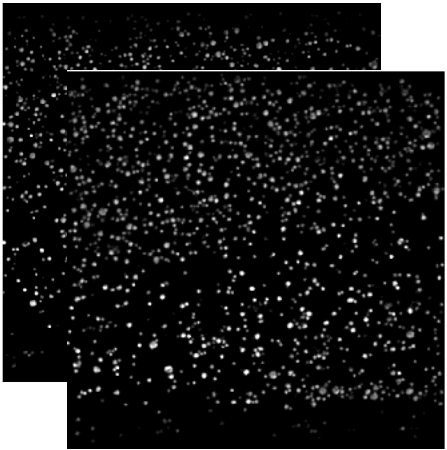

Cross-correlation

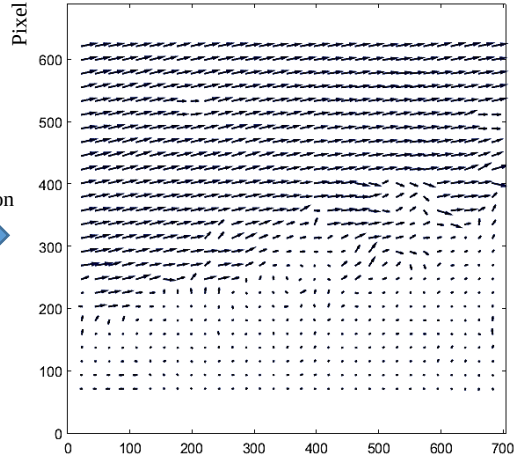

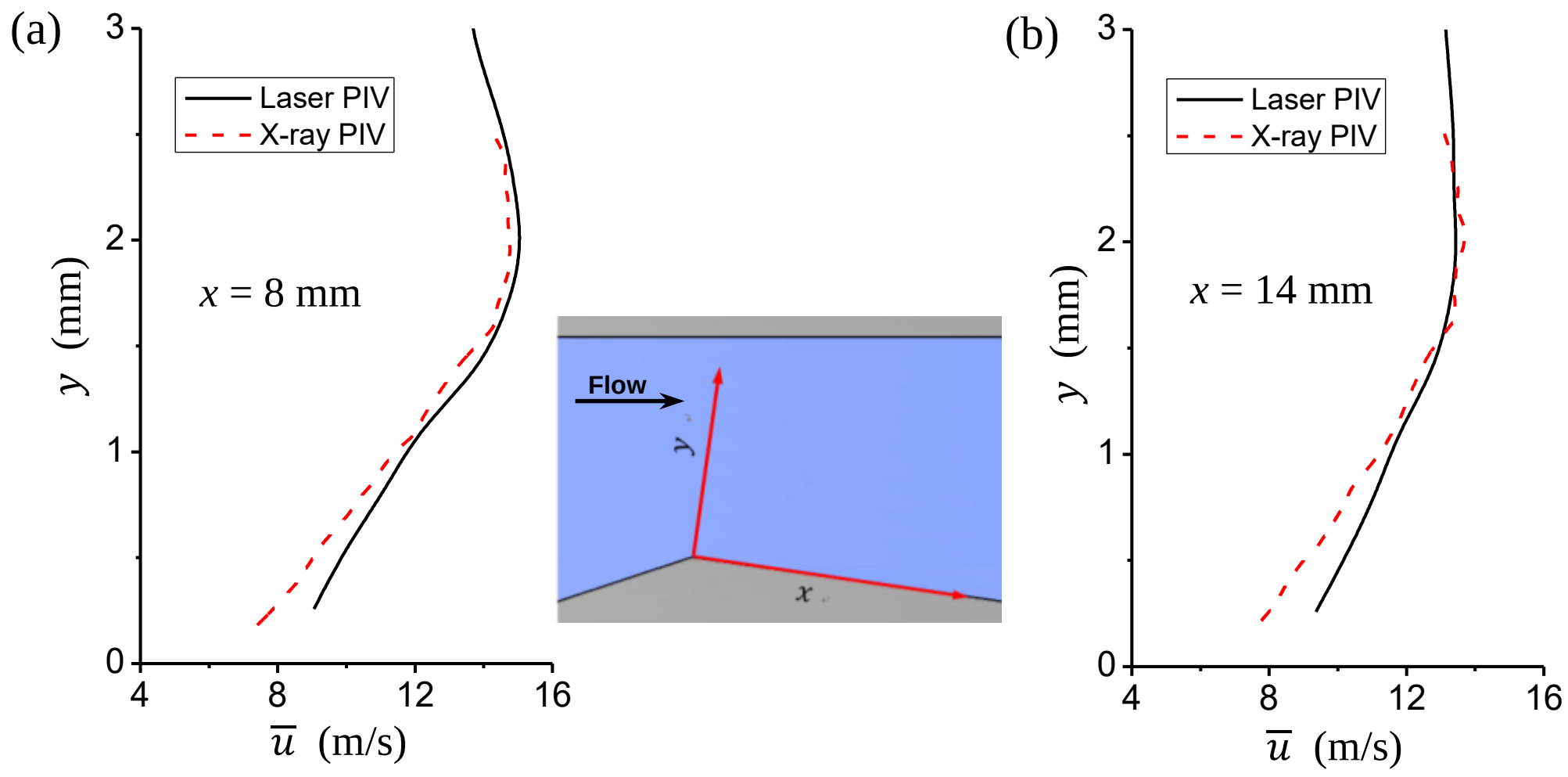
(a)
Laser PIV
X-ray PIV
x = 8 mm
y (mm)
$\overline{u}$ (m/s)
Flow
y
x
(b)
Laser PIV
X-ray PIV
x = 14 mm
y (mm)
$\overline{u}$ (m/s)

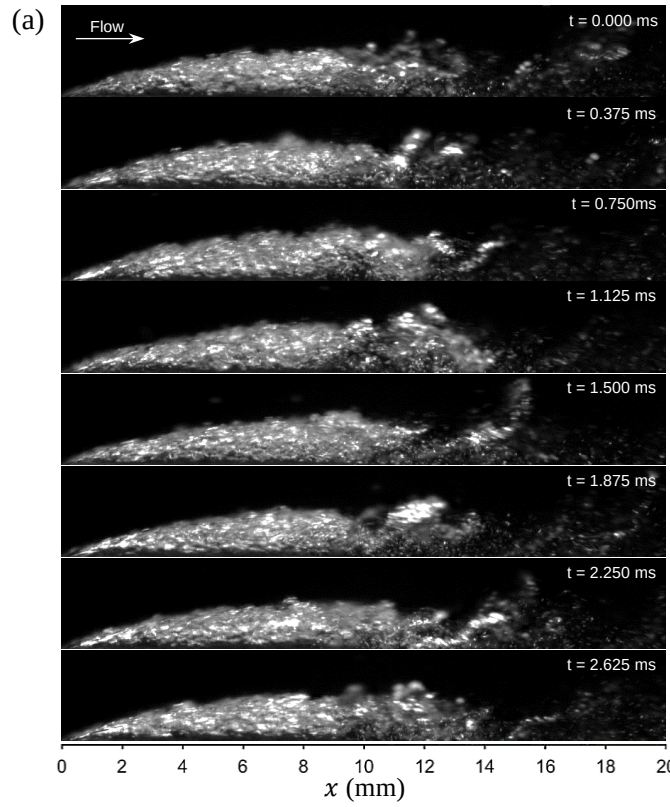
(a)
Flow
t = 0.000 ms
t = 0.375 ms
t = 0.750ms
t = 1.125 ms
t = 1.500 ms
t = 1.875 ms
t = 2.250 ms
t = 2.625 ms
0 2 4 6 8 10 12 14 16 18 20
x (mm)

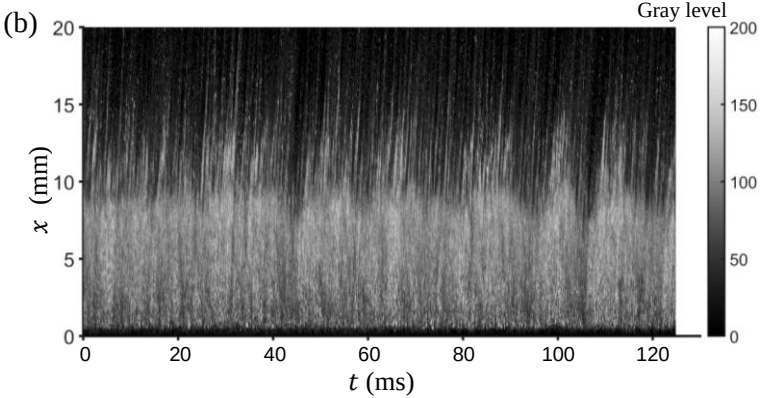
(b)
Gray level
200
150
100
50
0
20
15
10
5
0
x (mm)
0 20 40 60 80 100 120
t (ms)

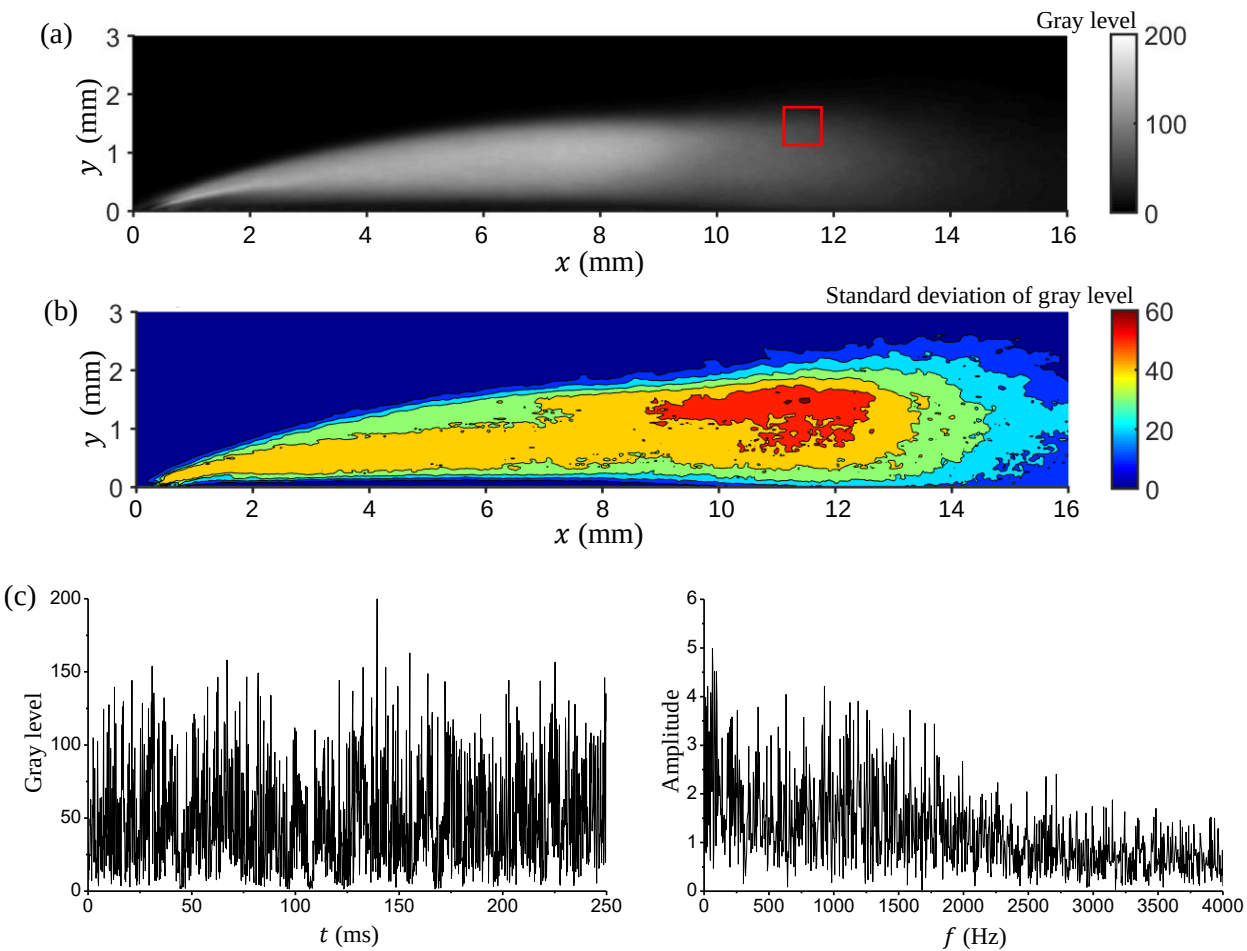
(a)
Gray level
200
100
0
y (mm)
x (mm)
(b)
Standard deviation of gray level
60
40
20
0
y (mm)
x (mm)
(c)
Gray level
t (ms)
Amplitude
f (Hz)

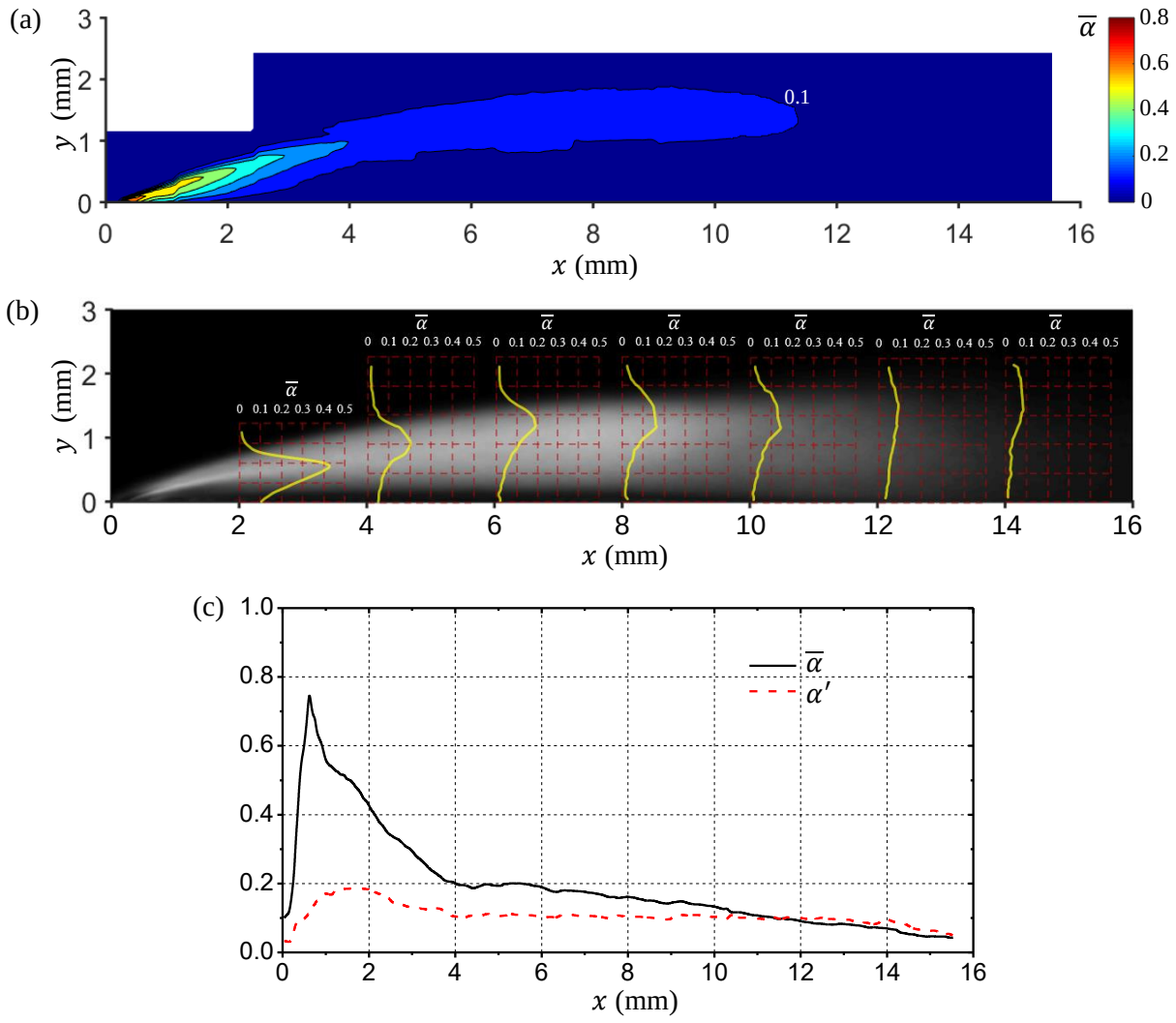
(a)
$\overline{\alpha}$
0.8
0.6
0.4
0.2
0
0.1
y (mm)
x (mm)
(b)
$\overline{\alpha}$
0 0.1 0.2 0.3 0.4 0.5
y (mm)
x (mm)
(c)
$\overline{\alpha}$
$\alpha'$
y (mm)
x (mm)

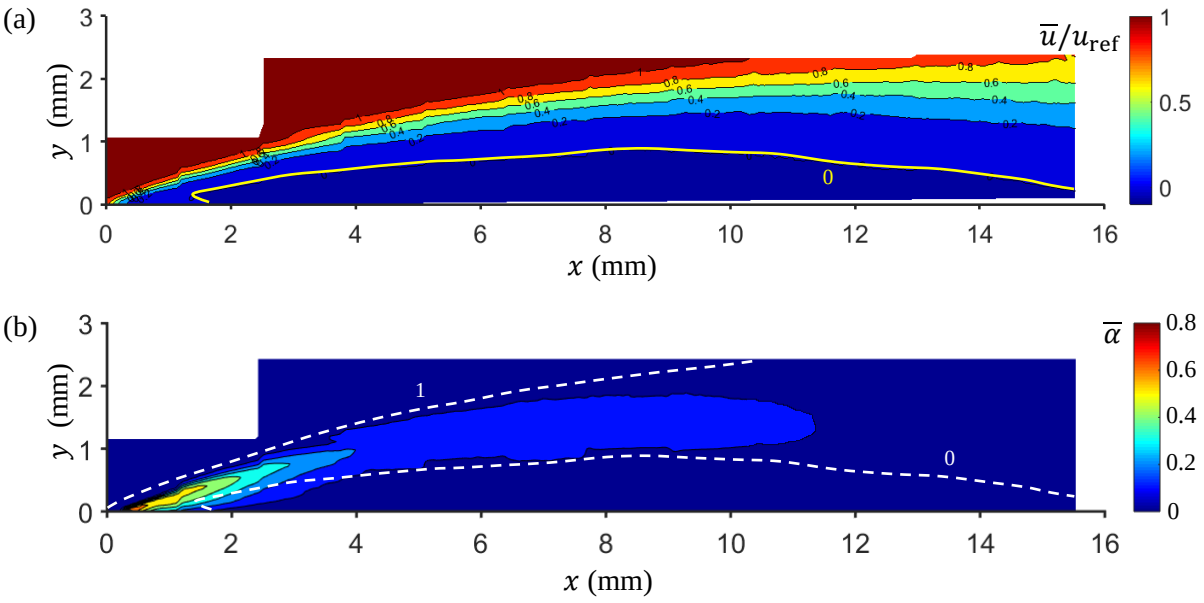
(a)
$\overline{u}/u_{\mathrm{ref}}$
1
0.5
0
$y$ (mm)
$x$ (mm)
0
2
4
6
8
10
12
14
16
3
2
1
0
0.8
0.6
0.4
0.2
(b)
$\overline{\alpha}$
0.8
0.6
0.4
0.2
0
1
0
$y$ (mm)
$x$ (mm)

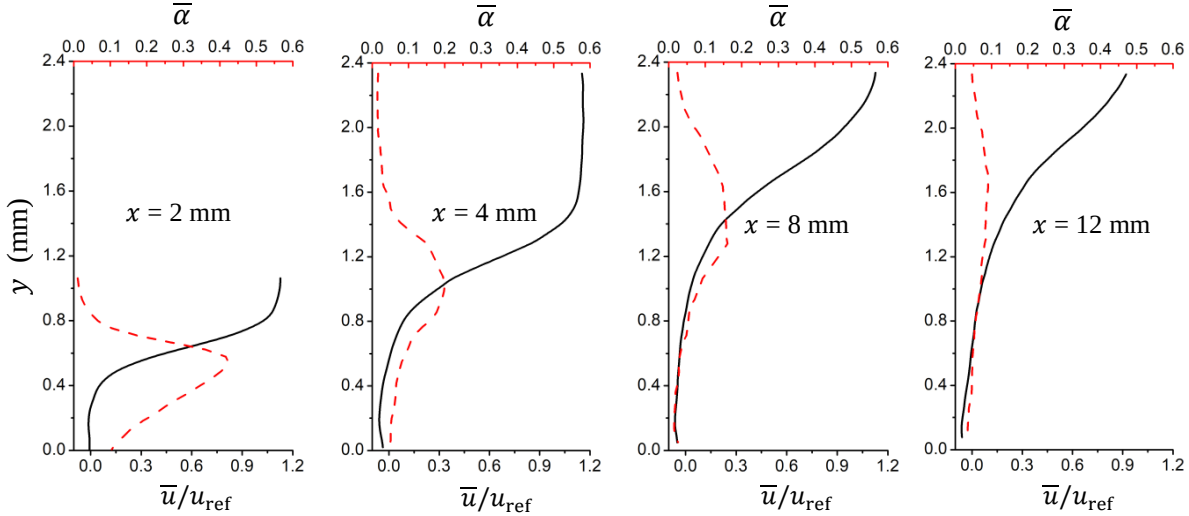
$\overline{\alpha}$
0.0 0.1 0.2 0.3 0.4 0.5 0.6
$y$ (mm)
2.4
2.0
1.6
1.2
0.8
0.4
0.0
$x$ = 2 mm
$x$ = 4 mm
$x$ = 8 mm
$x$ = 12 mm
0.0 0.3 0.6 0.9 1.2
$\overline{u}/u_{\mathrm{ref}}$

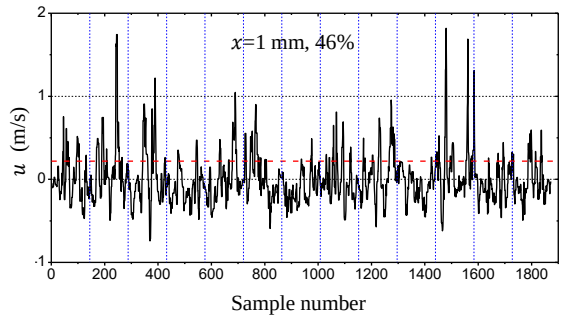
x=1 mm, 46%
u (m/s)
Sample number

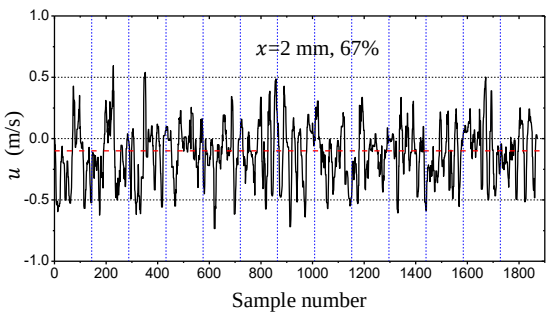
x=2 mm, 67%
u (m/s)
Sample number

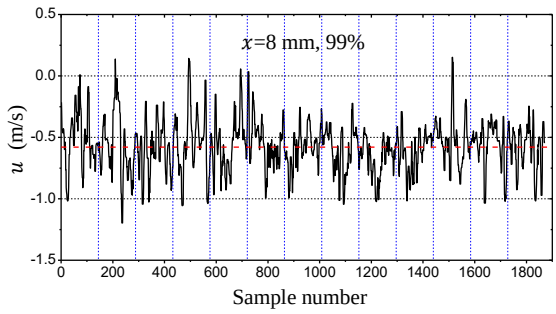
x=8 mm, 99%
u (m/s)
Sample number

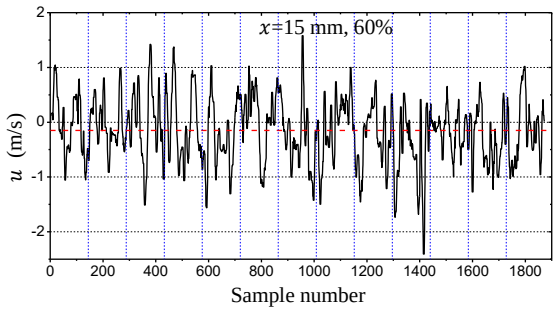
x=15 mm, 60%
u (m/s)
Sample number

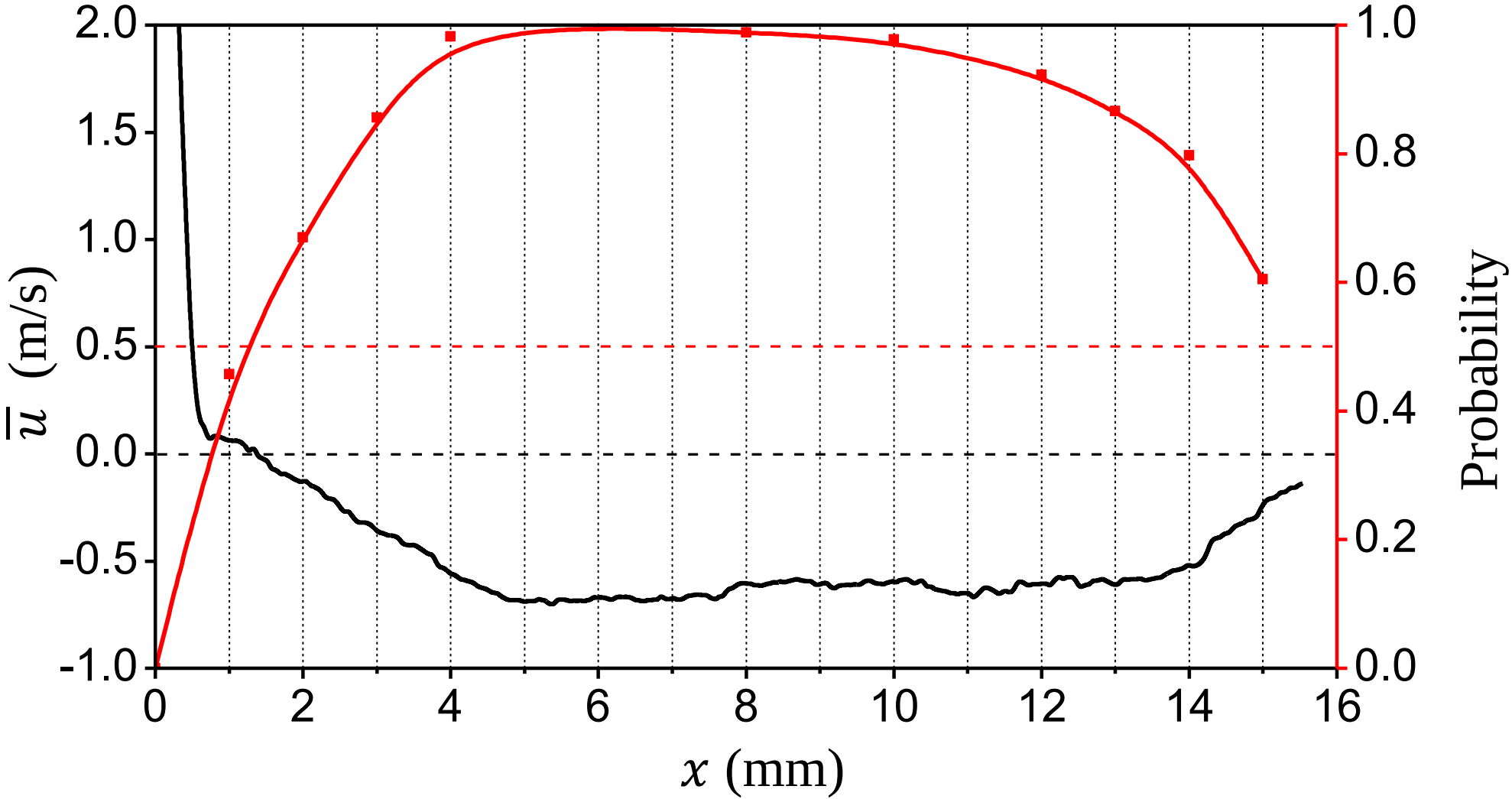
2.0
1.5
1.0
0.5
0.0
-0.5
-1.0
$\overline{u}$ (m/s)
1.0
0.8
0.6
0.4
0.2
0.0
Probability
0
2
4
6
8
10
12
14
16
$x$ (mm)

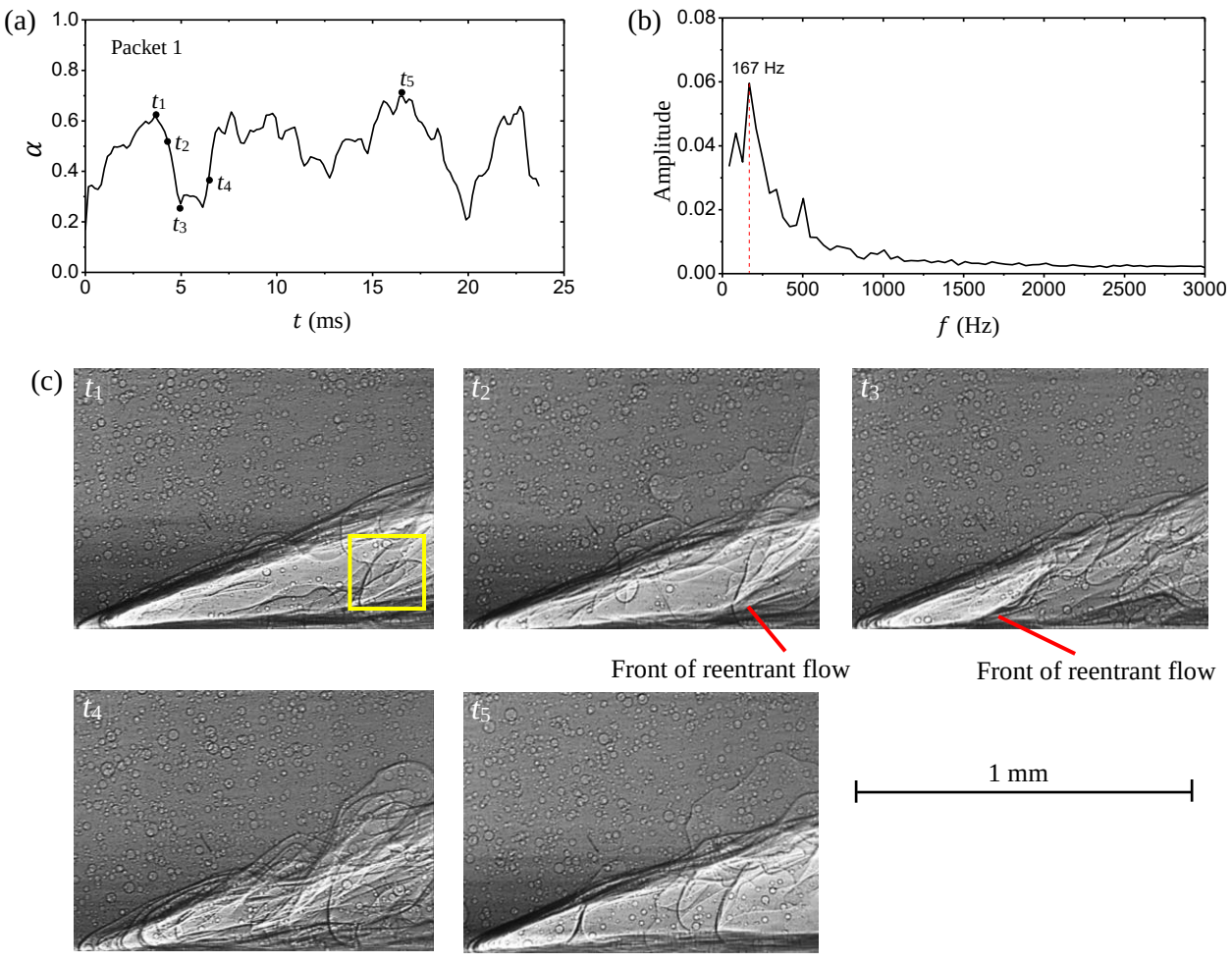
(a)
Packet 1
$t_1$
$t_2$
$t_3$
$t_4$
$t_5$
$\alpha$
$t$ (ms)
(b)
167 Hz
Amplitude
$f$ (Hz)
(c)
$t_1$
$t_2$
$t_3$
$t_4$
$t_5$
Front of reentrant flow
Front of reentrant flow
1 mm

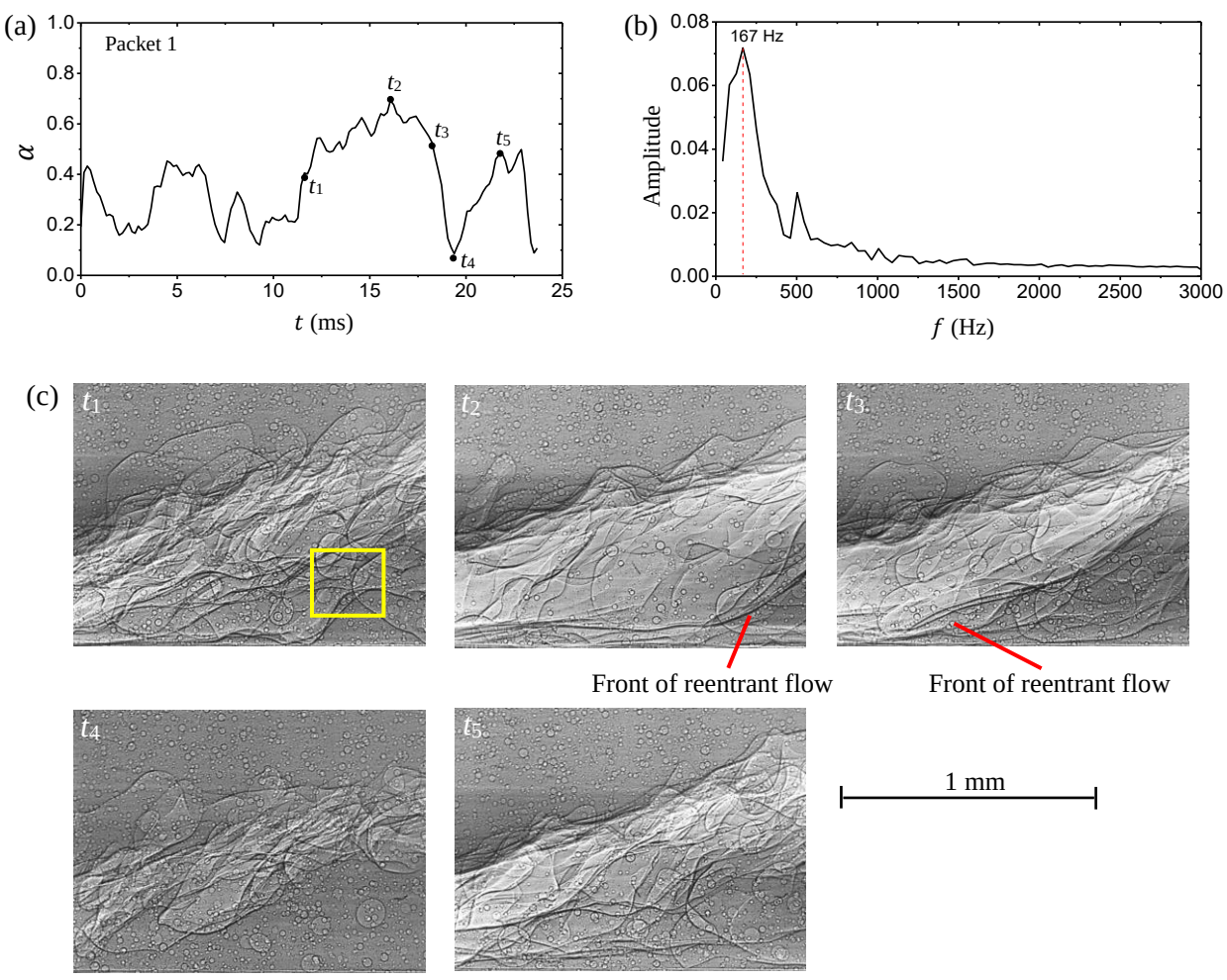
(a)
Packet 1
$t_1$
$t_2$
$t_3$
$t_4$
$t_5$
$\alpha$
$t$ (ms)
(b)
167 Hz
Amplitude
$f$ (Hz)
(c)
$t_1$
$t_2$
$t_3$
$t_4$
$t_5$
Front of reentrant flow
Front of reentrant flow
1 mm

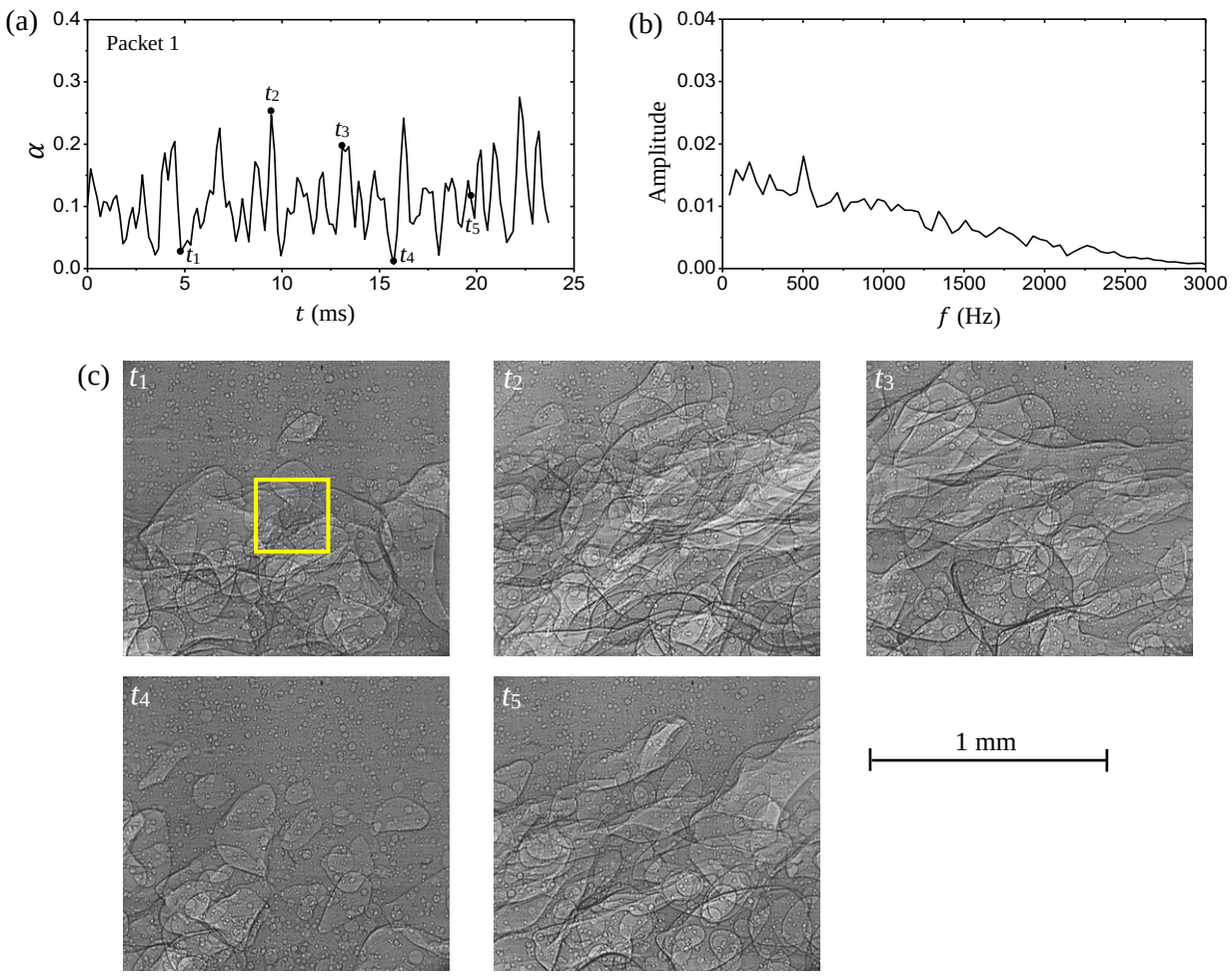
(a)
Packet 1
α
t (ms)
t1
t2
t3
t4
t5
(b)
Amplitude
f (Hz)
(c)
t1
t2
t3
t4
t5
1 mm

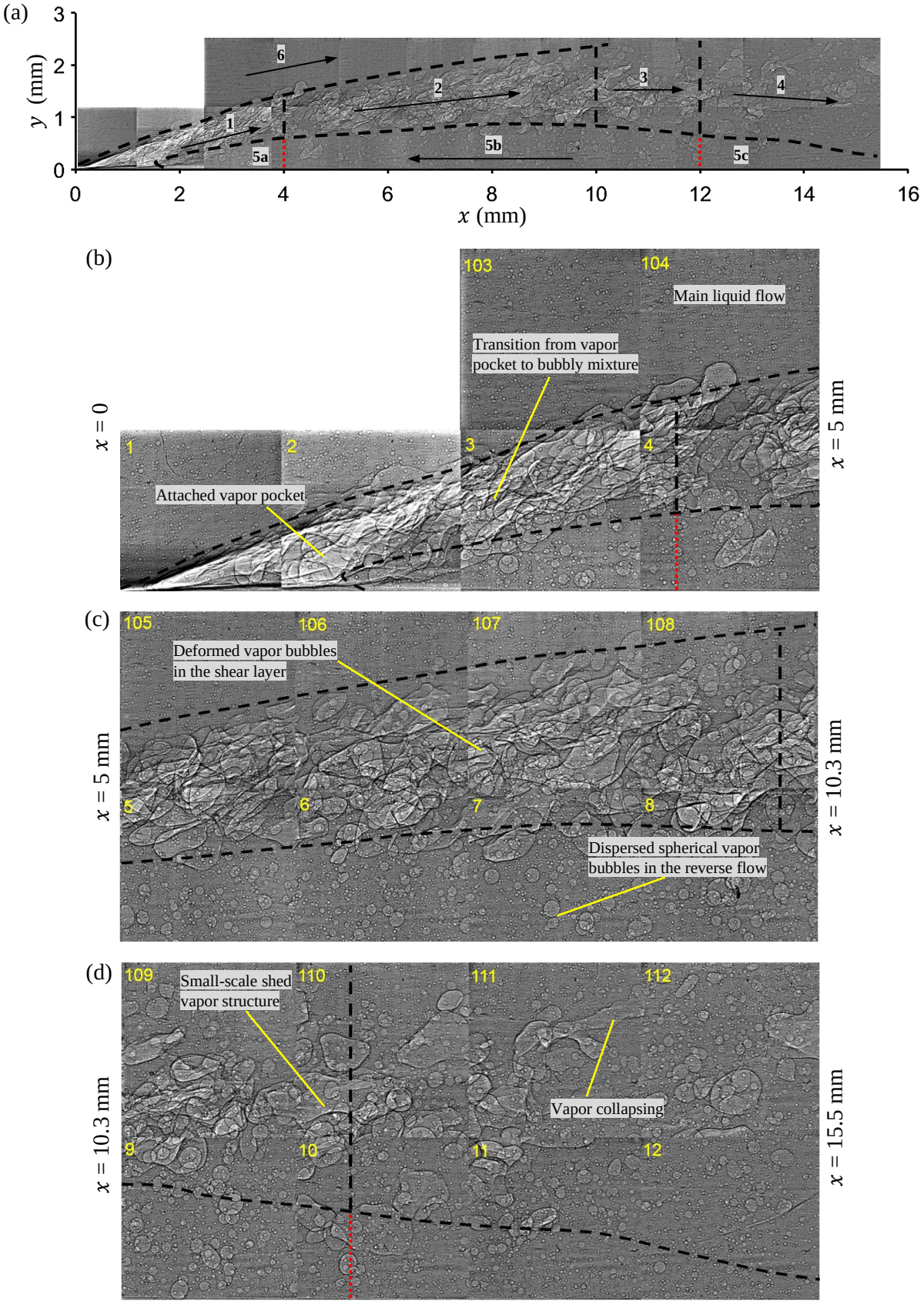
(a)
y (mm)
x (mm)
0
1
2
3
0
2
4
6
8
10
12
14
16
1
2
3
4
5a
5b
5c
6
(b)
x = 0
x = 5 mm
103
104
Main liquid flow
Transition from vapor
pocket to bubbly mixture
1
2
3
4
Attached vapor pocket
(c)
x = 5 mm
x = 10.3 mm
105
106
107
108
Deformed vapor bubbles
in the shear layer
5
6
7
8
Dispersed spherical vapor
bubbles in the reverse flow
(d)
x = 10.3 mm
x = 15.5 mm
109
110
111
112
Small-scale shed
vapor structure
Vapor collapsing
9
10
11
12

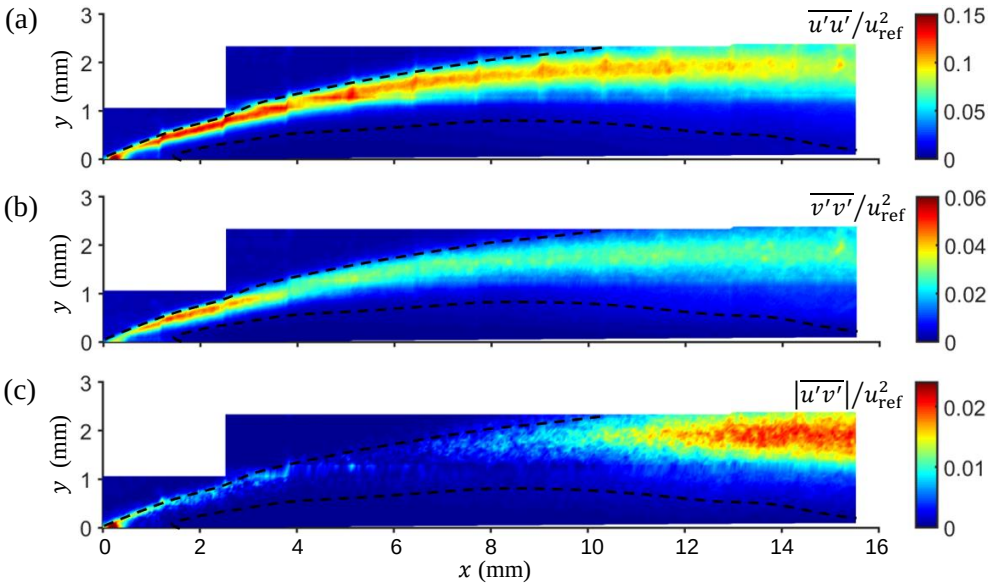
(a)
$\overline{u'u'}/u_{ref}^2$
0.15
0.1
0.05
0
(b)
$\overline{v'v'}/u_{ref}^2$
0.06
0.04
0.02
0
(c)
$|\overline{u'v'}|/u_{ref}^2$
0.02
0.01
0
y (mm)
x (mm)
0
2
4
6
8
10
12
14
16
1
3

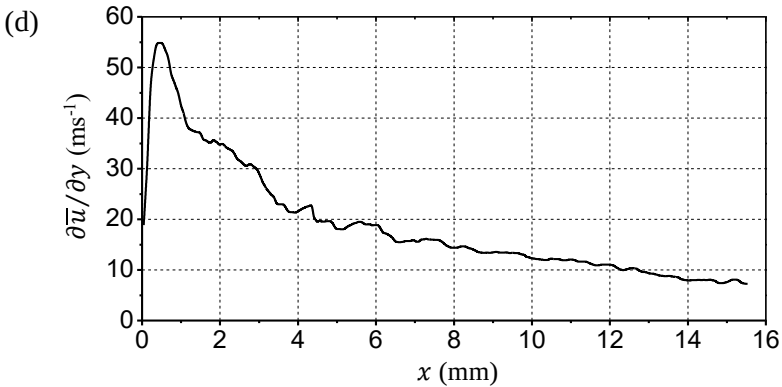
(d)
$\partial\overline{u}/\partial y$ (ms$^{-1}$)
x (mm)
0
10
20
30
40
50
60
2
4
6
8
12
14
16

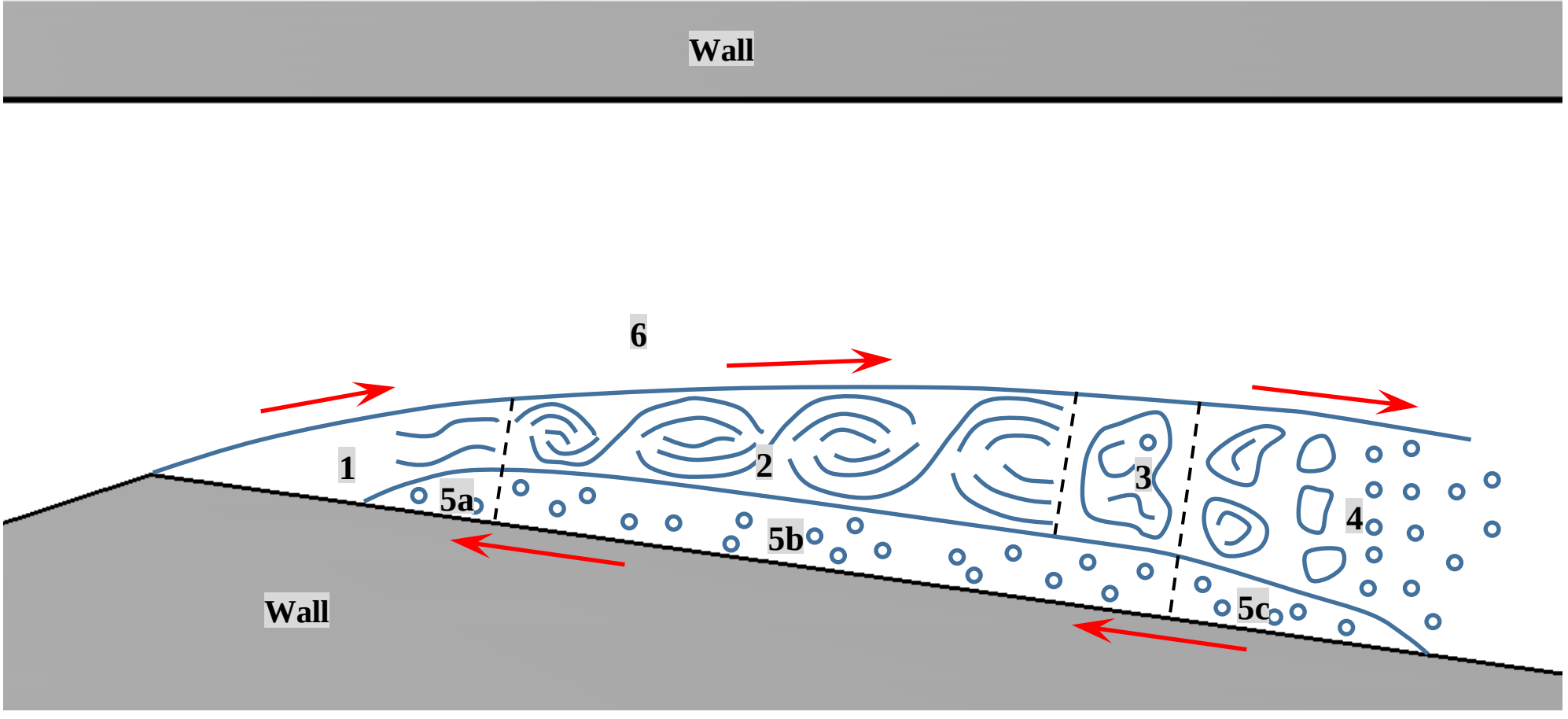
Wall
6
1
2
3
4
5a
5b
5c
Wall

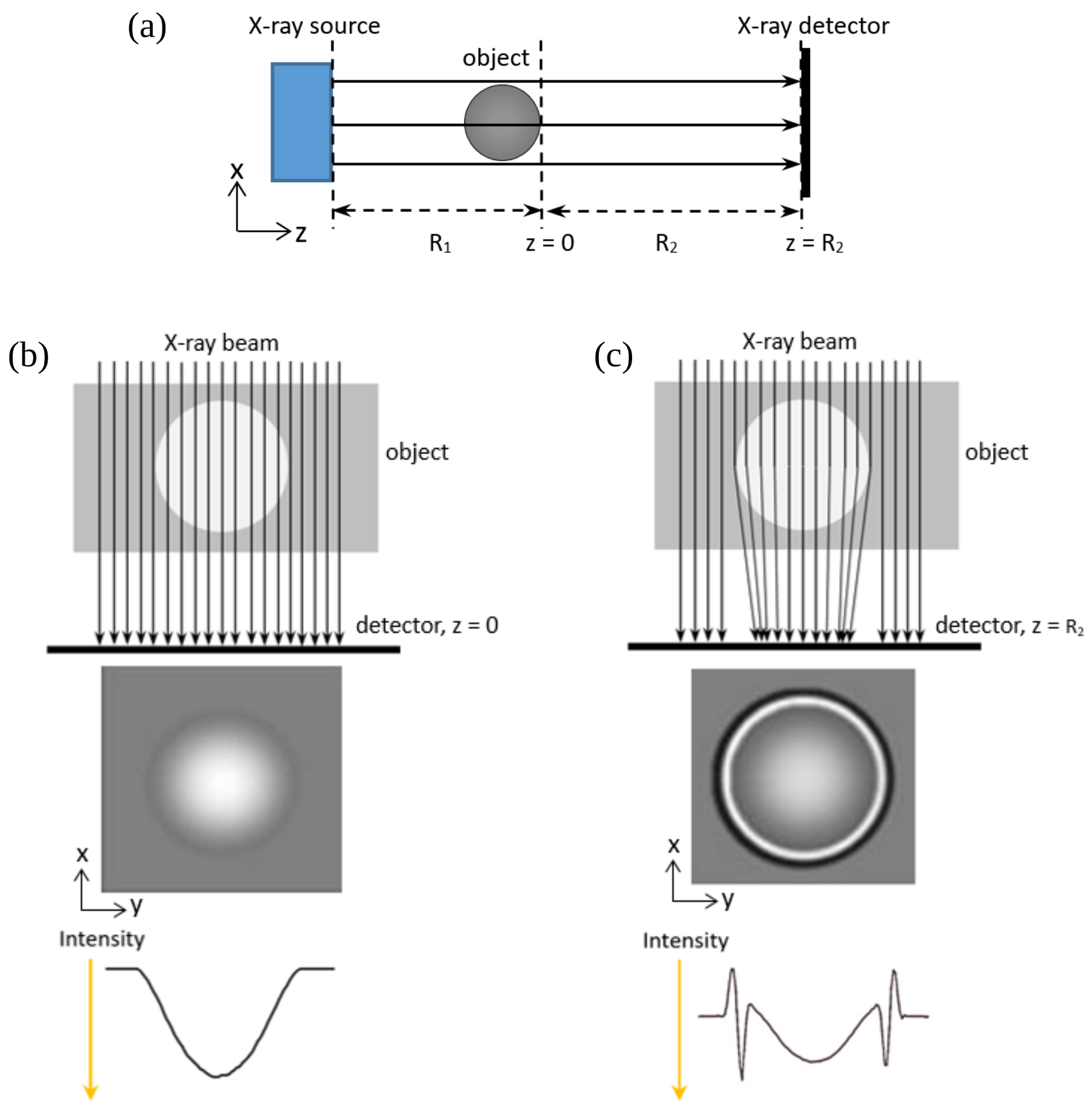
(a)
X-ray source
object
X-ray detector
x
z
R1
z = 0
R2
z = R2
(b)
X-ray beam
object
detector, z = 0
x
y
Intensity
(c)
X-ray beam
object
detector, z = R2
x
y
Intensity

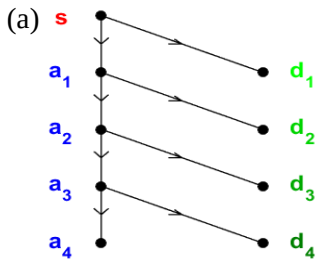
(a)
s
a1
a2
a3
a4
d1
d2
d3
d4

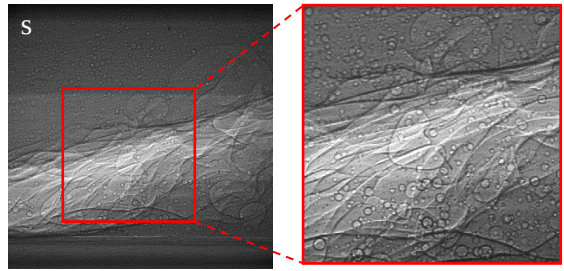
(b)
s

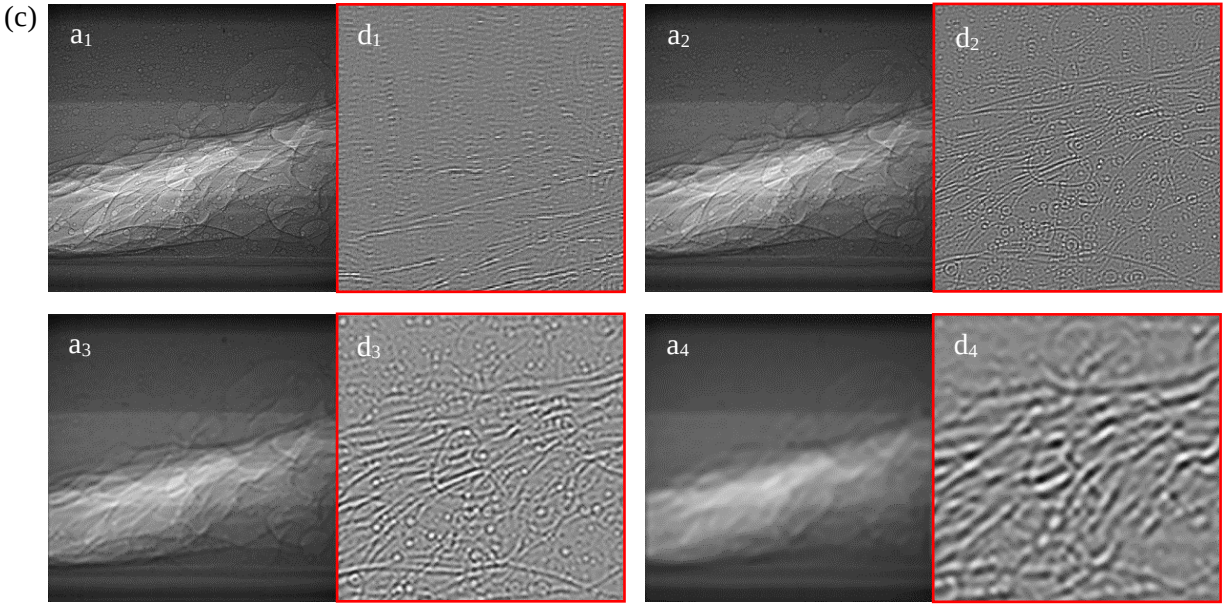
(c)
a1
d1
a2
d2
a3
d3
a4
d4

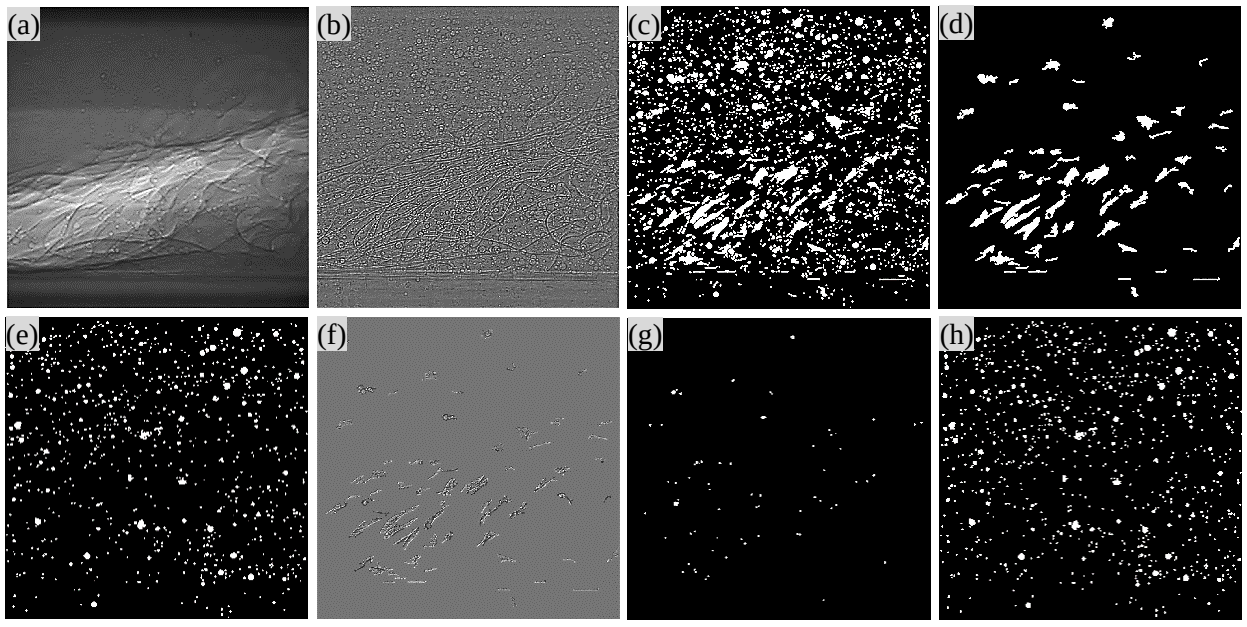
(a)
(b)
(c)
(d)
(e)
(f)
(g)
(h)

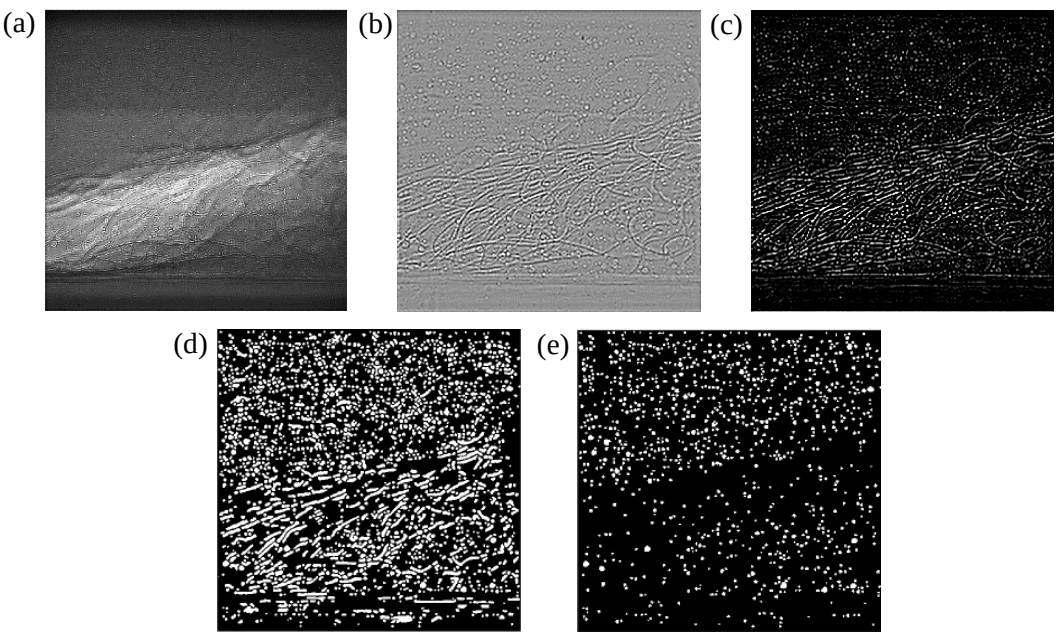
(a)
(b)
(c)
(d)
(e)

(a)

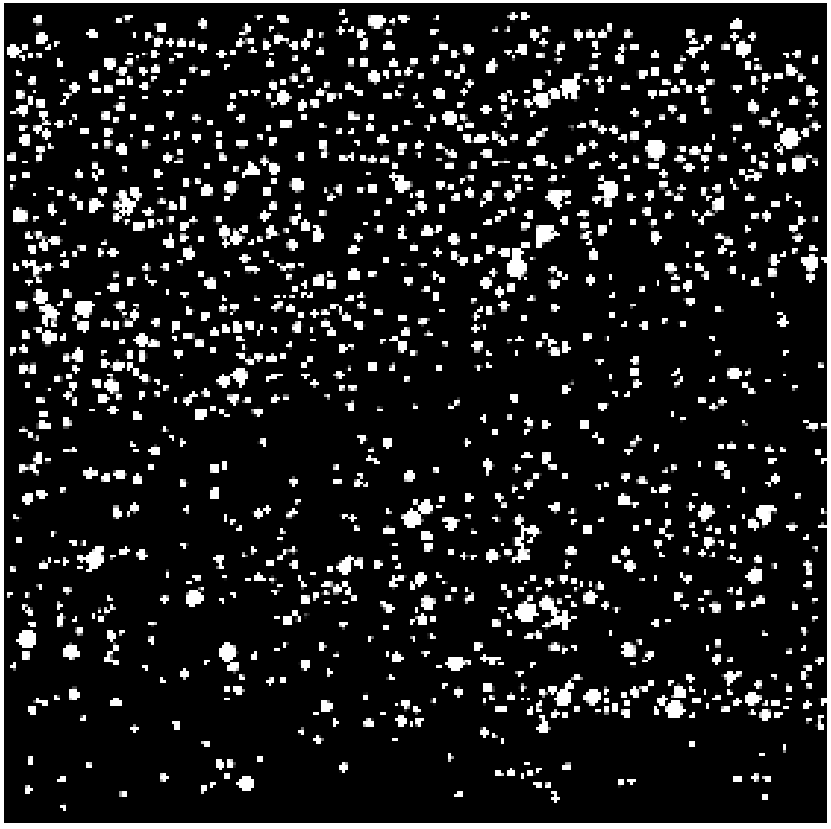

(b)

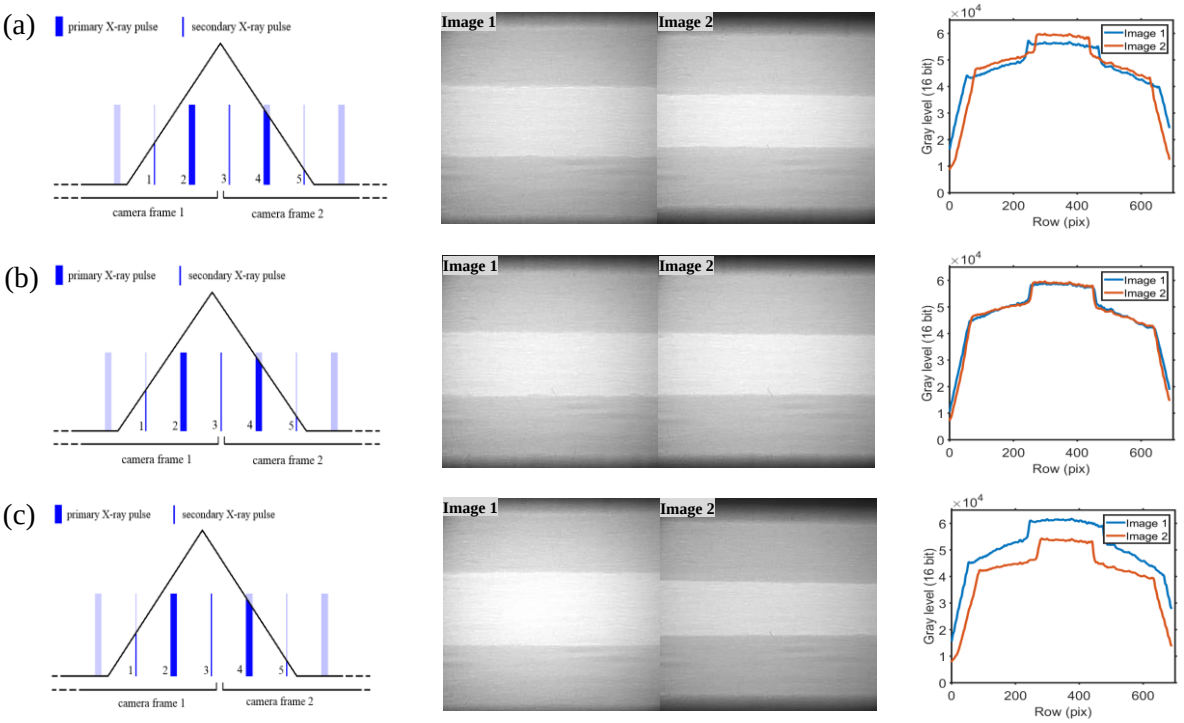
(a)
primary X-ray pulse
secondary X-ray pulse
1
2
3
4
5
camera frame 1
camera frame 2
Image 1
Image 2
×10^4
Gray level (16 bit)
Row (pix)
(b)
primary X-ray pulse
secondary X-ray pulse
1
2
3
4
5
camera frame 1
camera frame 2
Image 1
Image 2
×10^4
Gray level (16 bit)
Row (pix)
(c)
primary X-ray pulse
secondary X-ray pulse
1
2
3
4
5
camera frame 1
camera frame 2
Image 1
Image 2
×10^4
Gray level (16 bit)
Row (pix)

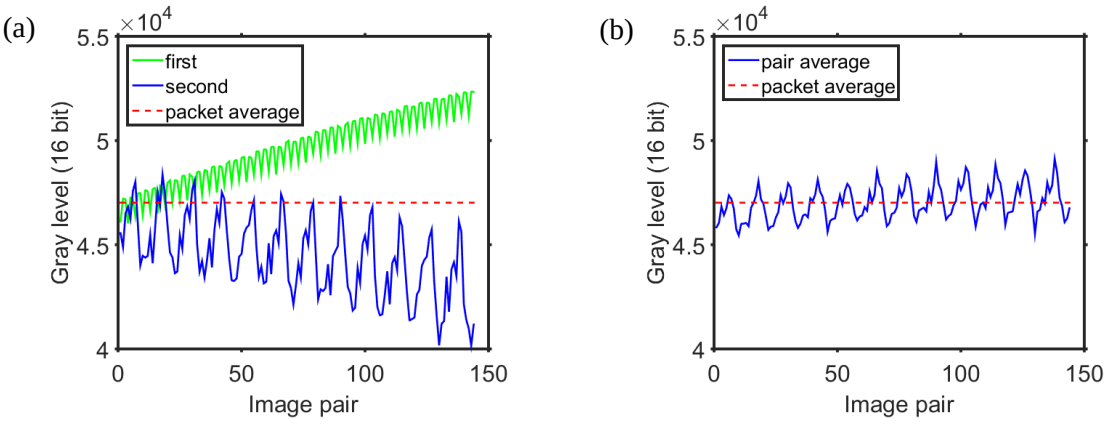
(a)
×10^4
5.5
5
4.5
4
first
second
packet average
Gray level (16 bit)
0
50
100
150
Image pair
(b)
×10^4
5.5
5
4.5
4
pair average
packet average
Gray level (16 bit)
0
50
100
150
Image pair

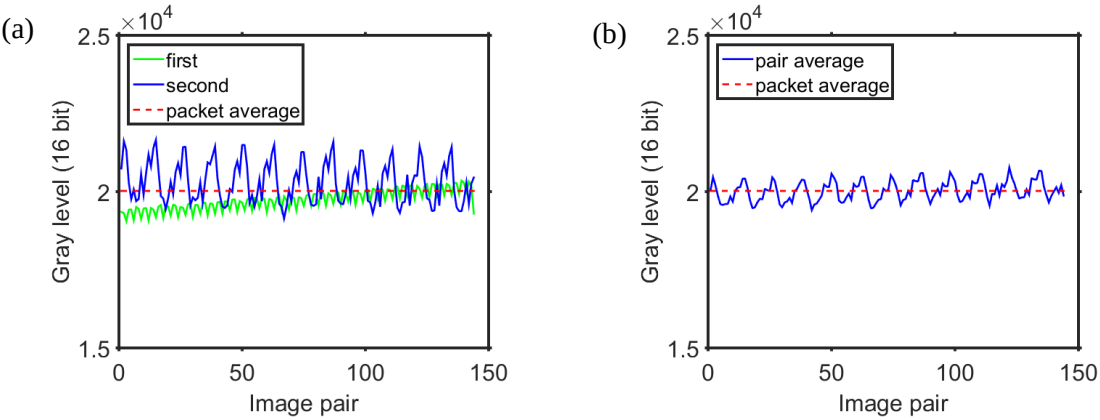
(a)
×10^4
2.5
2
1.5
first
second
packet average
Gray level (16 bit)
0
50
100
150
Image pair
(b)
×10^4
2.5
2
1.5
pair average
packet average
Gray level (16 bit)
0
50
100
150
Image pair

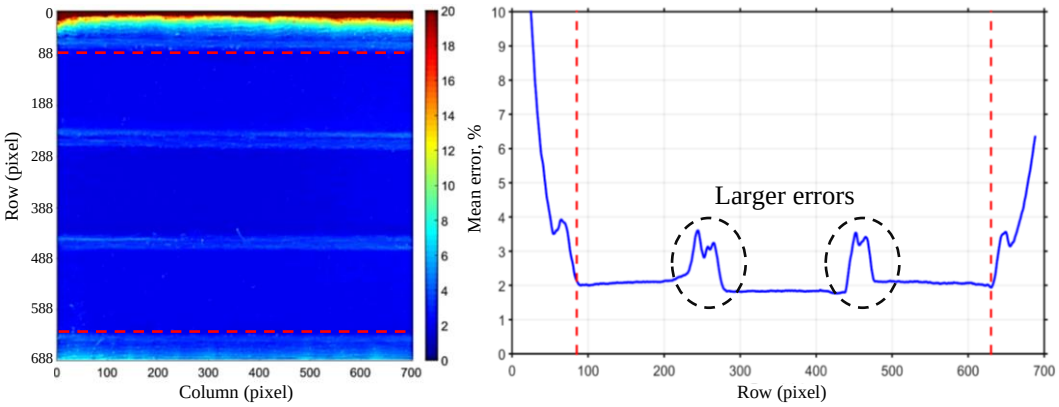
Row (pixel)
Column (pixel)
Mean error, %
Row (pixel)
Larger errors

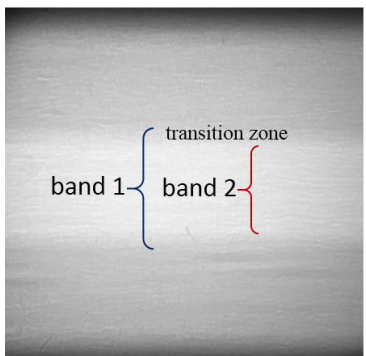
transition zone
band 1
band 2

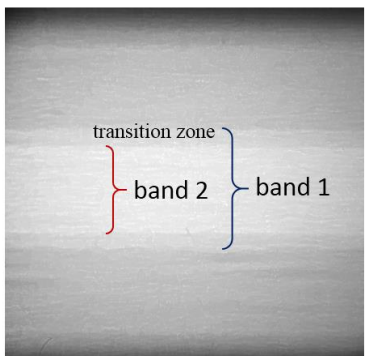
transition zone
band 2
band 1

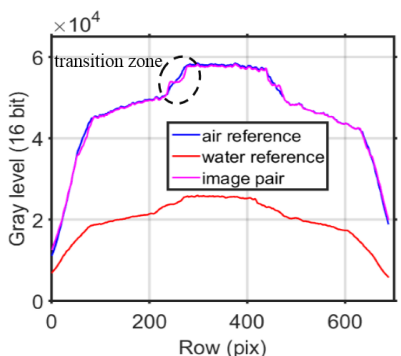
×10^4
6
4
2
0
transition zone
air reference
water reference
image pair
Gray level (16 bit)
0
200
400
600
Row (pix)

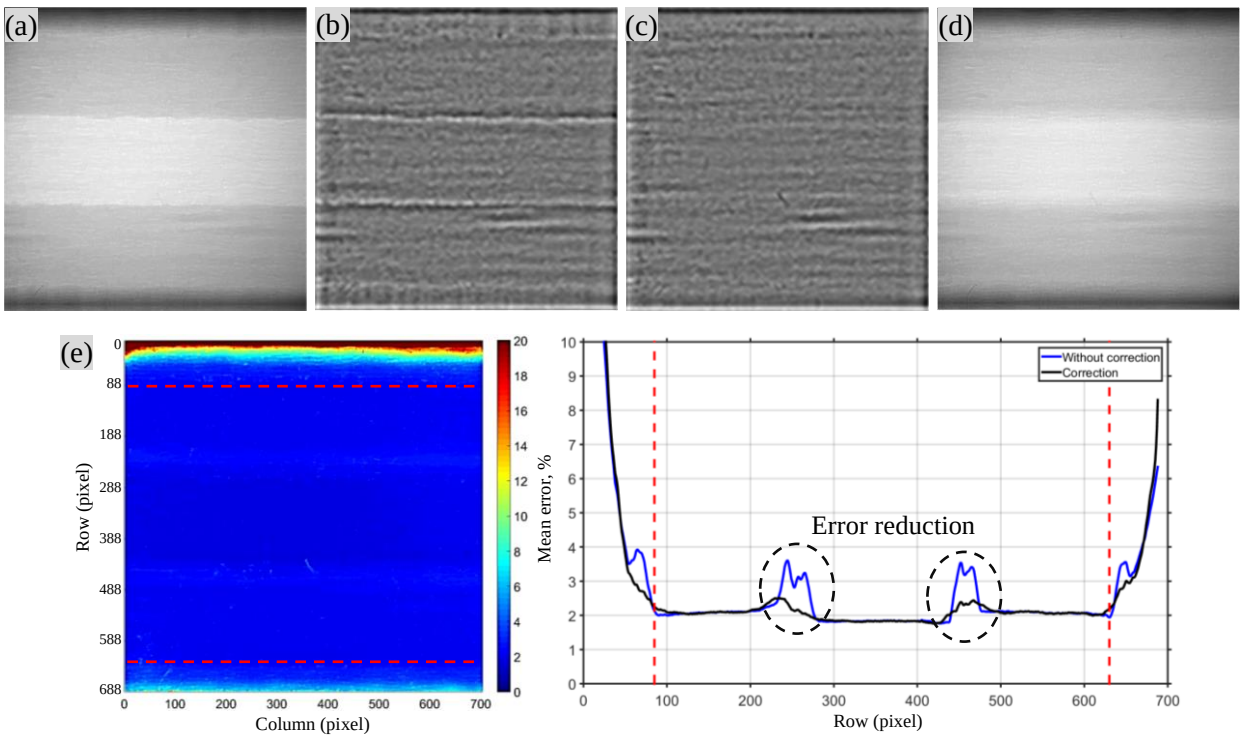
(a)
(b)
(c)
(d)
(e)
Row (pixel)
Column (pixel)
Mean error, %
Row (pixel)
Without correction
Correction
Error reduction

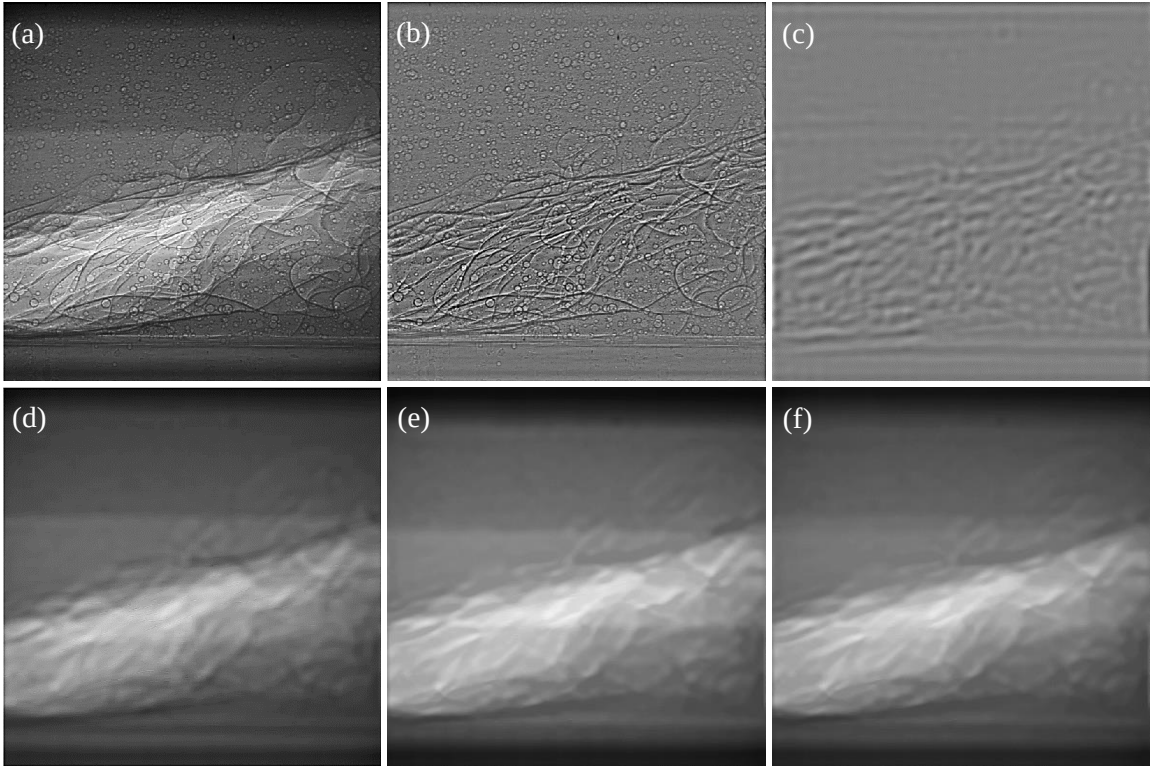
(a)
(b)
(c)
(d)
(e)
(f)